Evaluations of Powder Bed Fusion for Microwave Applications

Robert Batson

Centre for High Frequency Engineering

School of Engineering

Cardiff University

A thesis submitted to Cardiff University

for the degree of Doctor of Philosophy

November 2023

Abstract

Additive Manufacturing (AM) of metals is of interest to passive microwave applications as it introduces new design techniques for microwave components. However, with AM metals there are numerous issues and unknown variables. This thesis aims to address some of these variables, with the use of a novel broadband microwave technique for the characterisation of AM parts.

This thesis presents three proposed methods used to investigate the performance via surface resistance, to gain a better understanding of the performance of Powder Bed Fusion (PBF). The chosen method is based on a broadband resonator (in the range of 2.8 - 8.9GHz) and is a novel measurement technique specifically used to characterise surface resistance over a range of frequencies, and uses additional isotropic magnetic field to investigate the microwave properties of PBF when applied at different angles. Experimental studies are performed to investigate the effects of build orientation of samples produced via PBF to evaluate their surface resistance for use for microwave applications.

Finally, post-processing techniques have been studied to evaluate their effectiveness for microwave applications over a broad range of frequencies, with comparisons made to both their as-built counterparts as well as bulk material fabricated parts using subtractive methods of manufacturing.

Acknowledgements

I would first like to express my sincere gratitude to my supervisor *Prof. Adrian Porch* who as offered guidance and supported me throughout the duration of my PhD and offering myself the chance pursue down this avenue of research. I couldn't have asked for a better person to become my mentor.

I acknowledge the financial support of Renishaw Plc. and I would like to thank especially *Dr .Nick Jones* for proving me samples for my thesis research and *Dr.Kenneth Nai* for giving insight into the additive manufacturing process.

I am grateful to my fellow colleagues at the Centre of High Frequency Engineering without whom this work would not have been possible without. Special thanks goes to *Dr. Mike Barter, Dr. Sam Hefford, Dr. Heungjae Choi, Dr. Jerome Cuenca and Dr James Bell* whose daily antics, asking how I'm still wearing shorts and stimulating conversations, brought warmth to the office and a smile to my face. I would also like to specifically thank the ENGIN mechanical workshop and personally *Mr .Andrew Rankmore* who spent much time with me discussing designs and different fabrication techniques.

Finally I would like to thank my family especially my parents, *Timothy and Tracey,* who have always pushed me in the right direction and have sacrifice a lot to get me into the position I am in now. I am eternally grateful and will never forget the times that I have had with them. Also to my brothers, *Callum and Owen* who may not know it but have helped me through a lot.

Publications and Conferences

R. Gumbleton, R. Batson, K. Nai and A. Porch, "Effect of Build Orientation and Laser Power on Microwave Loss in Metal Additive Manufactured Components," in IEEE Access, vol. 9, pp. 44514-44520, 2021, doi: 10.1109/ACCESS.2021.3067306.

R. Batson, R. Gumbleton, S. He ord, K. Nai and A. Porch, 'Microwave Surface Resistance of As-grown and Post-processed Additive Manufactured Metal Parts', Ampere Conference 2021, Gothenburg, Sweden, 13-16 September 2021

Contents

List of Figures

List of Tables

Abbreviations

R_S surface resistance.

AM Additive Manufacturing.

BBPPR Broad Brand Parallel Plate Resonator.

CAD Computer Aided Design.

CNC Computer Numerical Control.

CR Coaxial Resonator.

DR dielectric resonator.

EM Electromagnetic.

FPOR Fabry-Perot open Resonator.

HSD Hemispherical Dishes.

PBF Powder Bed Fusion.

SLM Selective Laser Melting.

SLS Selective Laser Sintering.

TEM Transverse Electro-Magnetic.

VNA Vector Network Analyser.

Chapter 1

Introduction and Thesis Summary

The overall theme of the thesis is to explore the potential of using additive manufacturing (AM) as a means of producing microwave parts for applications, such as waveguides, resonators and antennas, by utilising the Renishaw AM250 and AM500 AM machines, which use Powder Bed Fusion (PBF) to produce solid parts. The metal alloy powders are of various materials such as Titanium, Steel, Cobalt-Chromium and Aluminium. The basic principle of these machines is to use manufacturing data, which has been generated using CAD software and a model processing specific software, to accurately create complex geometric shapes via layer-by-layer material deposition and consolidation [1], with the powder melted using a focused, high power laser.

Each new layer of powder is melted and then fused with the previous layer to ensure that a fully dense metal object is produced. The surrounding powder aids with supporting this structure while under the PBF process, though in some cases support material is needed to ensure a successful build [2].

The two key factors which need to explored which are:

1. How does PBF perform over different bands within the microwave frequency spectrum?

2. Are there any post-processing treatments that can improve the performance of PBF?

These points will be expanded to establish the aims and objectives for this thesis.

1.1 Performance of PBF Over Multiple Microwave Bands

1.1.1 Motivation

The adoption of additive manufacturing as a means of production accounts for approximately 0.05% of global manufacturing but is growing rapidly[3, 4]. Consider the versatility of PBF and potential uses for different microwave applications such as NASA's Interstellar Mapping and Acceleration Probe, which uses an X-band choke-ring horn antenna [5]. The performance and characteristics of PBF changes depending on the operating frequency of the device. As mentioned previously, PBF uses layers of metal powder and melts these together, which inherently creates a rough surface which influences the surface resistance (R_S) of the PBF part. Given that there are many variables in the PBF process, it is likely that there will be an equally large range of surface qualities that can influence the value of R_s. A common approach has been to make a waveguide using PBF and measure the microwave attenuation constant[6, 7]. However, this approach is more suited to improve a singular design than characterising the material, since it characterises both the material and the geometry used for the waveguide.

1.1.2 Research Goals

The subjects of interest are the characteristics of the R_s of the PBF surfaces and how the value of R_s is affected when used at different microwave bands. The research documented within this thesis has involved the development of a microwave fixture for testing PBF samples over a range of frequencies to enable the measurement of R_s. To achieve this, a novel measurement technique based upon a coaxial resonator

have been used. This method was verified with simulation data and through the measurement of bulk materials and measurement of PBF plate samples, as a plate will not have any geometrical contributions to microwave losses. This is the first time that AM parts have been characterised over the C to X microwave bands, simultaneously, on the same part.This is coupled with measuring the effect of post-processing on these parts.

1.2 The Effects of Post-Processing Treatment to PBF

1.2.1 Motivation

The use of layered metal powers for PBF with a high-energy laser produces a dense metal part but inherently creates a rough surface which influences the R_s. With post-processing we expect to be able to reduce this value and also to measure the values of R_s by either reducing the surface roughness or introducing a new material to be exposed to the induced current across the surface of the metal sample in different build orientations. Understanding the effects on R_s due to rough surfaces and the affect of build orientation on R_s is critical to the successful development of 3D microwave components which use the PBF process such as waveguides, spline horn antennas and feed clusters.

1.2.2 Research Goals

In order to investigate the changes of R_s with respect to post-processing, a microwave device that can apply a focused magnetic field to the sample under test is needed, so that an accurate measurement of R_s values can be taken. This is realised by

using a novel broadband coaxial-type resonator discussed later in this thesis, which incorporates the sample under test into the resonant structure.

Chapter 2

Literature Review and Background

2.1 Additive Manufacturing

2.1.1 Additive Manufacturing Overview

Additive manufacturing, also known as ”3D Printing”, is a type of fabrication which utilises multiple layers which are 2-dimensional and builds up these layers to create a 3-dimensional model[8, 9].These are the building blocks that allow for rapid prototyping and reduction of costs[10][11]. The reason for this is that when using AM very little waste is produced, which is mostly support material, used to ensure that the print is successful by supporting features that are most commonly overhanging [12, 13]; the vast majority of material is used to make the item itself.

There are many forms of AM which utilise different materials which range from plastics[14, 15], liquid resins[16, 17] and metal powders[18, 19]. All of these use a different method of solidifying their layers to create a 3D object. Some use UV

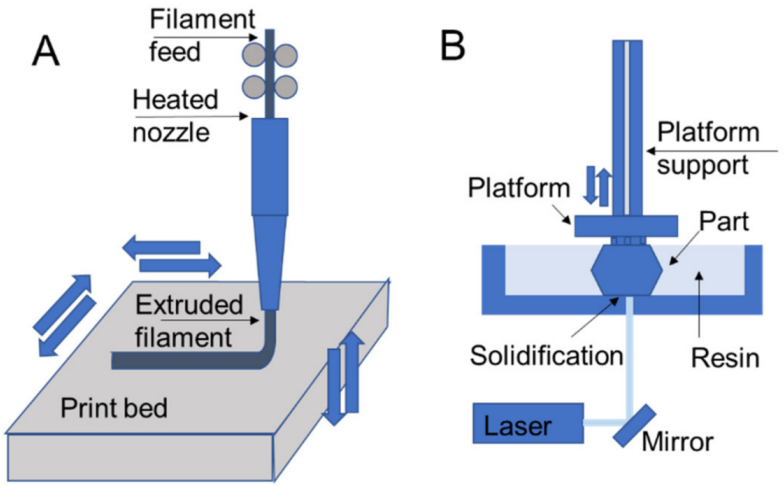

Figure 2.1: 3D printing schematics for (A) fused deposition modelling, (B) stereo-lithography. Reprinted from[22].

light, which is known as stereo-lithography [20, 21], and others use heat to make the material molten, which enables the AM layers to adhere to one another. This type of process can be further broken down into types that either melts the layer after the raw material has been deposited, or uses deposition of molten material as a means of binding the new layer to the previous ones.

The AM methods depicted in Fig 2.1 are popular with hobbyists, as these machines are cheap to run and over recent years have increased print quality via high resolution printing [23, 24] and have enabled other industries to improve their AM processes.

With the thesis topic in mind, these methods of AM have been utilised to produce microwave components by a post-process called materialisation, one example of which is that of Betancourt et al. [25], who has designed a double-ridge horn antenna that is optimised for ultra-wideband frequencies, shown in Fig 2.2. Using stereo-lithography when manufacturing this part, the authors were able to make it into a monolithic block which mitigates the inaccuracies of the more widely used technique, that of subtractive machining. This is also shown by Jacobs et al. [26],

who demonstrates that the tolerances within the design can cause gaps when assembled together to create a double-ridge horn antenna, since voids are present which result in unwanted resonances occurring, as shown in Fig 2.3.

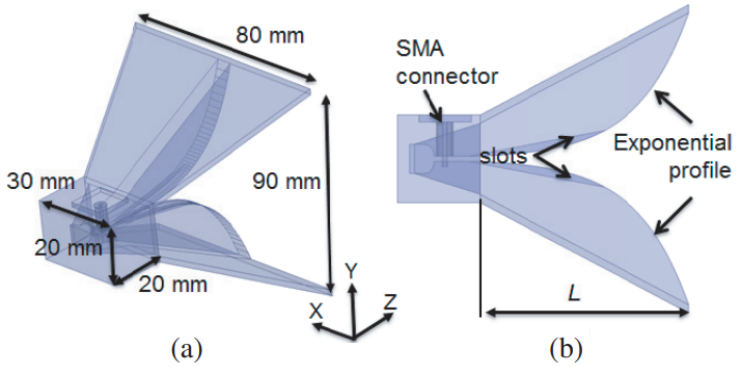

Figure 2.2: (a)Perspective view of double-ridge horn antenna and (B) cutaway view [25].

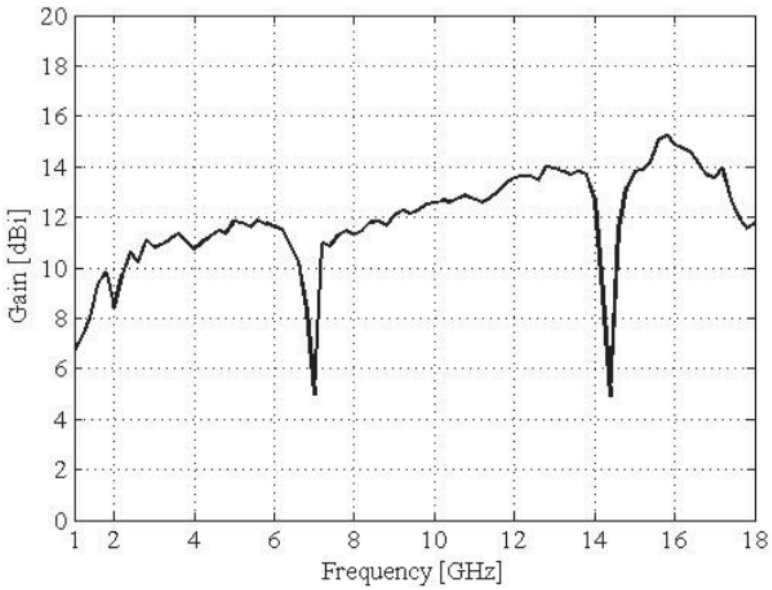

Figure 2.3: Boersight gain of machined antenna with ridge-bush gap. Reprinted from[26].

These resonances shown in Fig 2.3 occur at approximately 7GHz and another at 14.2GHz. Gaps are present at the ridge-bush gap in both bottom and top ridges with widths of 0.045mm and 0.05mm, respectively, and with a length of 10mm and 5mm. This is compared against Betancourt et al. [25] in Fig 2.4, who uses a monolithic block with only one resonance due to the ridge separation of the design. However,

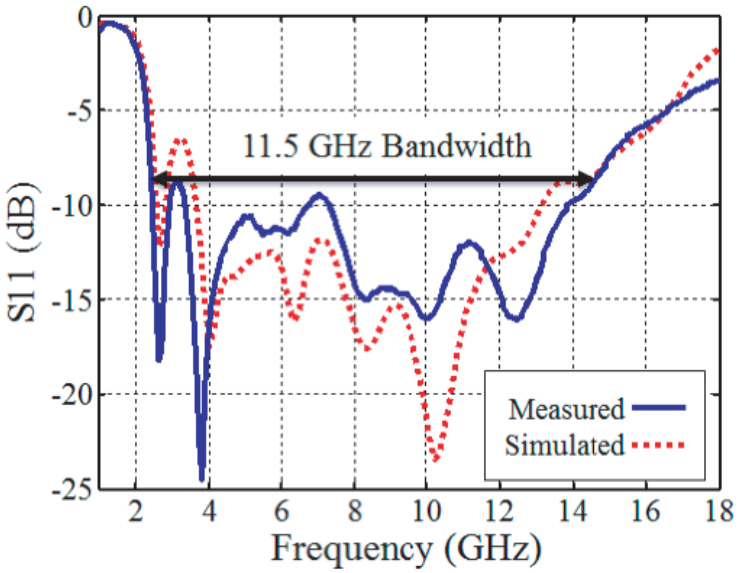

Figure 2.4: Return loss parameters of AM double-ridge horn antenna. Reprinted from[25].

due to the fabrication accuracy, the separation narrows leading to an improvement in the performance at 3GHz.

There are many studies [27, 28, 29] (including the ones above) in which AM is tested against the more typical manufacturing process of waveguides and antennas based on traditional subtractive manufacturing techniques. However there are many additional factors that can affect the performance of AM when used for certain designs, such as a waveguide, for example build orientation.

One of the largest areas of interest of AM for passive microwave components is metal powder based systems. One of these is PBF, which uses metal powder layers which are melted via a high powered laser, combining with the previous layer [30, 31]; with each layer being melted together, a 3-dimensional object is created. To prevent oxidation, the process occurs within a chamber filled with nitrogen gas[32, 33] and a representation of this process is shown in Fig 2.5

One of the greatest potentials for PBF is for passive microwave devices due to

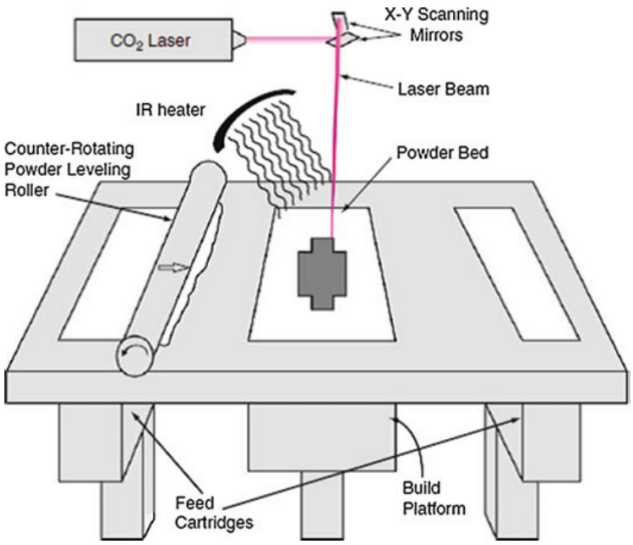

Figure 2.5: Schematic of PBF. Reprinted from[32].

the fact that PBF produces a near fully dense part with up to 50% weight reduction over traditional manufacturing techniques [34, 35, 36]. This opens up possibilities to utilise PBF as a means of creating novel structures that microwave devices can take advantage of due to the associated free-form nature of the build [37, 38].

2.1.2 Application to Passive Microwave Devices

There are many applications and sectors where microwave devices can be used when combined with AM techniques, which also allows them to be built into structures as part of an assembly. This is very attractive to the aerospace industry as a means of reducing the payload weight [39][40]; companies such as Airbus have adopted this method for producing aircraft components.

When looking at development in this sector, the starting point would be [41] Airbus' fifth order cavity filter using Selective Laser Melting (SLM), which utilises the build freedoms with SLM and iris shaping techniques to minimise the losses in the filter. When measuring the untreated PBF part, it achieved 40% - 50% of

the theoretical maximum unloaded quality factor (Q), though measuring the same structure which had been build using more traditional methods achieved 50% - 80% of the theoretical maximum unloaded Q. The large disparity between these measurements was claimed to be due to the poor surface finish inherent in the SLM process. Improving the surface finish via a chemical polishing increased the theoretical unloaded Q of the PBF part up to 75%, which showed that the surface roughness had a large impact on the performance of the filter. Booth and Lluch [42] have also used SLM to create a 5th order cavity waveguide filter using super-ellipsoid cavities. These gave a lower Q for the same eigenmode resonances, but which allowed the coupling structure to be more compact, which improved the overall filter Q for a given far-out-of band response.

Another showcase device is presented Booth et al. [43], using AM to manufacture a Ortho Mode Transducer, which is among the most complex components to be manufactured for feed chain antennas. Though the increase in surface roughness due to AM had an effect on the overall performance of the device via increased losses, the inclusion of post-build silver plating was able to reduce these losses. The use of AM negates the need for flanges and interconnections which would have been present otherwise, realising the design monotonically and resulting in a saving of further losses which would be present due to these interconnects. Kilian et al. [44] has unitised PBF to create a Ku-band feed cluster of 18 feed chains operating at Tx and Rx frequencies, shown in Fig 2.6 and made a from single print. Different approaches to building antennas are adopted due to the varying waveguide lengths which are used. Examples of ellipsoidal structures to reduce losses but still maintain the wave propagation properties are described in [41, 42]. Other manufacturing considerations related to mitigating high losses include orientating the builds to limit the amount of downward facing areas, which resulted in improved manufacturing accuracy and lowered surface roughness; all of these are part of the trade-off between

RF performance, manufacturability, accommodation and mass.

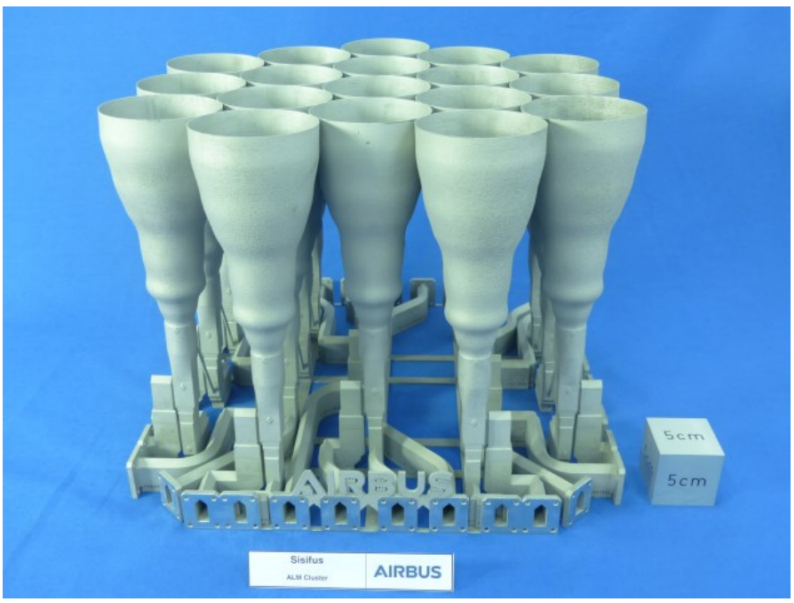

Figure 2.6: Monolithic Ku-band Tx/Rx feed cluster. Reprinted from[44].

Companies such as Airbus have also performed studies regarding the use of AM for space applications, where they have designed a resonator at 10GHz to investigate the actual RF temperature stability over a range from room temperature to around +150 °C, as temperatures in orbit range from 15-85°C. The resonator they used is a dimpled spherical resonator, that showed high Q characteristics due to interrupting the surface currents of the spurious modes [45]. Different materials were used with AM to build these resonators, which were invar alloy, Ti-6Al-4V alloy (Ti64), Ti-Nb-Ta-Zr beta-titanium alloy (TNTZ), Zr702, and the aluminium-copper alloy A20X. A20X was specifically used as a reference material as it had similar properties to aluminium alloy. With AM the temperature stability was found to be improved for Ti64, Zr702 and TNTZ, though A20X did not show this characteristic. Due to the difficulty of fabrication of Ti64, Zr702 and TNTZ parts through traditional methods, the use for AM can be seen as an important step into using otherwise difficult to handle materials as a means of producing microwave parts. Other studies include as Montejo-Garai et al. [46] who compared the Computer Numerical Control (CNC) manufacturing technique with AM and Selective Laser Sintering (SLS) by

building mode transducers shown in Fig 2.7, which are a classic component within the microwave engineering space [47]. Owing to their inherent surface roughness, AM components showed differences compared with their simulated CNC counterparts; though they did not perform as expected due to the introduction of seams within the design, they did exhibit the main characteristics of a mode transducer.

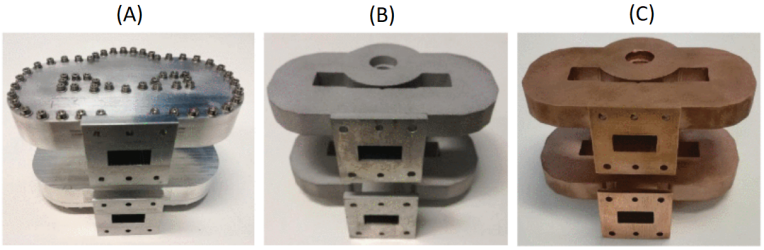

Figure 2.7: Manufactured mode traducer where A) is CNC milling B) is AlSi10Mg and C) is CuNi2SiCr. Reprinted from[46].

Studies into the use of different powders for AM parts have also been investigated by Cailloce et al. [48], who has published studies on spline horn antennas using both aluminium and titanium alloy powders. These are optimised for low mass using thin walls and a mesh structure that reduces the mass by 50%, depicted in Fig 2.8. Also, a cluster of Ku-band spline horns were made which had a mass of 2.4kg and had a reduced mass of 30%, with only 800g for the optimised structural part. Talom and Turpault [49] use different powders for microwave components for AM applications, in this case a waveguide. This study found that the use of titanium (Ti6Al4V) resulted in a lower surface roughness than using an aluminium (AS10G) counterpart, which resulted in a frequency shift within the waveguide filter. However, due to the lower electrical conductivity of the titanium part, there were higher losses within the waveguide.

Peverini et al. [50] studied the effects of rotating their waveguides while building to minimise the effect of overhang, which are the leading cause for a rougher surface finish. In this study, however, changes to the chambers of their 6th order waveguide filter (so that they were 45° downward facing shown in Fig 2.9) meant that this had

Figure 2.8: AM manufactured Ku-band spline horn antenna. Reprinted from[48].

a similar effect, so that a reduction of support structure was needed, which would save on cost per print. The use of angling the AM print is also not just relevant to waveguide as in the study carried about by Addamo et al. [51]; they went on to demonstrate the benefits of changing the orientation within the build volume for their feed horn antenna and paired this with the layering properties of PBF to create a smooth surface via the stepping of the layers when under heat.

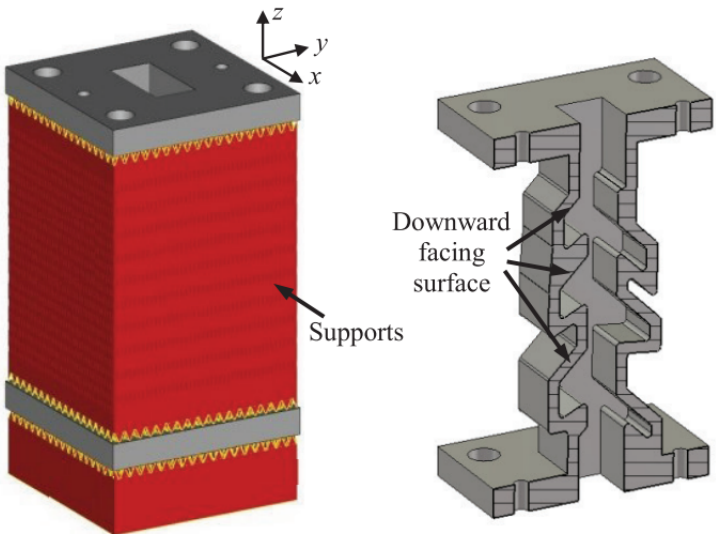

Figure 2.9: Sixth order filter, with z axis cross-section of the filter, showing the down facing sections. Reprinted from[50].

Hollenbeck et al. [52] used both AM and CNC to fabricate a set of off the shelf waveguides and measured the attenuation constant to evaluate their performance: Unsurprisingly, the commercially purchased waveguide came out on top, with the

lowest attenuation constant, though this is also due them being made from a higher conductivity material (copper and silver), in comparison the others which were all made of aluminium alloy parts. The CNC parts, however, showed similar attenuation constants, which implies that an increase in surface roughness due to the SLM process had a similar impact to attenuation as the seam along the H-plane of the CNC part.

At the Centre for High Frequency Engineering at Cardiff University, there have been ongoing investigations into PBF. They pioneered microwave methods to characterise these materials and investigate their microwave performance so that a better understanding can be obtained. These differ from other studies, where large-scale approaches have been used, such as measuring whole transmission line components as mentioned above. Gumbleton, Hefford, Clark and Porch have pioneered the approach of measurement of flat samples, which are assessed in a variety of different test fixtures.[53, 54, 55, 56]. Multiple types of materials were studied to show the effect of build orientation, the materials chosen being aluminium alloy (AlSi10Mg), Titanium alloy (Ti6Al4V) and cobalt chrome alloy (CoCr). This study showed that the samples built in a vertical orientation had a larger loss by a factor of approximately 2-3 when compared with the ideal bulk metal counterpart; additionally, horizontally built parts showed only to have a loss of factor increase of approximately 1.1-1.5. This approach extends through this thesis, ensuring coverage of different types of scenarios which could occur within the build chamber. A major finding with this study was that microwave performance of a metal surface cannot be deduced via a simple roughness value, but instead requires the spectral distribution as roughness with a certain wavelength applied to the surface ignores these large features and so spatial roughness should be considered.

2.2 Surface Roughness and Microwave Losses

Surface Resistance (R_s) is a key factor when evaluating the performance of metal surfaces at high frequencies since microwave currents flow at or near the surface of a metal. It was shown that in many instances that the manufacturing process contributes a large proportion to R_s [57, 58, 59, 60, 61, 62, 63]. Understanding the basic material properties is very important, so that the study of different manufacturing techniques and processes can be optimised for microwave applications. R_s can be defined as the real part of the ratio of tangential components of the electric and magnetic fields at a metal surface[64, 65] and physically it is the power dissipated per unit area of the parallel magnetic field at the surface of a metal; this characteristic is going to be used throughout the thesis to characterise the surface of metals. The use of Maxwell's equations can be used to show the importance of key variables that affect R_s, which are common design variables for microwave devices, namely frequency f and conductivity σ, via the well-known formula

$$R_s = \sqrt{\frac{\pi f \mu_0}{\sigma}} \tag{2.1}$$

where μ_0 is permeability of free space (H/m), f is the operating frequency (Hz) and σ (S/m) is the electrical conductivity of the material. Though Rs has the units of Ohms (Ω) it should be noted that the bulk resistance (R) of a material is a different parameter owing to where currents flow. The DC value of R arises from the current which flows across the entire cross-section of a metal object, where R is from the current that flows near the surface of a metal object. This given region over which the current flows has depth called the skin depth (δ). This phenomenon, known as the skin effect, is the reason for R_s, having such an impact on losses, as

alternating currents are concentrated near the surface. This causes these areas to have a high current density, of which 63% of the current resides within a thickness t$\leq\delta$. The skin depth of a metal can be expressed as

$$\delta = \sqrt{\frac{1}{\pi f \mu_0 \sigma}} \tag{2.2}$$

so that

$$R_s = \frac{\rho}{\delta} = \frac{1}{\sigma\delta} \tag{2.3}$$

2.2.1 Surface Roughness

Surface roughness is widely known to have an impact on the performance of microwave devices. One of the first widely known examinations into surface roughness is that of Morgan in 1949[58]. This study considers a grooved surface to demonstrate an increase in loss with increasing roughness, characterised by the RMS roughness value, R_q. This study concluded that the flow of transverse current across triangular and square profiled grooves significantly increase the losses when the features are of the same scale as the skin depth. Some examples of skin depths which would occur during measurements taken within this thesis are at frequencies of 2.8GHz, 5.8GHz and 8.9GHz and one metal that was measured was copper which has a conductivity of 57$\times$ 10^6 S/m , so by applying this to Equation 2.2 we obtain values for skin depths of; 1.26μm, 0.88μm and 0.71μm, respectively.

To provide guidance for design, Hammerstad and Jensen [66] uses Morgan's results to develop one of the most widely adopted surface roughness models for microwave loss estimation. This method was one of the first models to introduce a correction factor that employed an attenuation coefficient for transmission lines that

took into account of the roughness of the surface. Whilst the models of Morgan, Hammerstad and Jeson's are useful and widely used for copper striplines, they are limited to lower microwave frequencies around 5GHz and below[67]. This is due to the over-saturation of R_s as frequency increases. These models laid the foundation for how Electromagnetic (EM) applications use surface roughness for simulation [68] (for example, EM simulation packages like COMSOL).

Clark et al. [53] performed simple 2d finite element model simulations of triangular grooves of varying heights and also widths, whilst applying a perpendicular current flow to simulate extreme features to observe their effect on losses. These features are shown in Fig 2.10; when at these extremes, current flow is not impeded by these roughness peaks. Furthermore, the analysis of the relative loss shown in Fig 2.11 shows a relationship between the width of the feature (b) and the skin depth. Maximum losses can be observed when the peak roughness is around 3 times larger than the skin depth. However, when at extreme roughness widths, it can be observed that the microwave losses can be approximated to be an ideally flat sample. This study outlines the importance of how in reality using R_q may be inaccurate when predicting losses and where a cumulative distribution may be a better solution to calculating high frequency losses than R_q.

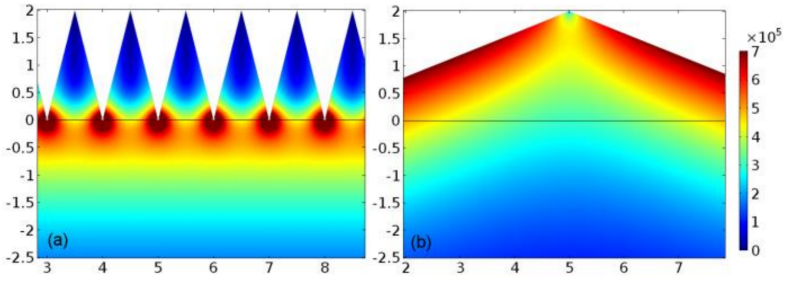

Figure 2.10: Simulation of induced current density (A/m^2) at 5.7GHz for a) feature with of 1μm and, b) feature width =10μm. Reprinted from[53].

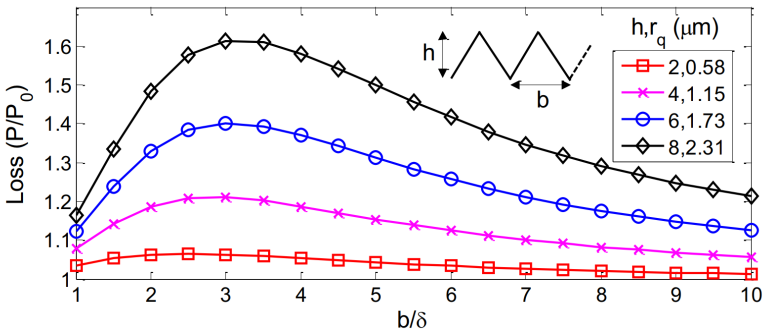

Figure 2.11: Simulated relative surface losses of the width of a 2D triangular corrugated surface relative to the skin depth, where P/P_0 is the loss when looking at power in vs power out, h is the height of the feature and r_q is the root-mean square of the surface roughness. Reprinted from[53].

2.2.2 Loss Measurement Techniques

There are a plethora of methods to evaluate R_s using cavity resonators, which are well represented within the literature. Two well-established techniques are the 'end wall' replacement of a cavity resonator structure[69, 70], and another method uses a dielectric resonator (DR) which can take many forms [71, 72, 73, 74, 55]. The Hakki-Coleman-type DR has the dielectric terminated with a flat sample under test on both ends, and this method tends to be favoured for high conductivity samples because of its high accuracy. This is due to dual termination, as it makes the structure produce a deterministic solution for the field equation[75].The problem with this, however, is that due to the use of two samples (shown in Fig 2.12) the results for R_s will be an average of the two samples.

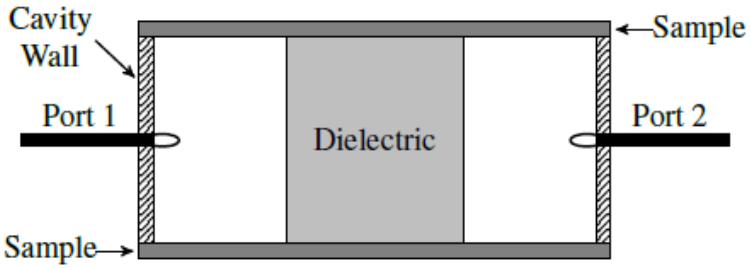

Figure 2.12: Hakki-Coleman Dielectric Resonator. Reprinted from[76].

For a DR a low loss dielectric material (e.g. sapphire) is used in close proximity to a sample plate, which makes the sample have a far greater influence over losses as it relies on the tangential magnetic field at the conductor surface; this can be expressed in terms of the conductor quality factor.

$$Q_c = \frac{\omega\mu_0 \iiint H^2 dv}{R_s \iint H_t^2 ds} \tag{2.4}$$

Where Q_c is the quality factor associated with the conductive surfaces and ω is the angular frequency (rad/s), μ_0 is is the permeability of free space within a vacuum and H and H_t is the magnetic field present within the volume of the DR and the tangential magnetic field applied to the surface of the DR, respectively. Although DRs have very high Q factors making them very suitable for the task of measuring surface resistances, when specifically measuring PBF where there are many factors a DR cannot measure due to only being able to measure properties isotropically owing to the circular currents induced in the sample end walls, which produces a surface average measurement for R_s. An alternative solution (which can analyse anisotropic features) will be described in Chapter 3, which is based upon a coaxial resonator.

2.3 Broadband Microwave Measurements

There are many R_s measurmenst using broadband structures for assessing the characteristics of the material over a range of frequencies; the most common application of these structures is to investigate the dielectric behaviour of materials. Some of the earliest work was done in 1951 by H.F Cook [77], who used a coaxial line to measure samples from 1GHz to 30GHz. This method of coaxial line measurement has been used in many other applications, where a coaxial line has been made into

resonant structures and used to measure liquids [78, 79, 80] and powders [81, 82]. The most common application of a coaxial structure is an open ended coaxial line, which was developed by J R. Mosig [83] in 1981. This uses its near radiant Transverse Electro-Magnetic (TEM) field to act as a probe as the reflected TEM field propagates back along the line and is dependent on the dielectric properties of the sample terminating the line. This probe technique is also used to measure a variety of materials, especially biological samples [84, 85, 86] as it is a non destructive type of measurement[87, 88] that uses low-power microwaves. Other methods of broadband measuring techniques have been used to measure dielectrics, one of which will be discussed later within this thesis, namely the Fabry Perot open resonator (FPOR) [89]. This open resonator technique showed a Q factor of 120,000 with an error of approximately ±0.25% in these measurements carried out between 9-9.5GHz when measuring a dielectric sample . There have been recent improvements and optimisation of this technique and now it is used from frequencies of gigahertz to terahertz frequency bands [90, 91, 92, 93, 94]. Test fixtures at optical frequencies are called a Fabry–Pérot interferometers, as semi-reflective surfaces which allow light to pass through the mirrors are used to create a path length difference between subsequent transmitted waves and are then recombined with a focal lens [95, 96]; an example of this can be seen in Fig 2.13.

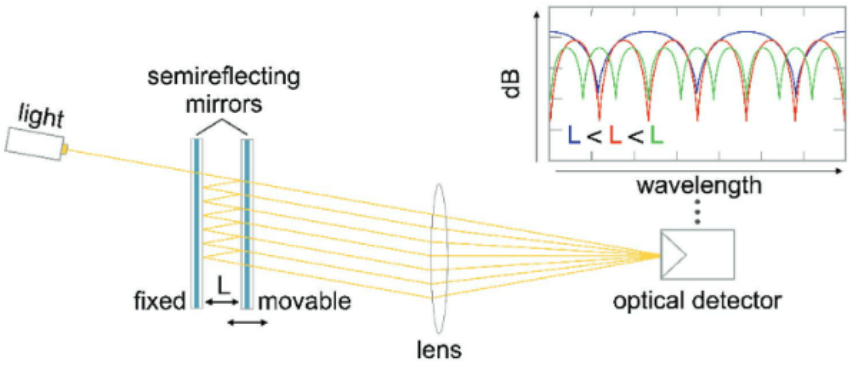

Figure 2.13: Depiction of a general principle of a white light Fabry Perot interferometer[97].

2.4 Parameters Relating to PBF Relevant to Microwave Performace

It is important to consider the parameters of PBF for the use of microwave applications. There are a plethora of parameters which can be changed (e.g layer thickness, laser power, build orientation, etc.) which all can affect the surface quality of the PBF part. Through this thesis, there is only one machine that was used to create the PBF samples which can be seen in Fig 2.14; however the properties and parameters tested can be universally applied to those of other AM machines from other manufactures.

Figure 2.14: Renishaw AM250 machine which uses the PBF manufacturing process.

2.4.1 Powder Properties

The material of interest throughout this thesis is AlSi10Mg aluminium alloy powder. These powders have a high concentration of silicon within the alloy powder to help improve the fluidity of the melt pools which occur when the laser melts these layers together, with the addition of magnesium to improve the strength of the alloy[98]. Metal powders used for PBF are manufactured with a process called atomisation. This process uses an inert gas to break up the molten metals, which also serves as a way to freeze them when the powder has formed. Free fall nozzles are also used, as these create small spherical particles, which are then cooled with gas. The particles falls is around 50-150mm until they land and are collected[99].

This virgin powder otherwise (known as ”raw” powder) is very expensive, so efforts to recycle it are made for economic reasons. This process ensures that any large particles above a threshold value do not make their way into other prints as this can cause defects within them, as the increase in particle size may be larger for the layer thickness, meaning that there will be a large displacement of powder in subsequent layers. Also, due to the increased size, the laser may not melt this larger ‘clump’ of powder, which may lead to issues with the mechanical integrity of the print[100].

2.5 Post Processing

Post-processing is an important part of the PBF process for microwave devices. These parts still require post-processing due to their inherent surface roughness, although development into building parameters designed to improve surface roughness has come along way since PBF was first used to fabricate microwave devices.

2.5.1 Highly Conductive

Plating High conduction plating (e.g. with silver) is a common way to lower the surface resistance of microwave parts, and also a common way to overcome some of the high losses associated with AM when compared against other more traditional manufacturing techniques[101, 50]. Plating microwave devices has many advantages but also disadvantages. Some advantages are that when the plating thickness is thicker than the skin depth at the operation frequency, the part will have the characteristics of the material used for plating due to the fact that all the currents are residing within the plated material's surface[102, 103]. Another advantage of plating is that its liquid-like nature allows for plating the material to fill the imperfections along the surface of the material [104, 105], which reduces the surface roughness. The downside to plating PBF parts, aside from the additional cost and time needed for this process, is reliability. As AM is being proposed for aerospace applications, the environment to which parts are exposed is extreme, from extremely cold temperatures to extremely hot temperatures over a matter of minutes. With this in mind, thermal expansion of these materials needs to be considered, as in some cases parts have been known to separate due to the different expansions of both materials used; clearly, this could result in a failure of the plating[106].

2.5.2 Deburring

Burrs are an undesirable and unavoidable product of most manufacturing methods because of the plastic flow of material[107, 108], such as cutting, forming, blanking and shearing. A burr is defined as a projection of undesired material beyond the desired machined feature[109]. From this definition of a burr, we can also apply this to PBF, as the material beyond the defined features of PBF such as the powder that

has been bound to the object via the melt pools.

Deburring is performed with the use of a CNC machine which enables precise deburring and chamfering of holes, flat and curved surfaces[110]. This deburring using can achieve a mirror-like finish with a surface roughness of 0.5μm to 1.5μm [111]. Media tumbling is another post-processing method which is used for PBF parts, as it enables treatment of the interior cavities of builds which processes like CNC may not be able to reach. The uses of different media when tumbling allows for different abrasive properties. Stainless steel shot has been used to reduce the RMS surface roughness, by 25% after 2 hours and by 36% after 8 hours of tumbling[112]. This is just one of many types of media available for surface treatment. Bead blasting in another form of post-process, which fires small particles at high velocity, to remove the top layers of the part. In PBF this means that it can remove loose powder or protrusions present, which may have been created from support material[113]. Both tumbling and blasting may be expected to decrease R_s since both introduce mechanical damage near the surface in the form of material dislocations.

Chapter 3

Theory and Methods of Microwave Surface Resistance Measurement

3.1 Introduction

Chapter 2 described the evaluation of PBF for specifically designed microwave applications, such as waveguide filters. However, this choice is somewhat interesting as all measurements taken are of the average surface resistance of either the entire microwave part or of a singular surface. This is important to note as the surface performance of PBF is worse than other alternatives, such as CNC machining. Evaluating AM components by manufacturing them and testing them is not only very time consuming due to the time taken to design and build these structures, but also very costly. In addition, a full understanding of the characteristic of AM for microwave applications, is not possible since there are have many factors that affect the performance of such parts, such as print orientation of parts as each surface may have a different surface resistance values and contribute to the losses differently

and can't measured separately due to the measurement being of the average surface resistance of a wave guide. So with this in mind, rather than manufacturing a large structure to evaluate the performance of PBF, methods have been developed that utilise small samples so that measurements of R_s can be done which reduce the cost of a sample but also with reduced lead times for all measurements. Another added benefit is that by using small samples, a better understanding can be gained as one can change the parameters of these build parts such as build orientation, as you have much more control on what samples will be and their properties when compared to manufacturing a waveguide, which is restricted by the fundamental geometry of the waveguide, such as orientation on the build plate. In Chapter 3 methods will be proposed for the evaluation of PBF for two established techniques: the Fabry Perot open resonator (FPOR) and the coaxial resonator(CR). Both of these methods use a specially designed sample to achieve measurements of R_s but both have disadvantages and advantages, as will be discussed. The third method, however, is a novel technique that uses an end-plate replacement, which simplifies the manufacturing process of samples. Chapter 3 presents background to microwave resonance and loss quantification, with the explanation of these three methods to evaluate R_s for PBF with the aim of achieving broad-band measurements using a single structure and the use of one test sample, which not only reduces the number of samples needed, but also reduces time taken for these to be evaluated.

3.2 Microwave Resonance and Loss

As previously mentioned in Chapter 2.2, the current that flows at microwave frequencies is predominantly along the surface of a good conductor, where the thickness of this current-carrying region is called skin depth δ . Skin depth can be analytically derived for a good conductor via the EM wave equation; this derivation can be found

in[114]. A overview of this starts with Maxwell's curl expressions for a medium with conductivity σ.

$$\nabla \times \overline{E} = j\omega\mu\overline{H} \tag{3.1}$$

$$\nabla \times \overline{H} = j\omega\epsilon\overline{E} + \sigma\overline{E} \tag{3.2}$$

where $\overline{H}$ and $\overline{E}$ are the magnetic and electric fields respectively and $\sigma\overline{E}$ represents the conductor current density, ω is the angular frequency ($2\pi\ f$), μ is the magnetic permeability, ϵ is the electric permittivity. Equations 3.1 and 3.2 result in a wave equation for $\overline{E}$

$$\nabla^2\overline{E} + \omega^2\mu\epsilon\left(1 - j\frac{\sigma}{\omega\epsilon}\right)\overline{E} = 0 \tag{3.3}$$

The propagation γ constant can then be defined as

$$\gamma = \alpha + j\beta = j\omega\sqrt{\mu\epsilon}\sqrt{1 - j\frac{\sigma}{\omega\epsilon}} \tag{3.4}$$

where α is the attenuation constant and β is the phase constant (sometimes called the wave number). If the assumption is made that $\overline{E}$ only has an x component which is perpendicular to the direction of propagation (z) (ie. TE) the solution becomes

$$\overline{E}_x(z) = E^+e^{(-\gamma z)} + E^-e^{\gamma z} \tag{3.5}$$

The $H_y(z)$ field can be derived in the same way. When $\sigma \gg \omega\epsilon'$ as there is an exponential decay of amplitude with distance and $\mathrm{Re}(\gamma) = \sqrt{\omega\mu\sigma/2} = 1/\delta = \alpha$. The wave impedance ($\eta$) for plane wave propagation of a good conductor can be expressed as $\eta = (1+j)\sqrt{\omega\mu/2\sigma}$. R_s is the real part and quantifies the microwave losses that determine performance of the devices, In this context losses are the power dissipation at the surface of the conductor when in the presence of a EM field, which can be expressed as

$$P^t = \frac{R_S}{2} \int\int_s |H_S|^2 dS \tag{3.6}$$

where S is the surface on which the current flows and H_S is the tangential magnetic field. It is also important to note that R_s has a dependence $\sqrt{f}$ on frequency and so any change to frequency results in a change of R_s and furthermore the power dissipated is proportional to $\sqrt{f}$. However there are also losses linked to surface finish. As these are not material bound, we intrduce an effective R_S and hence an effective value of conductivity σ_{eff}. This then means that losses associated with the conductor can be attributed proportionally to R_s, with R_s being the measurement metric for losses at microwave frequencies, including additional surface roughness effects. With this understanding, it is then important to look at not only material choices for microwave applications, but also the processing and methods of the materials as surface finish also plays an important role in the overall R_s.

3.2.1 Microwave Resonance

Within this thesis, different types of microwave resonators are used to investigate the losses of PBF parts. The use of a resonator can provide a sensitive instrument for

measuring loss in particular, which can assess the effects of surface/material properties. Another benefit of this approach is the relative size of these structures, as the more basic structures tend to be of around half the size of their operating frequency wavelength. Due to their relative simplicity, most resonator based techniques are easily scaleable and easy to fabricate.

For a resonant condition to occur within a microwave cavity the electric and magnetic field stored energies need to be equal, so that the resultant impedance is purely real, hence R_s can be extracted with the use of certain techniques. The unloaded Q factor of a resonator can be defined by the stored energy and the power loss as shown in Equation 3.7, and this is the starting point to quantifying the loss.

$$Q_0 = \omega_0 \frac{\text{Avrage stored energy}}{\text{Energy loss / Sec}} = \omega_0 \frac{\langle W \rangle}{\langle P \rangle} \tag{3.7}$$

If the assumption is made that any dielectric present within the resonator is lossless, the energy loss can be given by Equation 3.6 as all losses are then from the conductive cavity walls. The average energy stored within the cavity can be defined as

$$\langle W \rangle = \langle W_m \rangle + \langle W_e \rangle \tag{3.8}$$

where

$$\langle W_m \rangle = \frac{1}{4}\mu \iiint_V |H_V|^2 dV \tag{3.9}$$

$$\langle W_e \rangle = \frac{1}{4}\varepsilon \iiint_V |E_V|^2 dV \tag{3.10}$$

where $\langle W_m \rangle$ is the average magnetic field stored energy and $\langle W_e \rangle$ is the average stored energy of the electric field. Both of these energies are stored within the electromagnetic field in the form of a standing wave, which occupies the hollow space within the cavity. Therefore, when the resonance condition is met $\langle W_m \rangle = \langle W_e \rangle$. Hence when a large Q factor is present, it indicates that the relative loss is low within the system, which would indicate a lower level of impedance and therefore a lower value of R_S.

3.2.2 Rectangular Cavities

For a rectangular resonator it is convenient to view it as a waveguide with both ends of the waveguide being shorted, thus forming an enclosed cavity. A standing wave produced within a cavity is described as the sum of two waves moving in opposite directions, but each having the same amplitude and frequency. The resonance frequencies of modes (f_{mnl}) for this resonator are simply determined by its physical dimensions. As a rectangular cavity is essentially a rectangular waveguide section with enclosed ends; it allows us to use the phase constant of a given mode(β_{mn}) to designate an expression for f_0 when each boundary condition of the sidewalls of the rectangular cavity is equal to those of a waveguide.

$$\beta_{mn} = \sqrt{k^2 - \left(\frac{m\pi}{a}\right)^2 - \left(\frac{n\pi}{b}\right)^2} \tag{3.11}$$

where a and b are the geometric factors shown in Fig 3.1, $k = \omega\sqrt{\mu\varepsilon}$ where μ and ε are the permeability and permittivity of the material that fills the cavity, m and n are the mode integers. If we apply the conditions of E_t=0 at $z = 0$ which implies that A^+ = -A^-, where A^+ and A^- are the arbitrary amplitudes for the forward and

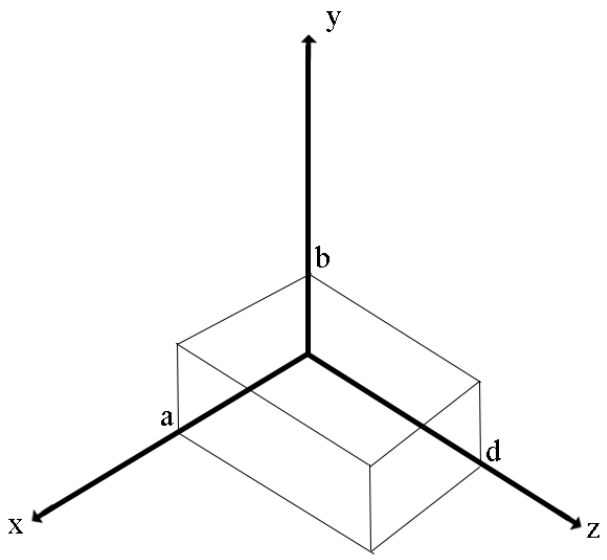

Figure 3.1: geometric representation for a rectangular cavity resonator, with internal dimensions a,b and d.

backward waves denoted by $\overline{e}$(x,y), which is as expected from a perfect conductive wall. This then means that the condition of $\overline{E} = 0$ at $z = d$ can be expressed as

$$\overline{E}(x, y, d) = -2jA^{+}\overline{e}(x, y)sin\beta_{mn}d = 0 \tag{3.12}$$

The only non trivial ($A^{+} \neq 0$) solution thus occurs for

$$\beta_{mn}d = l\pi, \quad l = 1, 2, 3, ..., \tag{3.13}$$

This implies that the cavity must be of an integer multiple of a half wavelength long at the resonant frequency. For this no trivial solutions are feasible for other lengths, or for frequencies other than the resonant frequencies. This then means that a rectangular cavity is a waveguide version of a short-circuited $\lambda/2$ transmission line.

So the resonant wave number ($knml$) for a rectangular cavity can be defined as

$$k_{mnl} = \sqrt{\left(\frac{m\pi}{a}\right)^2 + \left(\frac{n\pi}{b}\right)^2 + \left(\frac{l\pi}{d}\right)^2} \tag{3.14}$$

We can refer to the resonance modes of the cavity as TE_{mnl} or TM_{mnl} type resonances, with the indices of the m, n, l, which refers to the number of have wavelengths which are standing waves in the x, y and z directions, respectively. The resonant frequency can then be defined as

$$f_{mnl} = \frac{ck_{mnl}}{2\pi\sqrt{\mu_r\varepsilon_r}} = \frac{c}{2\pi\sqrt{\mu_r\varepsilon_r}}\sqrt{\left(\frac{m\pi}{a}\right)^2 + \left(\frac{n\pi}{b}\right)^2 + \left(\frac{l\pi}{d}\right)^2} \tag{3.15}$$

where c is the speed of light within a vacuum (approximately $3 \times 10^8 m/s$)

3.2.3 Surface Resistance and Dielectric Loss

Previously we have shown how loss is quantified by quality factor Q_0. A ideal air-filled cavity has only conductive walls, so that

$$Q_0 = Q_c \tag{3.16}$$

where Q_c represent the losses associated with the conductive walls. However, we can introduce dielectrics into the cavity which contribute to the losses, so the overall losses can be summed as follows

$$\frac{1}{Q_0} = \frac{1}{Q_c} + \frac{1}{Q_d} \tag{3.17}$$

where $1/Q_d$ is the overall loss contributions associated with the dielectrics. With further analysis both Q_c and Q_d can be considered separately to give

$$\frac{1}{Q_0} = GR_S + P_{ed} \tan \delta \tag{3.18}$$

where G is the geometric factor (Ω^{-1}) associated with the conductive losses and P_{ed} is the dielectric filling factor [114], defined by

$$G = \frac{1}{\omega} \frac{\iint_s H_t \cdot H_t^* ds}{\iiint_V \mu_0 H \cdot H^* dv} \tag{3.19}$$

$$P_{ed} = \frac{\iiint_{Vd} \varepsilon_d E \cdot E^* ds}{\iint_V \varepsilon_v E \cdot E^* dv} \tag{3.20}$$

where S represents the surface integral of each conductive surface, V is for the volume of the cavity space and V_d is the volume occupied by the dielectric, μ_0 is the permeability of free space, ϵ_d and ϵ_v are the permittivity of the materials within the cavity.

To measure the values of Q factor, when using any structure within this thesis scattering parameters (S-Parameters) where used, with either the Keysight N5232A or E5071B. Which are transmission measurements or S_{21} as these are power measurements over 2 ports they be expressed as $|S_{21}|^2$. However as this is expressed as insertion Loss, a span of frequency shown around the resonate frequency should be

chosen so that -3dB of bandwidth can be seen as Q is expressed in Equation 3.21 due to this, the amounts of sample points of frequency required when measuring for S-Parameters should be considered so that a -3dB bandwidth can be measured.

$$Q_0 = \frac{f_0}{BW} \tag{3.21}$$

Where Q_0 is the Q factor at the resonate frequency, f_0 is the resonate frequency and BW is the bandwidth

3.3 Fabry Perot Resonator: Overview

A FPOR is an open resonator, which is mostly used for dielectric characterisation[89, 115, 116, 117, 118]. The technique exploits the use of its Gaussian mode , with the structure having a large bandwidth, typically upto 50GHz and beyond depending on the plate separation. It is suitable for the purpose of measuring PBF samples as it would enable the characterisation of samples over a wide range of frequencies so that multiple bands can be characterised with a single measurement device and requires just a flat sample.

Because open resonators have the intrinsic advantage of not having any sidewalls within the resonant structure, the Q factor is very high, which is one of the reasons why they are used for dielectric measurements. This also gives them the ability to have higher accuracy for R_s measurements of flat metal plates due to the high fidelity.

3.3.1 Measurement Theory

One of the most common configurations of a FPOR utilises two hemispherical dishes (HSD) as metal reflectors, the free space between them containing a standing wave which represents the resonance. If this were implemented, it would mean that one of these dishes would have to be made using PBF, so that we could evaluate the performance of the PBF manufacturing process. However, using an HSD manufactured by PBF each time would be very costly and would make the repeatability of the measurements very difficult to maintain, due to the complexity of the structure. Instead of using a single hemispherical PBF reflector, a flat plate was chosen to act as one HSD and also be the sample under test, which would increase the repeatability of the measurement when many samples need to be characterised as making a HSD would increase the complexity of manufacturing the samples which could potentially lead to errors in these parts.

The FPOR resonant frequency is [119]

$$Fr_{00q} = \frac{c}{2L}(q + 1 + \frac{1}{\pi}cos^{-1}(1 - \frac{L}{R}) \tag{3.22}$$

where c is the speed of light in a vacuum, q is the mode number (an integer), L is the distance from the centre of the HSD and the plate, and R is the radius of the HSD; a depiction of these parameters are shown in Fig 3.2

To gain a better understanding of FPOR operation, the mode number was increased to investigate whether there was a drop in Q factor, and so a COMSOL simulation was performed. With the dish aperture being 148 degrees and a target frequency of 15GHz (this frequency is within the K_u band, which is what PBF

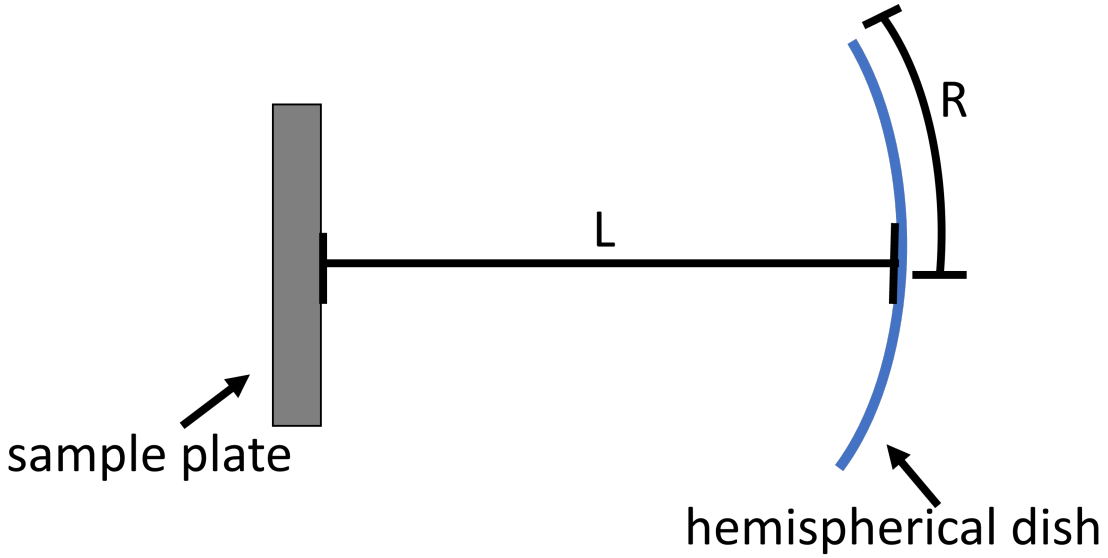

Figure 3.2: A simplified depiction of the FPOR showing the characteristic factors affecting the resonant frequency.

devices aim to achieve as this band used in satellites for video distribution, broadband internet services, and corporate network communications), the results of this simulation can be seen in Figure 3.3 below.

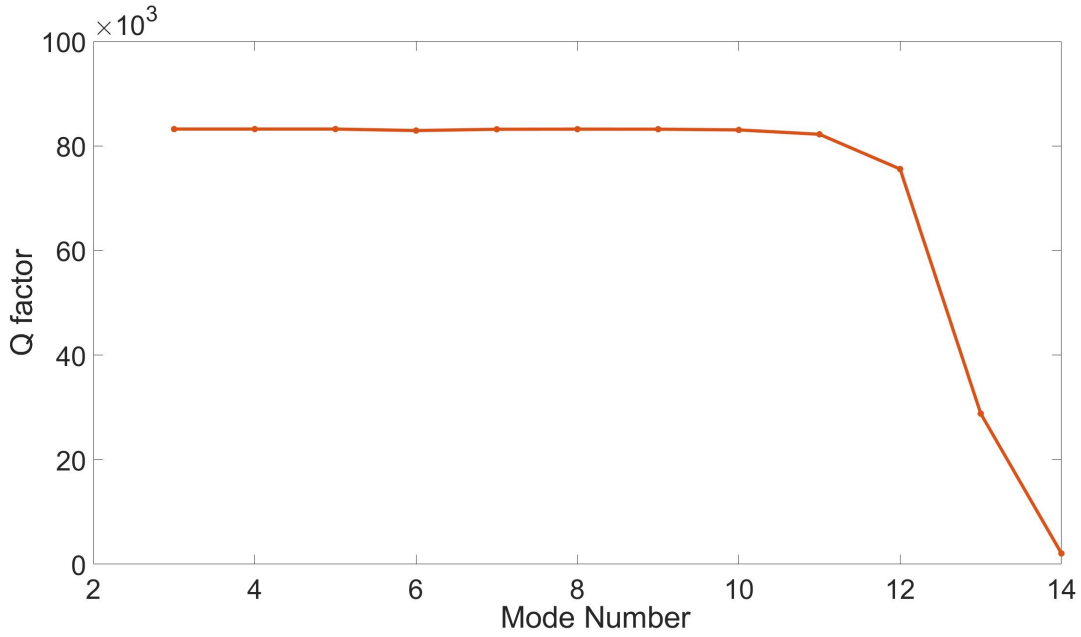

Figure 3.3: Simulation of mode order separation at 15GHz.

Referring to Figure 3.3, it is clear that when the resonance mode number is greater than 11 there is a severe drop in the Q factor. This observation is one of

the typical downsides of an open resonator if not utilised properly. The sidewalls present in enclosed cavities cause losses to occur on these surfaces; however, they do ensure that the fields are contained within the structure. In an open resonator case, if not designed properly, these fields radiate from the structure, and what we are seeing is a prime example of this when changing the mode number to a higher order, as fields are then radiating outward of the resonator causing the large drop in Q factor. Note that radiation is just another loss mechanism that causes leakage of the stored energy and thus reduces Q_0.

The consequence for measurement is that the plate separation needs to be closer than the 11 half wavelengths to ensure that there is no loss of Q factor from the radiating fields. Another outcome of these simulations was that COMSOL has limitations when computing an open resonator. When trying to design the simulation for FPOR it becomes apparent that the memory required was too much for a full 3D simulation, as systems with 64GB and 128GB of RAM with varying virtual RAM sizes and mesh sizes would not compute. To overcome this limitation, 2D simulations were used to gather results because the FPOR has rotational symmetry. This enables a 2D cross section to be used to identify resonances and the Q factor characteristics.

3.3.2 Dish Design

Other factors are not considered within the Equation3.22, such as the angle chosen for the dishes segment, which effectively changes the arc length of the dish if observing the dish on a 2D plane. So a COMSOL 2D simulation was performed with a sweeping angular aperture of the dish to observe its effects on Q factor, as this will show a suitable angular aperture that can be used in practice. The results of this simulation can be seen in Fig 3.4.

Before simulation a model had to be made. However, since there was still a need for a 3D simulation of a FPOR the decision was taken to make a CAD model that could be imported into different simulation packages such as HFFS and CST alongside COMSOL. The software used was SolidWorks, as this is one of the most popular CAD software used in industry, with features that allow integration with other software. Simulation packages like COMSOL have a package similar to SolidWorks Live Link which allows parameterisation of features within the SolidWorks model to be controlled by COMSOL when doing a parameter sweep study. Although simulations using HFFS and CST were unsuccessful in achieving a 3D simulation, slicing the model and using COMSOL again to create a 2D simulation worked successfully.

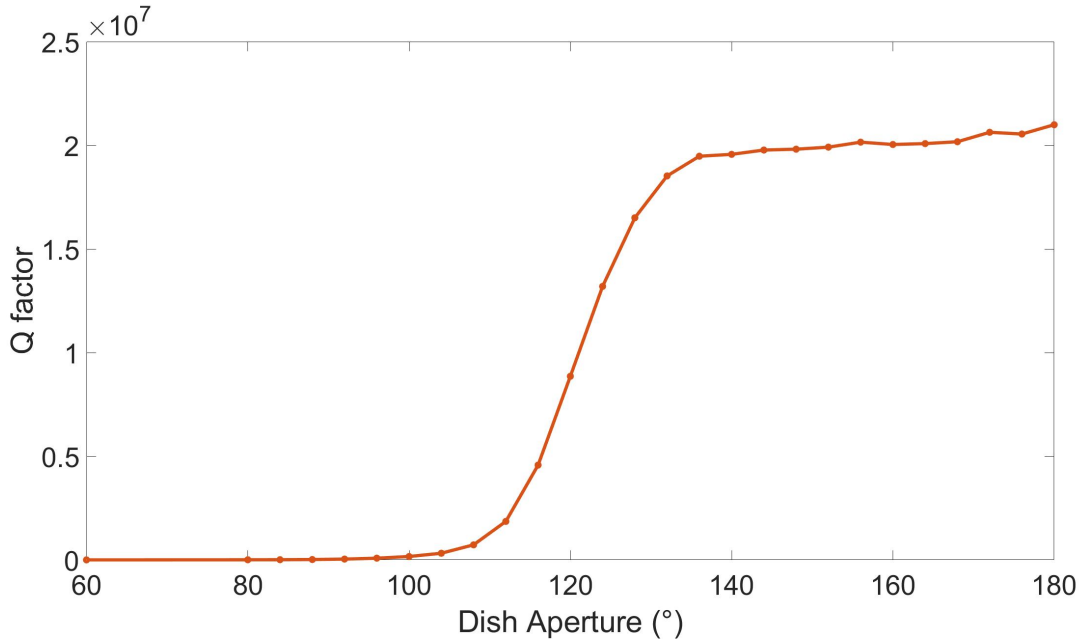

Figure 3.4: Simulated graph of Q factor when the aperture of the HSD is changed using SolidWorks Live Link.

As shown in Fig 3.4, the aperture of the dish is found to have an impact on the Q factor, as was expected due to the fact that when having a small aperture the reflection from the plate doesn't have have enough area coverage to support a standing wave. A reason for this (and why there is a sudden increase in Q factor) is that the standing wave is in fact the shape of a Gaussian beam which starts wide at the dish then narrows towards the plate; an example of this is shown in Fig 3.5,

which depicts the evolution of a Gaussian beam as it expands away from the focal point at position 0mm; with this understanding any dish angle above 140 degrees is suitable for use when using a FPOR as it can support the curvature of the Gaussian beam being produced within the structure.

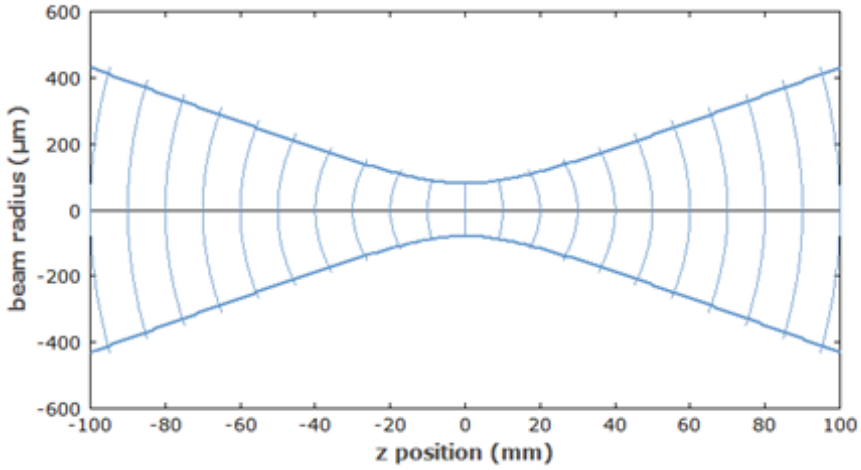

Figure 3.5: An example of the evolution of a Gaussian beam around a focal point and the curvature of the wave propagation[120].

3.3.3 Sample Design

Now that it is understood how the characteristics of the aperture of the dish and the mode selection affects the Q factor, we next consider the design for the sample plate which is suitable for FPOR. When producing a sample with PBF, the size of the part has a large impact on how many samples can be built on a single build plate and so to produce a sample set many prints have to be run, which is both time consuming and costly. An understanding regarding sample size is important to gauge the appropriate size needed for the characterisation using FPOR. This study was achieved by increasing the sample size in increments of 20mm, done as a 2D simulation, resulting in a circular part when extrapolated to a 3D simulation using the revolve tool in COMSOL.

One important characteristic of the FPOR is that the magnetic field applied to the sample is circular, as shown in Fig 3.6. This is important as it limits the type of measurement that can be done on PBF samples. The field applied in this way results in a measurement of average surface resistance. When using a FPOR to extract the surface resistance of a sample, all high-frequency losses must be accounted for, since each loss contributes to the measured (loaded) Q factor. As shown below, if the mode selection and dish angle are suitable for resonance, there is only small radiational loss, which was also found by B. B. Yang [121]. With this in mind, we can attribute these losses to the total unloaded Q_0 and express as

$$\frac{1}{Q_0} = G_p R_{S_p} + G_D R_{S_D} \tag{3.23}$$

where Q_0 is the total unloaded Q factor of the system and G_p, R_{S_p}, G_D and R_{SD} are the geometry factors (G) and surface resistance (R_s) values associated with

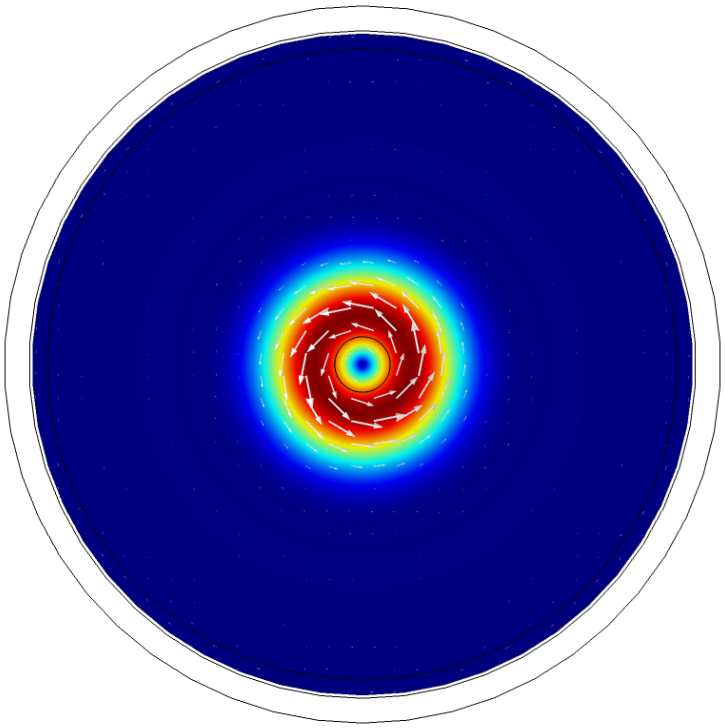

Figure 3.6: Simulation of applied magnetic field direction for the FPOR sample.

the losses of the sample plate and HSD, respectively. This equation can be used in conjunction with COMSOL to attribute these geometric losses and apply known material losses to each loss contribution so that a solution for R_{S_p} can be calculated, as seen in Equation 3.24

$$R_{S_p} = \frac{\frac{1}{Q_0} - G_D R_{S_D}}{G_p} \tag{3.24}$$

This shows how the FPOR can be calibrated for measurement of R_s on unknown samples. As the FPOR can resonate at different frequencies on changing L, multiple calibration steps need to be considered, as there may be a change in contributional losses associated with different operating frequencies.

3.3.4 Mechanical Design

Since plate separation is critical, a micrometer adjustment was implemented into the FPOR, which was achieved by boring a hole into the shaft of a micrometer and attaching it with a bolt which acted as a pin to secure the plate onto the micrometer. A nut was also used to ensure that the bolt did not fall out. As a micrometer has only a small range of movement, another coarse method was used to allow a much larger range of movement, using the extruded aluminium as the frame to slide a bracket up and down to adjust the distance of separation by a larger amount. These two adjustments allows the selection of a wide range of resonant modes.

It's important to ensure repeatability when using the FPOR and add functionality to the design that allows the changing of components such as the HSD. Having keyed slots on the HSD and each support bracket ensures that if any component changes due to replacing the HSD (to target another resonant frequency), they can be located back to the same position.

As mentioned previously a simulation package called SolidWorks Live Link within COMSOL was used for parameter sweeps of the FPOR, which utilises both a CAD model and simulation file to share the same model, which helped fine-tune and validate the functionality of the resonator. In this case, it can be used to locate the top support bracket to locate the desired frequency and use the micrometer to sweep with fine movement control allowing a much finer control over the resonant frequency.

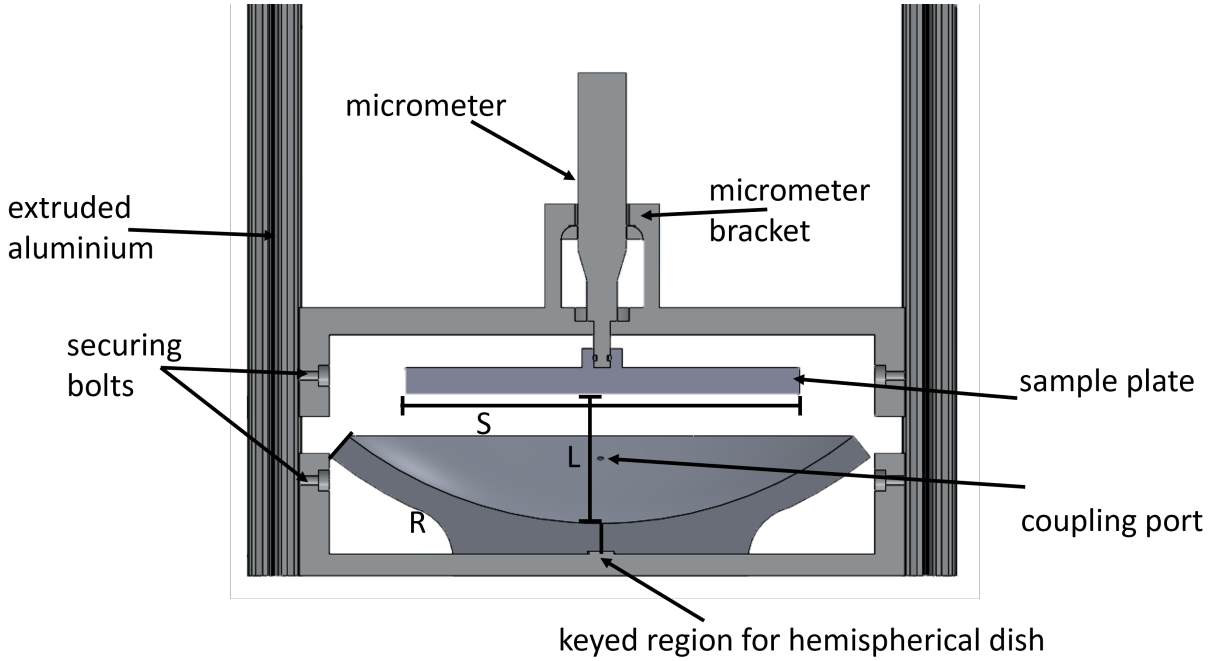

Figure 3.7: Sliced CAD view of the FPOR showing key features, where R is the radial aperture, S is the sample width and L is the separation distance.

3.3.5 Measurement

Initial testing of the FPOR resonator showed issues with the coupling locations which were within the HSD, This resulted in having a raised backwards power shown in S_{21} plot Fig 3.8 , which made tracking the resonance peak of the S_{21} response difficult as the resonator tracker program used (which tracks the shift in the resonant response with the use of Lorentzian curve fitting to find the peak of the S_{21} response) would jump towards peaks located nearby due to the high baseline caused by direct coupling of the 2 ports. To relocate this port, a sacrifice had to be made as a port was relocated within the sample plate, which reduced the range of movement as only one half rotation could be done before the relocated port hit the top support bracket, thus stopping the full rotation of the micrometer.

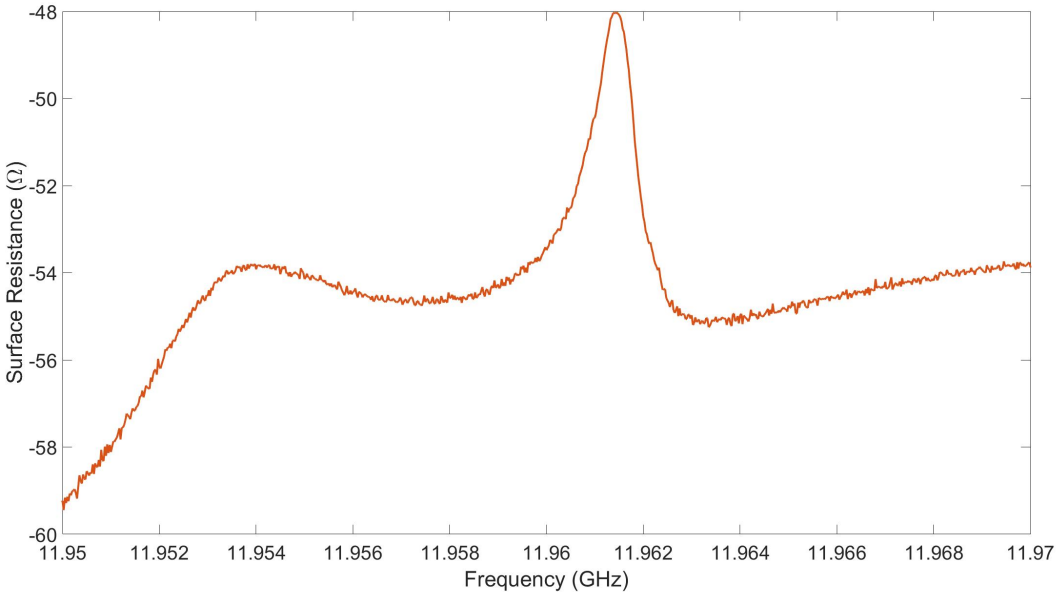

Figure 3.8: S_{21} response of FPORs high baseline when ports are located within the HSD.

This measurement was taken with the use of a Keysight N5232A network analyser. The coupling structure used 2 inductive coupling loops located in both the sample plate and HSD which can be seen in 3.9. Thus coupling into the magnetic

field present within FPOR.

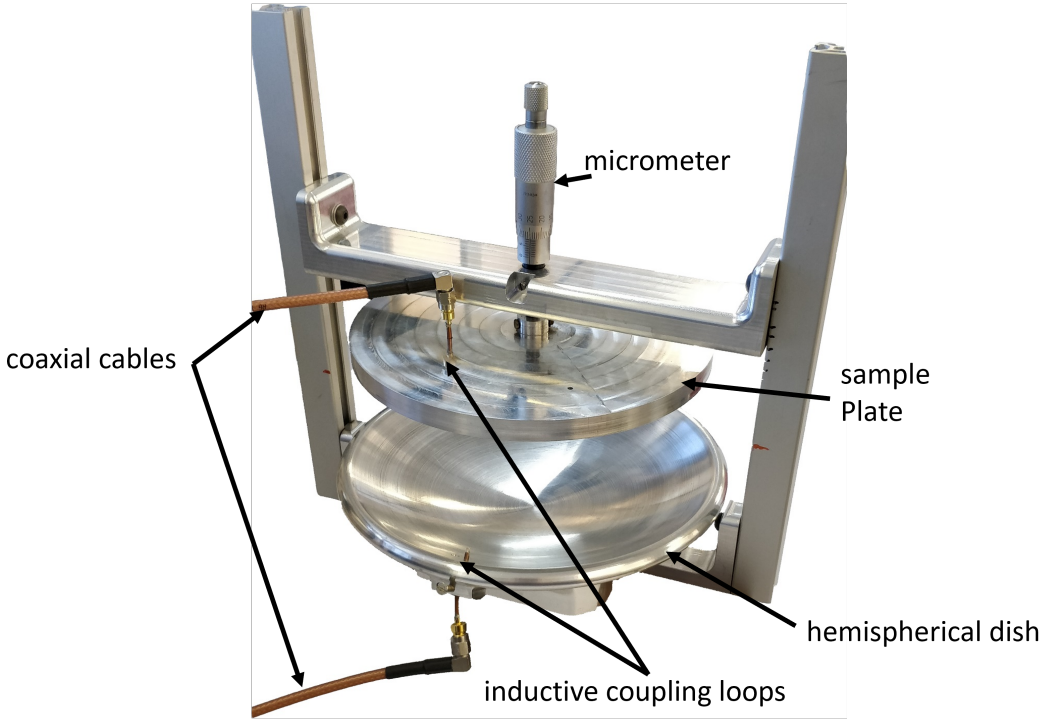

Figure 3.9: location of new coupling locations of the FPOR, one in the HSD and one in the sample plate.

Even with this change in port location, due the direct coupling of the ports, the resonance could not be tracked when using the Keysight N5232A PNA as the tracking software implemented for the PNA would jump to other S_{21} peaks caused by the [presence] of this high baseline response.

3.3.6 Future Work

For the FPOR there are many problems that need to be resolved, but automating the separation between the sample and the HSD should be one of the first things done, as it would alleviate problems that may be due to the use of a micrometer; automating this with a linear stage would mean that it is then more controlled and can be used to target frequencies more accuracy and also more repeatably. With automation of setting the resonant frequency, more attention can be paid to investigating the coupling port locations/structures used when coupling. The reason for investigating a different solution to measure PBF samples was due to the issue of coupling in this structure; It was difficult to do any measurements of R_s due to the nature of the strong coupling of the FPOR and the inconsistent measurement of Q.

3.4 Coaxial Resonator: Overview

With a coaxial resonator (CR) the objective is to make measurement via replacement of the centre conductor, as with a coaxial structure the magnetic field is concentrated around this part; hence replacing this with a PBF part would enable measurements of the performance of the inner conductor's surface. As coaxial cables have their currents confined to the outermost region of the conductors as a result of the skin effect, this would also mean that the outermost layers would be under test, resulting

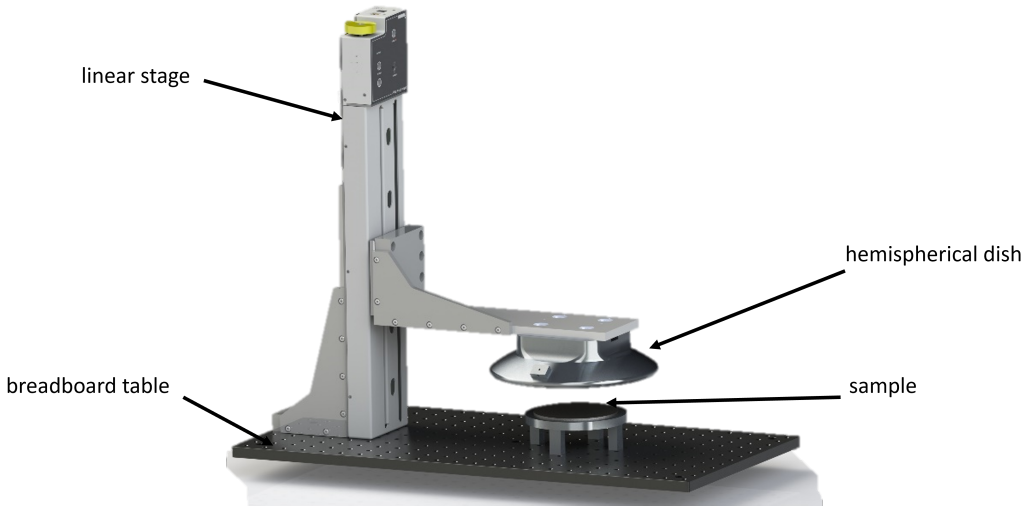

Figure 3.10: Conceptualised designs for an FPOR with an incorporated automated linear stage.

in analysis which could evaluate if post-processing reduces the surface resistance of PBF part.

3.4.1 Measurement Theory

Like all the resonant structures within this thesis, the CR is capable of having multiple resonances allowing for measurements of PBF parts to be measured across a wide range of frequencies. Where the CR has an open circuit at each end, giving rise to a half-wavelength TEM resonances, the resonant frequency as defined in Equation 3.25 is determined by the length of the centre conductor,

$$f_0 = \frac{nc}{2L} \tag{3.25}$$

where n is is the integer number of the half wavelengths on the length, c is the speed of light, and L is the length of inner conductor. Due to this, the resonant

frequencies are integers of the fundamental, so in this case a length of 53.5mm was chosen, which resulted in a resonant mode of 2.8GHz and subsequent harmonic modes would be at 5.6GHz and 8.4GHz. One advantage of the CR over the FPOR is that there are no moving mechanical parts to achieve a different frequency and so this could overcome some of the problems associated with the FPOR. Equation 3.25 was verified with a COMSOL simulation, as shown in Fig 3.13 - 3.15

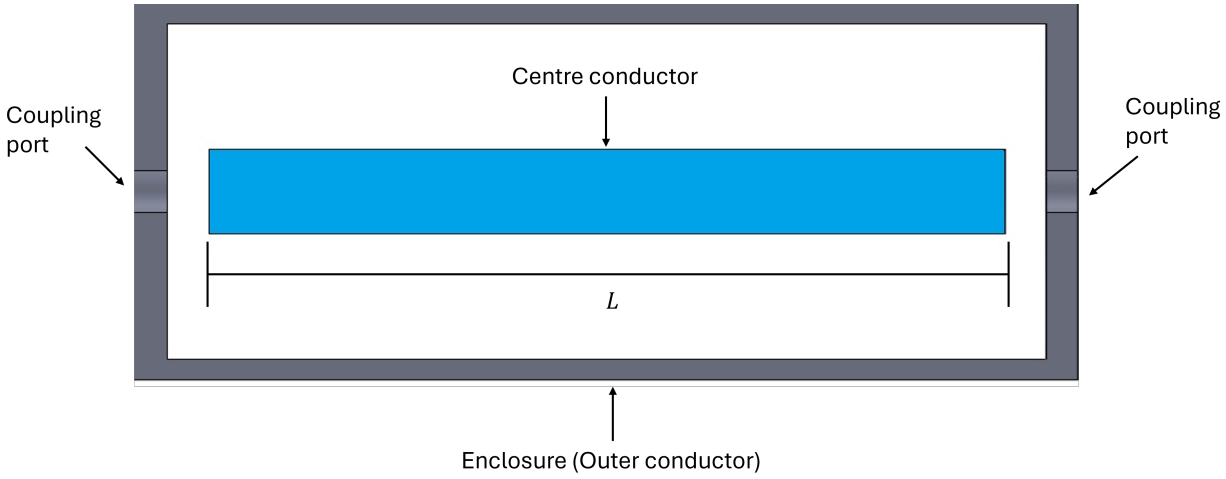

Figure 3.11: Cross section of a basic air spaced CR

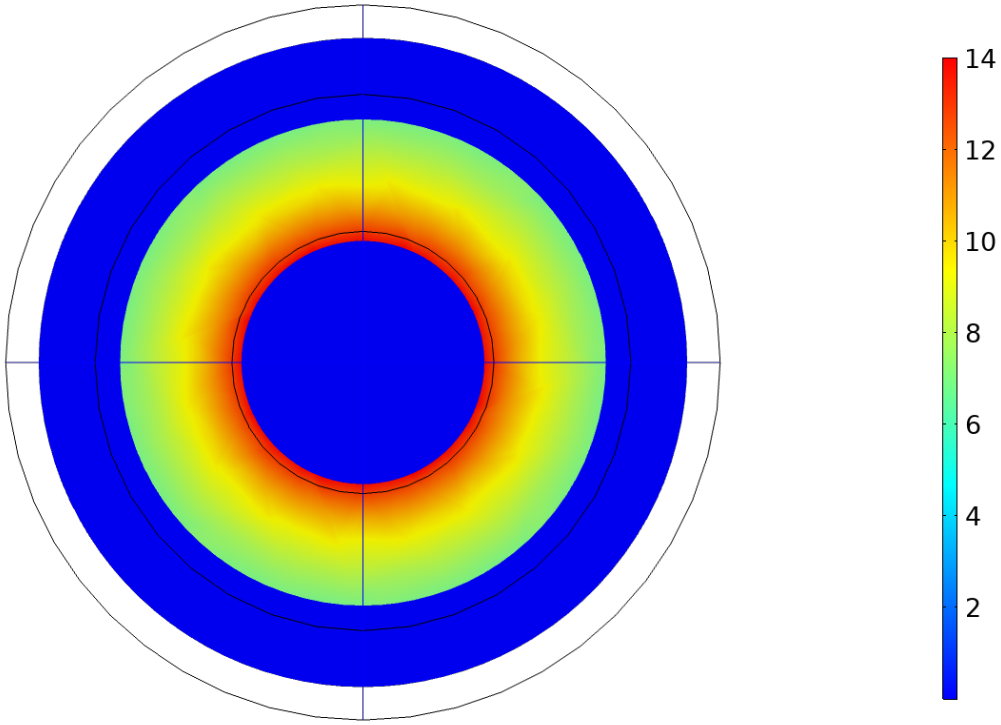

Figure 3.12: Cross section of a CR magnetic field (A/m), COMSOL Simulation resonating at 2.8GHz.

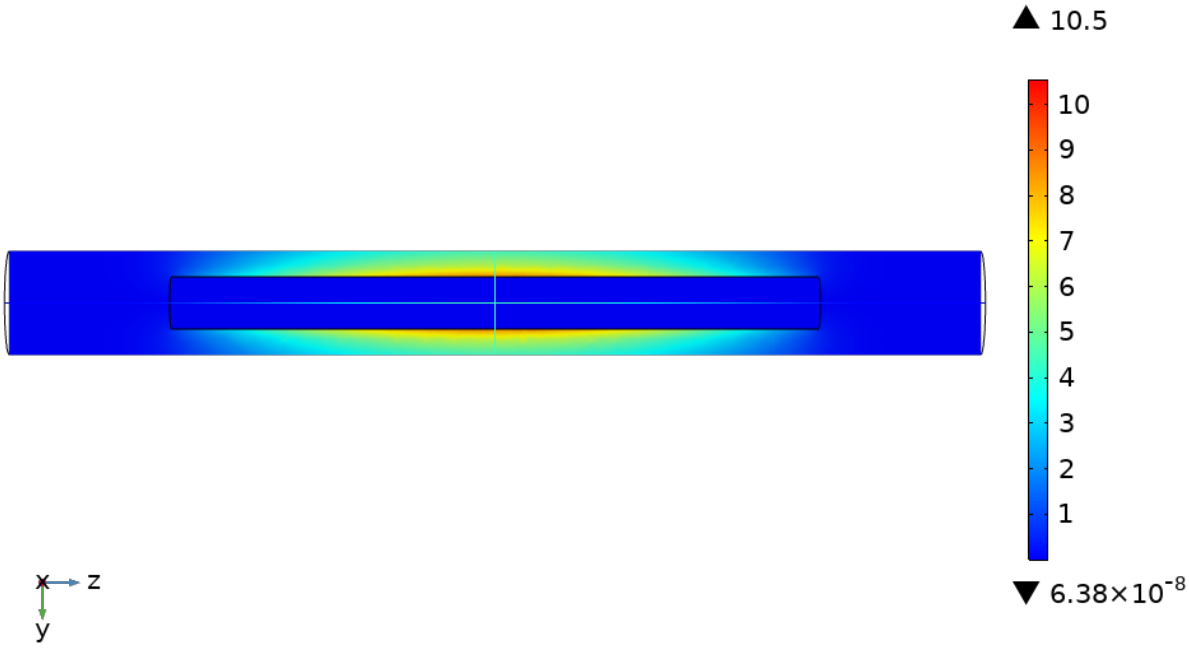

Figure 3.13: Magnetic field (A/m) COMSOL Simulation of CR at 2.8GHz.

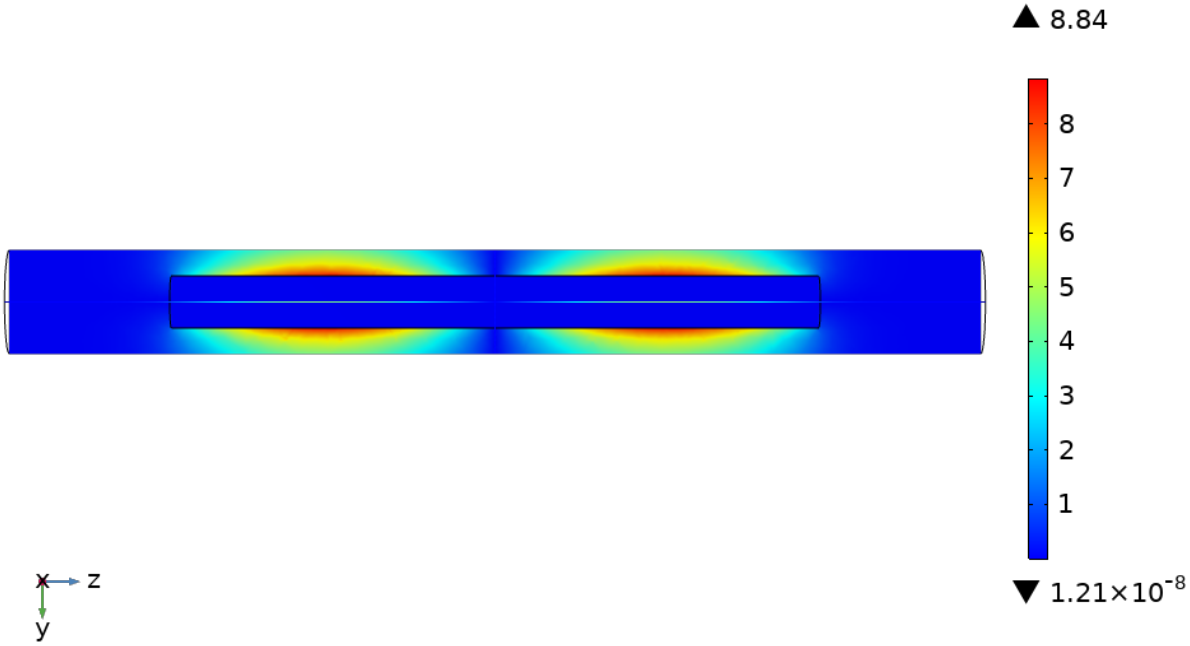

Figure 3.14: Magnetic field (A/m) COMSOL Simulation of CR at 5.6GHz.

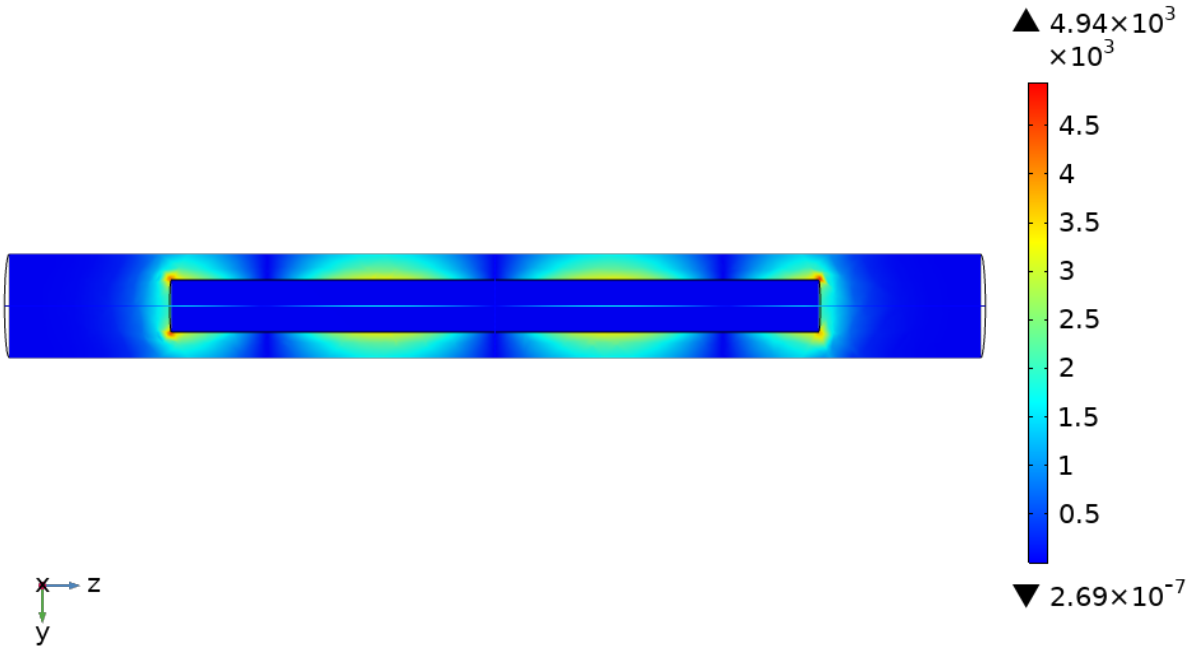

Figure 3.15: Magnetic field (A/m) COMSOL Simulation of CR at 8.5GHz.

3.4.2 Resonator Design

As can be seen in the figures above, the inner conductor of the CR has a higher current density in contrast to the outer conductor, which was one of the reasons for the choice to replace the centre conductor. An air-spaced CR was proposed, as replacing the centre conductor would be impossible if it was enclosed in a dielectric material. However, considering the nature of an air-spaced coax, supports are still needed to support the centre conductor in the centre of the line. Therefore, when calculating losses of this structure, each loss can be attributed for a CR shown in Equation 3.26.

$$\frac{1}{Q_0} = G_u R_{S_u} + G_x R_{S_x} + \sum_{p=1}^{i} P_{ed_P} tan\delta \quad (3.26)$$

Where G_u and R_{S_u}, G_x and R_{S_x} are the geometric losses and surface resistance associated with the enclosure walls, which are considered the outer conductor for CR and the inner conductor, respectively, while p_{ED} is the dielectric filling fraction for the dielectric volumes present within the structure, which are the PTFE spacers. These geometric factors and dielectric filling fractions are defined in Equations 3.19 and 3.20. As the CR is to be used over multiple resonances, each resonance will need to be recalculated with COMSOL for both their new geometric losses and geometric filling fractions, as these will alter with the resonant frequency due to the presence of the dielectric spacers and the change of electric field along the central conductor.

3.4.3 Spacer Design

With an air-spaced CR, spacers are needed to ensure the location of the centre conductor is along the axis, other wise if the centre conductor wasn't centred would result in a bunching of magnetic field to accumulate on the inner conductor and not be distributed evenly. To reduce the losses associated with these spacers, a practical test was done to compare the effects of spacers of two designs, where one is a solid spacer and the other in a half spacer with voids to further reduce the amount of dielectric present with the structure. These designs can be seen in Fig 3.16 and the results of simulations with these parts included can be seen in Fig 3.17

Figure 3.16: PTFE spacer design a) is a solid design, and b) is a half spacer with voids in the structure, reducing dielectric loss.

As can be seen in Figure 3.17, there are large reductions in the Q factor in 2 regions (6.5GHz and 17GHz), which is due to the full spacer being located within the propagating electric field at certain resonant modes. However, when using the half spacer, it can be observed that there is no large reduction in the Q factor, which indicates that lower volume of dielectric material present near the centre conductor reduces the dielectric losses associated with the dielectric filling effect. The larger

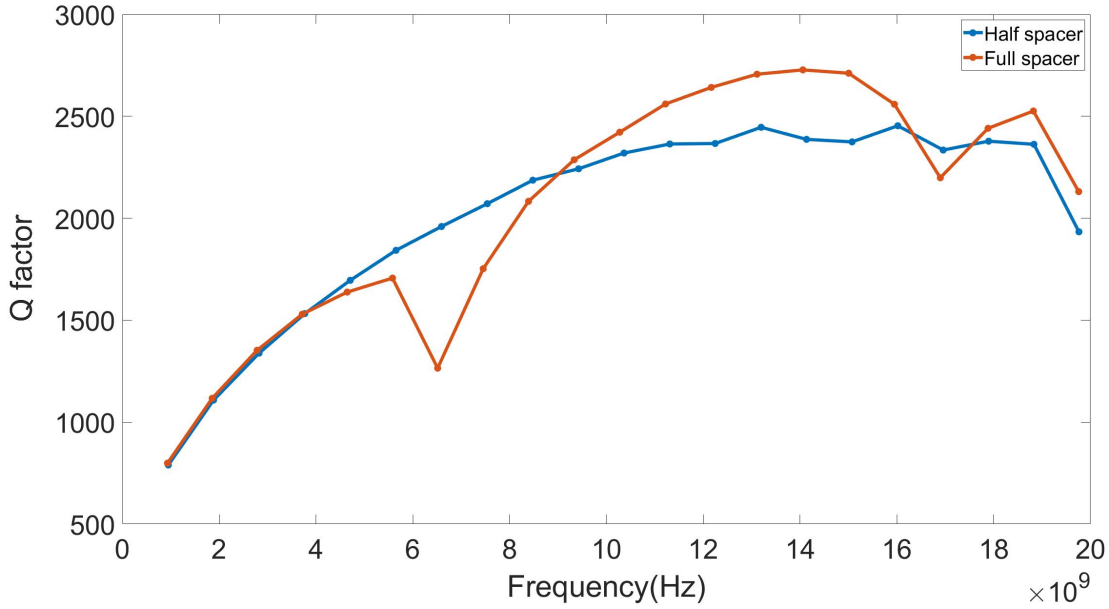

Figure 3.17: Q factor measurements of full spacer and half spacer from 1GHz to 19.8 GHz.

reduction of the Q factor at 19.8GHz is due to a combination of the connector savers used on Keysight Technologies Vector Network Analyser (VNA) (PNA-L N5232A) as they are only rated to go up to 18GHz, so the coaxial cable used and connectors both need to be operating within their limits.

3.4.4 Sample Design

There are issues with PBF for manufacturing samples with a diameter down to 2mm since such a part would have a flat spot where it has adhered to the build plate if built horizontally, meaning that the centre conductor would have a modified field distribution when compared to a cylindrical part; which would result in some of the parts potentially having more loss than others due to the bunching of currents along the length of the conductor. Also, this would mean that the spacers designed would need to be changed to accommodate a variation of flat spots which may be present on some samples, as these may come in different widths if they were built vertically.

Also, warping of the part would cause a major issue and as such small diameter parts would be more prone to warping during the PBF process.

Another issue associated with the fabrication of small cylindrical parts is the repeatability of post-processing, with processes such as machining and media tumbling, being be difficult. For this reason a rectangular part was proposed, as machining a flat surface is easier and more repeatable as samples can be made horizontally, as it already has flat surfaces which can be used for adhesion to the build plate. To analyse the effect of replacing a cylindrical conductor with a rectangular structure, a COMSOL simulation was again used. In this simulation, the dimensions of the rectangular central conductor were 3.5mm by 2mm by 57.6mm as it has the same surface area as the cylindrical conductor which gives a fundamental resonance of 2.6GHz, which can be seen in figure 3.18 below. The cylindrical centre conductor (as a comparison) had a diameter of 2mm and a length of 57.6 to ensure that both sets of resonant frequencies were the same.

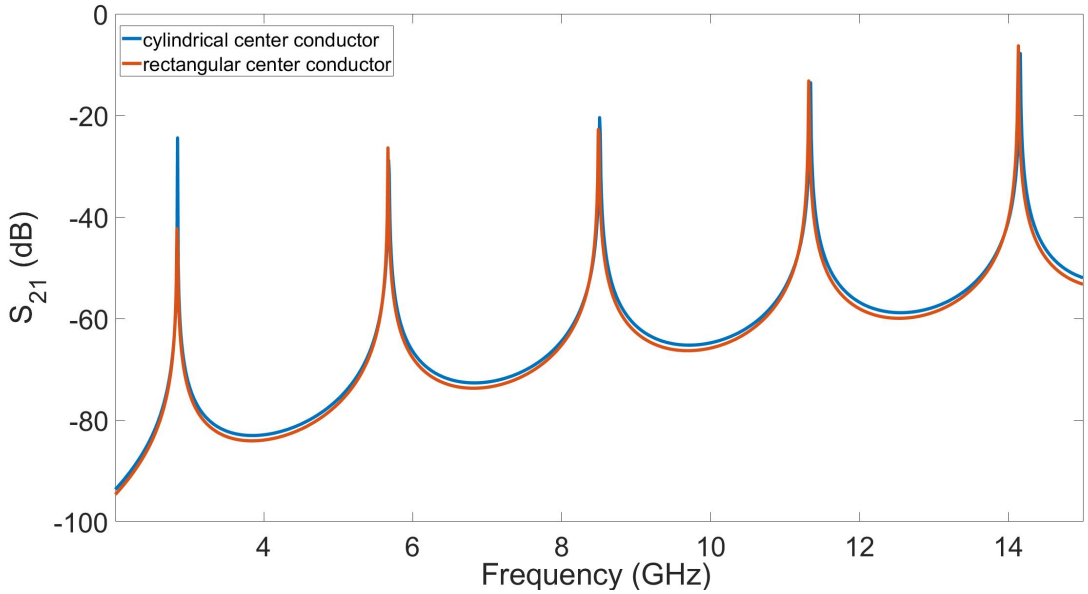

Figure 3.18: COMSOL simulation of S_{21} comparing a rectangular and cylindrical centre conductor.

The S_{21} response when using the rectangular centre conductor shows the same

computational response as the cylindrical centre conductor, making it a suitable replacement. However, when studying the currents along the surface of the rectangular part, there is a large bunching of currents around the corners of the rectangular part, shown in Figure 3.19. This is because the edges have the highest electric field. Due to the increased bunching of currents along edges and with an increased current density, a study to look at the width of the part was performed to investigate the magnetic field applied to the surface of the rectangular central conductor.

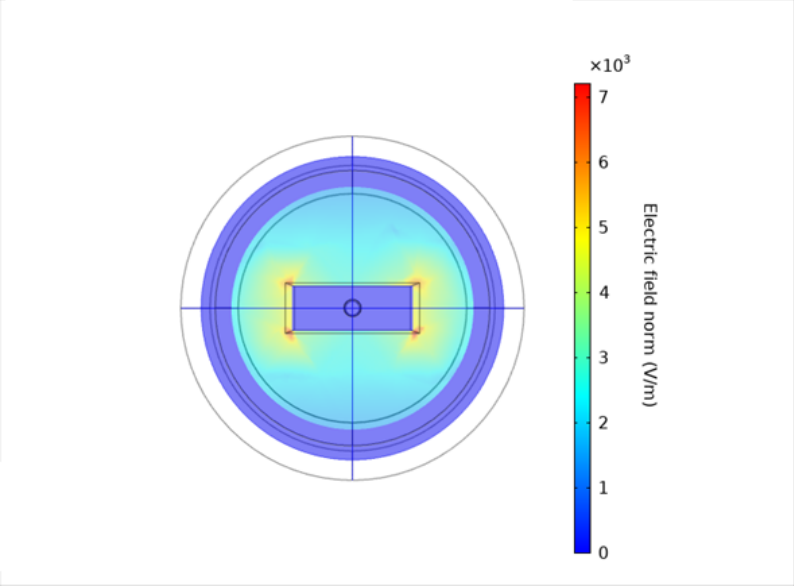

Figure 3.19: Simulated electric field at 8.5GHz of rectangular center conductor.

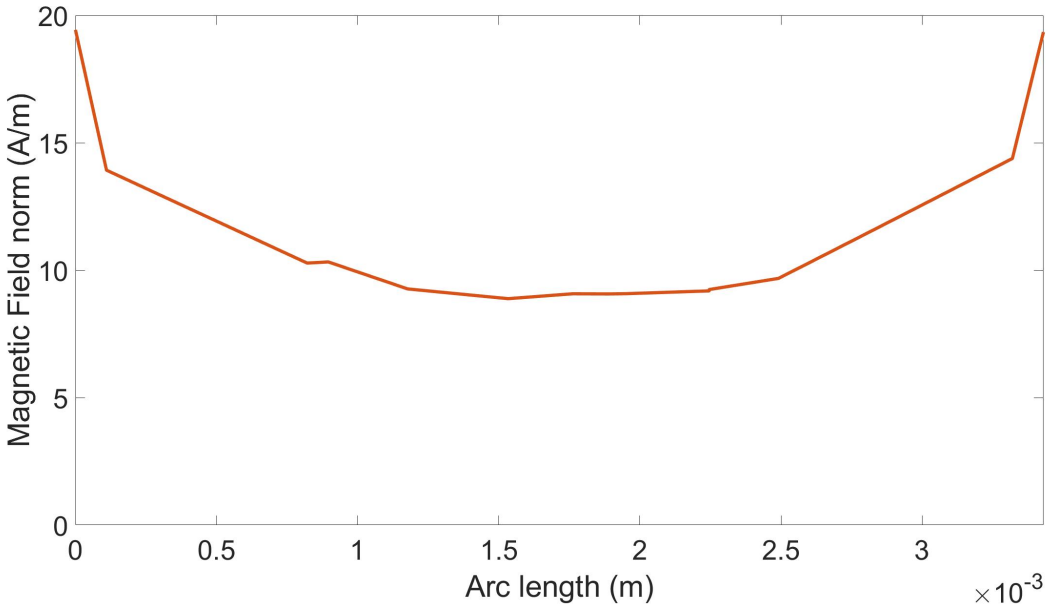

Figure 3.20: Magnetic field (A/m) across the surface width of the center conductor sample.

Although the R_s values extracted from the rectangular samples will be weighted by the edges, it would still represent a meaningful average across the full length of the sample owing to the current density present across the centre of the sample.

3.4.5 Measurements

The a practical measurement was performed on a Keysight Technologies Vector Network Analyser (PNA-L N5232A) to determine the differences between rectangular and cylindrical centre conductors, shown as in Fig 3.21, there was a large disparity between the measured Q factors using the PNA after taking out losses associated with the cables used to connect the CR to the PNA. As these are both fabricated out of the same copper, the material should have the same fundamental R_s values, so these differences are due to shape of the central conductor and thus show the effects of the bunching of currents along the rectangular centre conductor. So the original concern about the bunching of current was valid and so a new method which uses the principles of a CR but overcomes these issues was proposed which is the broadband parallel plate resonator BBPPR

3.5 BroadBand Parallel Plate Resonator: Overview

For both resonant structures shown earlier in Sections 3.3 and 3.4, the goal of measuring PBF samples over a broad range of frequencies has been at the forefront; however, many issues with these techniques made it difficult to gather results. e.g. issues with the coupling and the frequency span of a single measurement with the FPOR resulted in measurements to be non-optimal. This was also the case with the CR, as due to having the centre conductor as the material under test, repeata-

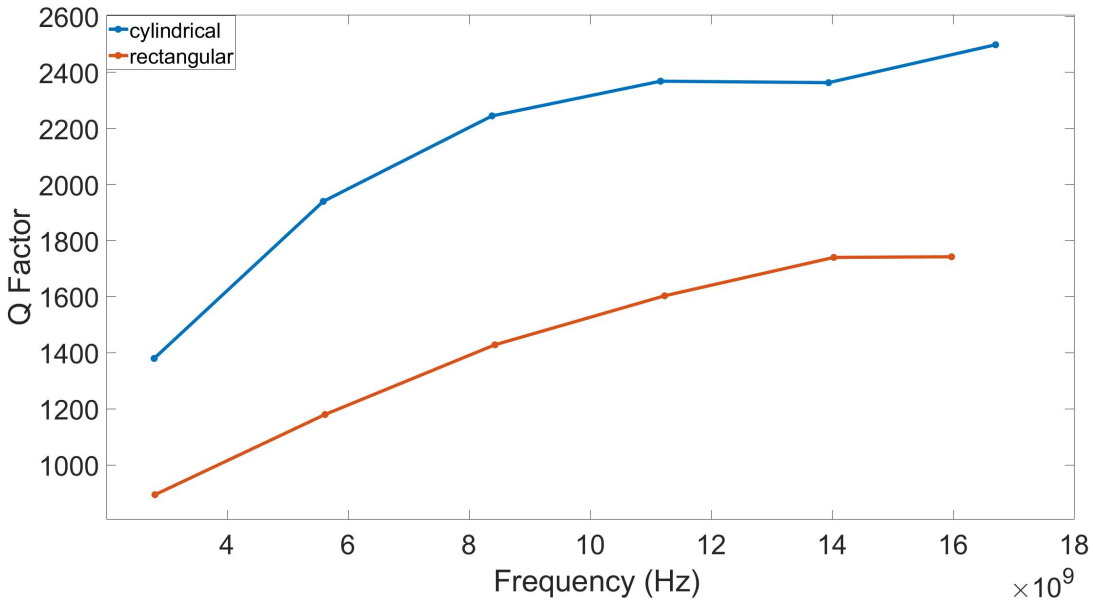

Figure 3.21: Measured Q factor response of a rectangular and cylindrical coaxial resonator.

bility was a major issue, as replacing the inner conductor not only changed the coupling but also damaged the spacer over many uses due to being friction fitted and would cause the spacer to be fatigued and then break. This meant that new spacers needed to be used each time, which again affected the repeatability of the test. So, the broadband parallel plate resonator (BBPPR), was developed to overcome the issues with previously used techniques. One of these advantages is that the induced currents along the surface are unidirectional; this means that measurements can be made to also see the effects of build orientation, by rotating the samples by up to 90° in the test fixture.

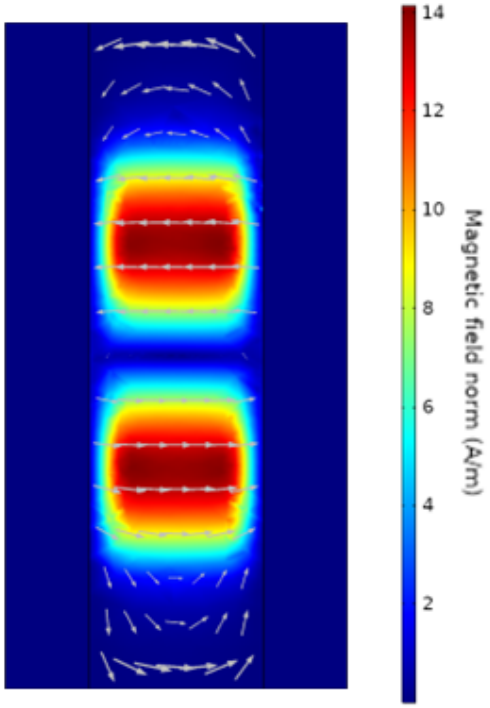

Figure 3.22: Magnetic field applied to sample surface (view from above), showing the directionality of the current measuring the anisotropy of R_s based on build orientation.

3.5.1 Measurement Theory

The BBPPR is an evolution of a CR where the resonant frequency is defined by the length of the centre conductor. This role is also shared with the reference plate but is offset toward the lower section, which will be replaced to interchange the sample under test. This resolves the issues previously met with the CR, as the samples to be tested are large enough so that they can be used to enclose the end plate and that they are flat. Furthermore, as long as these conditions are met, the sample could be fixed without fixture holes, though a small amount of clamping force is required to ensure the required electrical contact is made.

3.5.2 Resonator Design

To suspend the reference plate, two PTFE spacers are used to ensure that the reference plate is secured in a fixed location, as unlike the CR it doesn't need to be removed. These spacers were keyed so that they would also be fixed in a position to avoid any issues of alignment that would result in twisting on the reference plate, which may have affected the applied magnetic field to the material under test. These are secured with nylon screws so that if the fixture was moved they would still be in position, unlike the CR which had the spacers friction-fitted. With the reference plate in a fixed position, coupling to the structure was simplified as there is no effective change to the structure when measuring from sample to sample, as we couple to the reference plate. These features can be seen in Fig 3.23

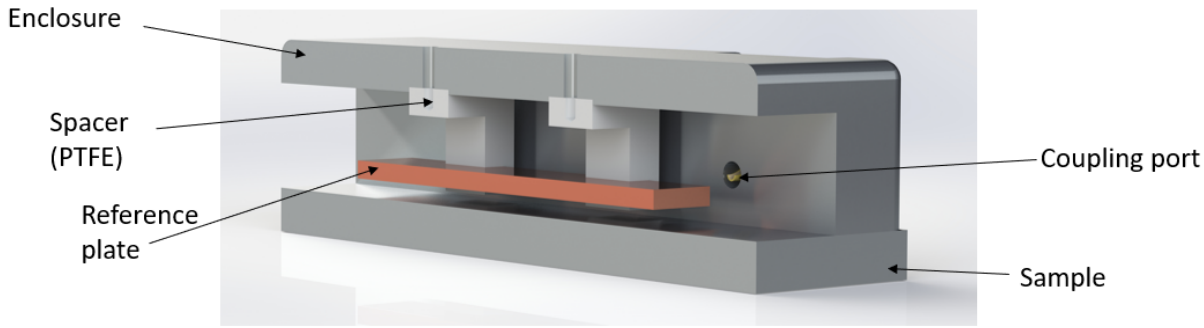

Figure 3.23: Cross-section of BBPP showing the construction of the resonator .

3.5.2.1 Enclosure Design

After manufacturing the BBPPR and performing initial testing there were more resonances than anticipated, in the range of up to 20GHz. After some investigation into the dimensional properties of the BBPPR it was found that the enclosure itself became a waveguide, resulting in the higher frequency modes. These modes can be seen from 6-8 GHz and 12-14 GHz in Fig 3.24. However, at approximately 10 GHz there is another mode which is outside that of the the expected resonant modes and waveguide frequencies. This is a mode across the width of the reference plate, but unfortunately its Q factor was too low to be used as a means of using the surface currents which are perpendicular to the intended ones to measure anisotropy in the sample.

To resolve this issue, a redesign for the enclosure and the reference plate was done to make these other modes less dominant and remove them completely; this was done by making the enclosure to have a semi cylindrical open cross section, increasing the cut-off frequency of undesirable modes as it wouldn't allow a standing wave to be supported. Other modifications were needed, as changing the enclosure meant changing the reference plate. Making the width 15mm meant that the resonant

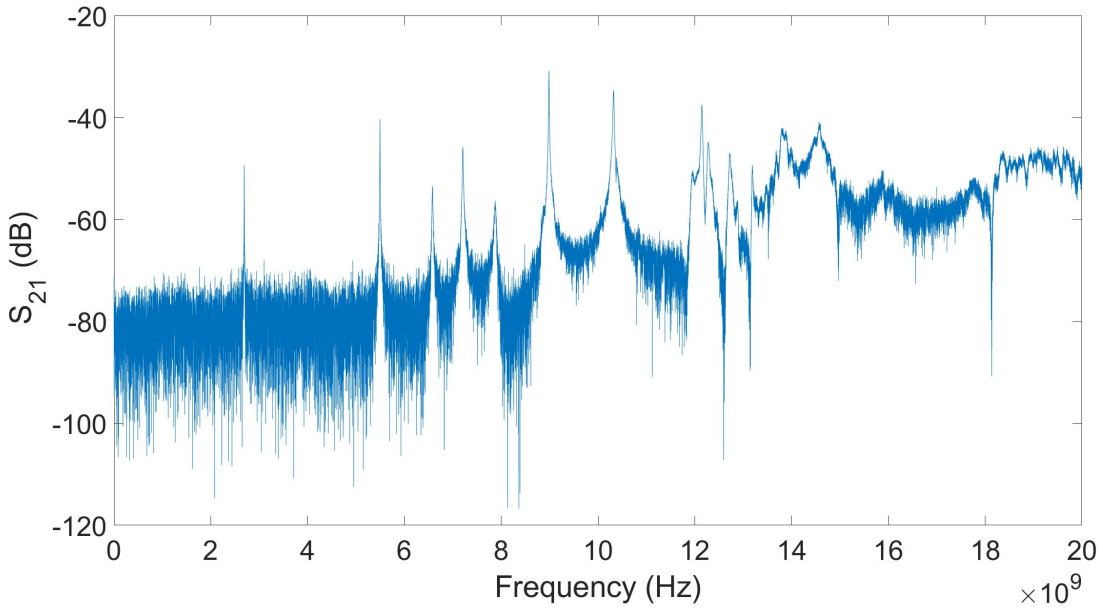

Figure 3.24: Measurement of S_{21} for the first BBPP over 0-20GHz.

modes would be at least 20 GHz as 15mm is the wavelength of 20GHz, which is outside of the measurement range when using the Keysight Technologies VNA (PNA-L N5232A); this can be seen in the simulated S_{21} response of the new design in Fig 3.25.

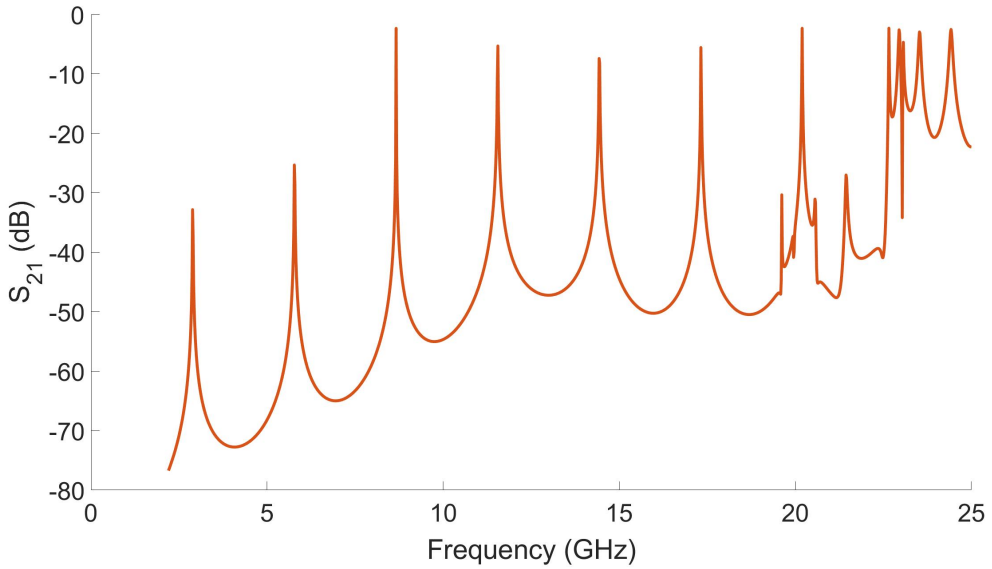

Figure 3.25: Simulated S_{21} response of new BBPPR enclosure over 0-25GHz.

3.5.2.2 Reference Plate Design

One other design change to the reference plate was that the top side of the plate had beveled corners. this was to distribute the current across these corners, since coupling to this structure had to be done at an angle in relation to the reference plate, as the height of the reference plate from the sample made it difficult to get a coax panel connector in place for the coupling structure. The bunching of currents when using a rectangular reference plate causes too strong a coupling to the structure, so to distribute the current better at these corners and to lessen the coupling strength, beveled corners were used. This meant that a straight coupling capacitive feed could be used, which also made it easier to couple to. These changes can be seen in Fig 3.27.

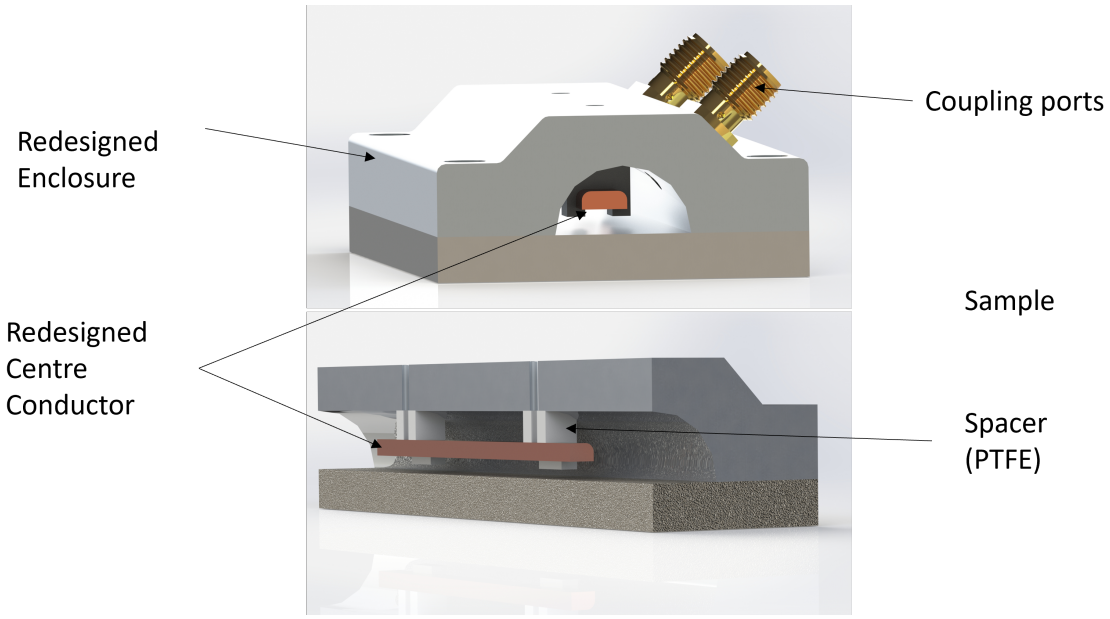

Figure 3.26: CAD cross section of version 2 of BBPPR .

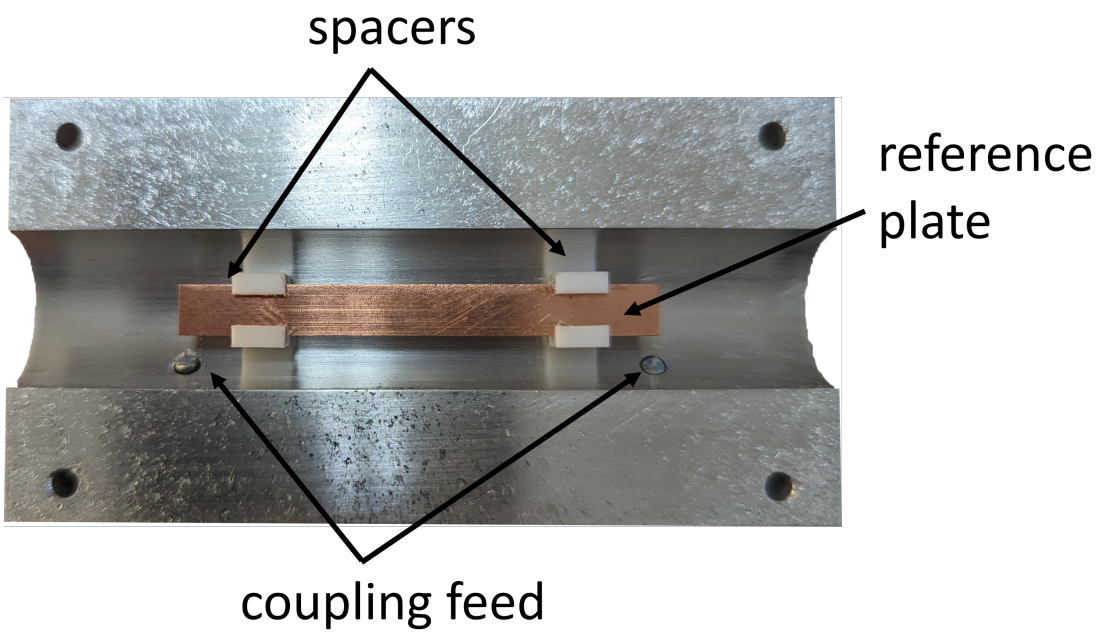

Figure 3.27: Photograph of the underside of BBPPR showing capacitive coupling feed to the reference plate.

3.5.3 Calibration

For calibration of the BBPPR it was necessary to attribute all the losses associated with the structure so that an accurate measurement of Q_0 (and hence R_s) could be taken. To achieve this, characterisation measurements were also done of the cables used for the experiment to ensure that cable losses can be accounted for. These measurements were taken over a range of 2.6-8.6 GHz as the BBPPR is intended to be used over this range of frequencies. The losses attributed to the structure can also be calculated via simulation, which is accomplished with the use of COMSOL by singling out each lossy components by attributing them to their associated lossy material and making all the other components lossless, so that we can calculate each loss associated with each component. Similarly to the CR, the loss contribution can be summed to find an overall Q_0 as in Equation 3.27

$$\frac{1}{Q_0} = G_s R_{s_s} + \sum_{m=1}^{j} G_{W_m} R_{sw_m} + \sum_{p=1}^{i} P_{ed_P} \tan\delta \quad (3.27)$$

where Q_0 is the total unloaded Q factor of the resonant structure, G_s and R_s G_W and R_{sw} are the geometric factors and surface resistance values associated with the sample; the summation of j is the summation of the losses associated with the walls of the resonator and i is the dielectric volume filled within the fixture (in this case being PTFE for the spacers and Nylon_{66} for the screws). These geometric and dielectric filling factors are defined in Equations 3.19 and 3.20. Loss tangent $\tan\,\delta$ is found through cavity perturbation, so the only loss not known is R_{s_s} from equation 3.27, which is what we need for the sample. Correcting for small changes to the frequency between the measurements of samples is done by assuming $R_s \propto \sqrt{f}$ and $\tan\delta \propto f$, the later being consistent with the assumption that $Q_d f$ is constant, as is usually assumed.

A reference sample is used here with a known value of R_s. We use the copper of a Rogers Corp. RT/duriod 6002 sample PCB of a known R_s value measured with a dielectric resonator fixture that was discussed is Section 2 and published in [53],[55]. With this measurement of R_s being provided for the sample of PCB being used, we can use this as a "golden standard" measurement value.

To first understand the accuracy of the BBPPR, measurements of the PCB sample were made with the structure being dissembled and reassembled to ensure that any variation in measurements between each measurement can be analysed. For the disassembly procedure, a total dismantling of the sample from the BBPPR was done to ensure that any variation in mounting can be assessed. For reassembly, it was ensured that the screws were tightened up to a torque of 2Nm so that no over tightening occurred, which could warp either the PCB and other samples when

testing, so minimising any changes to the samples.

As shown in Fig 3.28 over the range of frequencies measured, the standard error from each measurement is at approximately 0.06%, 0.12% and 0.13% for each mode respectively, which was obtained by repeating the reassembly process 10 times. This signifies that for subsequent tests the error bars show the variance between samples produced by PBF rather than the error between each measurement that occurred due to inaccuracies in the measurement technique. We could also establish a standard error with are sample of measurements of samples N=10. From the standard deviation σ, the standard error becomes $\sigma/\sqrt{10}$.

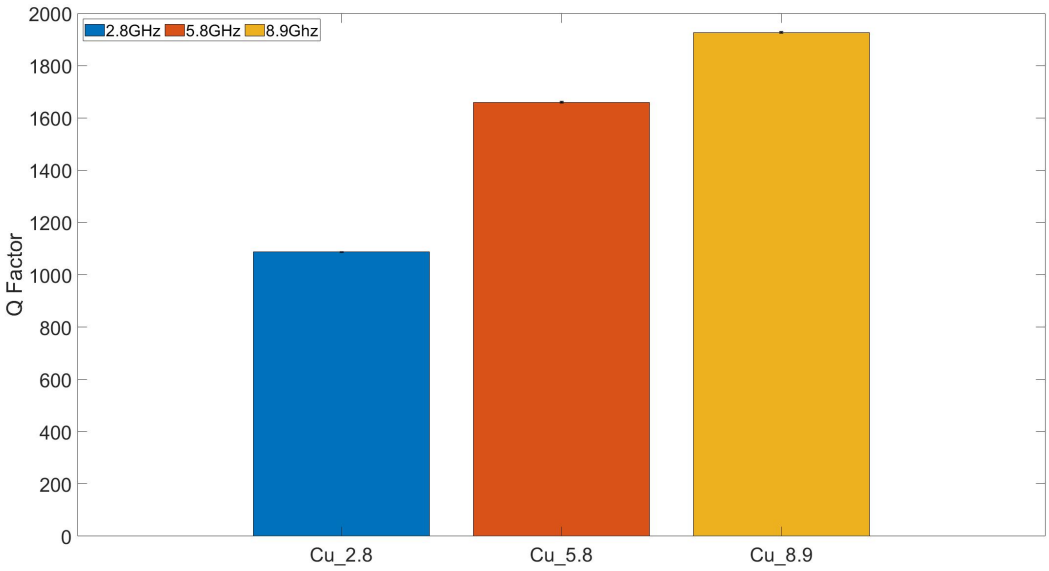

Figure 3.28: Q factor measurements taken of Copper PCB sample .

3.5.4 Correction Factor for R_s

As stated in [122], sharp corners of rectangular conductors need a correction factor to account for the current crowding. This correction factor can be obtained with the aid of COMSOL, since the simulated solution can be used in conjunction with

known samples of known R_s to calculate a correction factor. The contribution to the total loss of the cavity wall is low (around 4%) and it can be combined with the reference plate to produce an average value of R_{Swcal} for the reference copper plate. This value is not changed when replacement of samples is performed and can be defined as

$$R_{Swcal} = \frac{\frac{1}{Q-0} - G_{Cb}R_{S_{Cb}} - \sum_{p=1}^{N} P_{ed_P} tan\delta_p}{G_{Sw}} \tag{3.28}$$

where $R_{S_{Cb}}$ and G_{CB}, and R_{SWcal} and G_{Sw} are the surface resistance and geometrical factors for the known Rogers Corp copper PCB sample and the remaining conductive surfaces within the resonator, respectively. Using the Q factor measurements shown in Fig 3.28 and measuring the PCB sample with the known 'gold standard' we can produce a correction factor. However, due to the nature of BBPPR we measure over a wide range of frequencies and so having an absolute value would not work; hence we need to scale the 'golden standard' measurement with frequency to effectively scale the found measured R_s value for each resonance, as shown in Equation 3.29

$$R_{sfs} = \sqrt{\frac{\pi f_r \mu_0}{\sigma_s}} \tag{3.29}$$

where R_{sfs} is the surface resistance of the sample plate at a given frequency, σ_s is the conductivity of the measured sample and f_r is the resonance frequency. So as the measurement was taken at 7.5 GHz and had a measured surface resistance of 33.4mΩ, by using equation 3.29 the new resistances are 20.5mΩ for 2.84 GHz, 29.6mΩ for 5.92GHz and 36.3m$\Omega$for 8.92GHz; by using these values we can calculate the effective correction factor for each value using Equation 3.30.

$$k = \frac{R_{Swcal}}{R_{sfs}} \tag{3.30}$$

Hence, we have correction factors of 1.18, 1.08 and 0.82 of frequencies for 2.84GHz, 5.92GHz, and 8.92GHz, respectively. We can then rearrange equation 3.27 and substitute to calculate the surface resistance of the sample.

$$R_{S_s} = \frac{\frac{1}{Q_0} - \sum_{m=1}^{j} G_{W_m} k R_{Swcal} - \sum_{p=1}^{i} P_{ed_P} tan\delta}{G_s} \tag{3.31}$$

3.6 Further Work

For the BBPPR there are some areas of interest which could be pursued to improve the performance and versatility of the BBPPR so that it can investigate higher bands within the frequency spectrum. One key element which would need to be addressed would be the resonances caused by the enclosure of the BBPPR. As this is the apparent limiting factor so far which could hinder the measurement of higher frequencies, a solution to this could be to design the enclosure to be a filter which would stop the rise to any unwanted resonances, leaving the spectrum of choice to be measured.

Chapter 4

Build Orientation and Measurement Orientation

4.1 Introduction

In this chapter, an investigation is made into how the effect of build orientation affects the surface resistance as the PBF components are built by using multiple layers of melted metal powder. Also due to the characteristic of the measurement technique, the magnetic field is applied in a single direction, allowing us to evaluate the R_S of the surface at different orientations. All of this data could then be used to aid in improving the performance of PBF components by simply changing the orientation of PBF components when being manufactured.

4.2 Sample Preparation

To evaluate R_S of PBF components, consideration has to be made as to what would typically be printed and how it would be used. As in most instances, AM builds for mass production are done so that the yields per print is highest and so little consideration is given to the build orientation. So, as the BBPPR uses an end plate replacement method for the material under test, having a sample of N=3 allows a standard deviation of σ to be estimated, and hence a standard error of $\sigma/\sqrt{3}$ when quoting the averages values of results. These three different samples are made with varying degrees of angular elevation with respect to the build plate, these angles being 0 degrees, 45 degrees and 90 degrees, as shown in Fig 4.1.

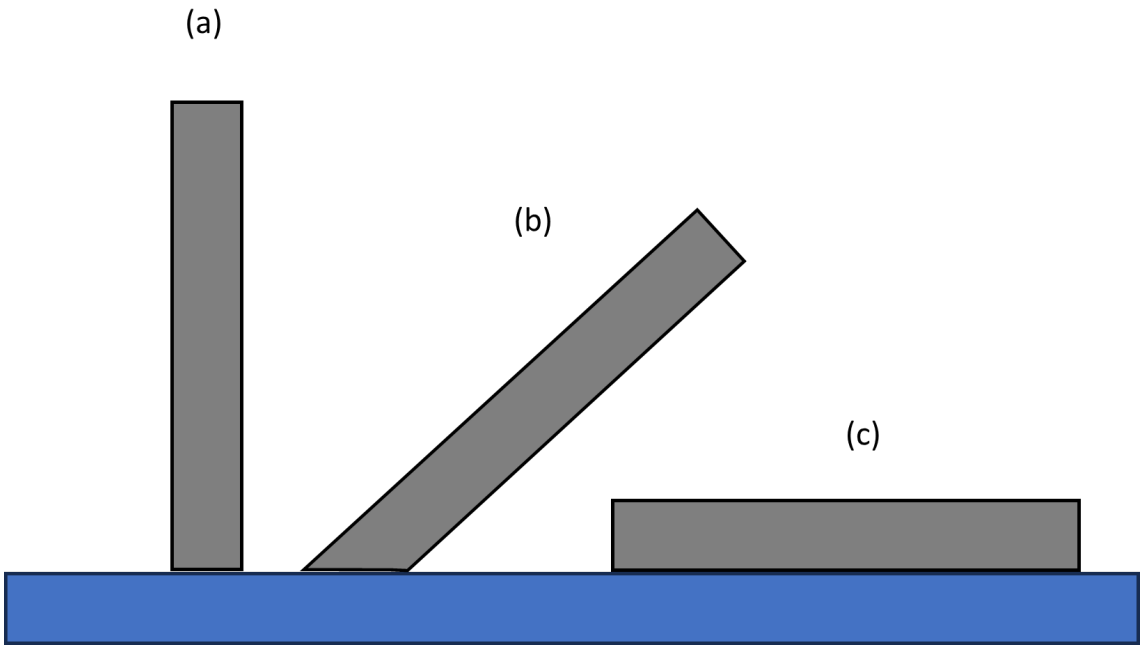

Figure 4.1: Build orientation of samples with reference to build plate where (a) is at 90 degrees (b) is at 45 degrees and (c) is at 0 degrees.

These angles were chosen as they represent all potential outcomes of the build orientation. An important note is that the 45 degree sample actually has two surfaces to measure as we have the topside (which would be facing towards the laser), and the underside facing towards the build plate; all of the surfaces are measured. The

sample material chosen for the PBF parts was AlSi10Mg, as AlSi10Mg is one of the most widely used alloy powders for microwave components as it is lightweight, has good mechanical properties and a high electrical conductivity (so resulting in a low R_s and high Q).

4.3 Sample Surface Measurements Technique

We can apply a magnetic field in different directions to investigate the inherent surface geometry of the PBF process that affects the R_S, shown in Fig 4.2

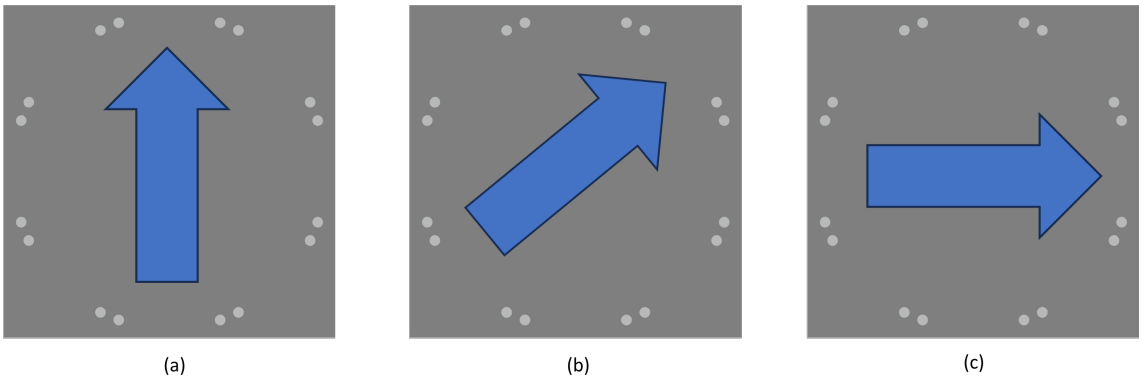

Figure 4.2: Directions of applied magnetic field to the samples where (a) is vertical (b) is at 45 degrees and (c) is horizontal. Sample hole positions for the BBPPR text fixture are also shown

4.4 Build Orientation and Surface Orientation Measurements

By applying a magnetic field to induce a current on the surface of the PBF parts, the influence of the R_s can be investigated. For every sample type, there were 12 individually made samples, to produce a comprehensive data set for each build orientation, where each measurement consisted of using all three resonant modes

and three orientations of the applied magnetic field; these results are shown in Fig 4.3 and 4.4

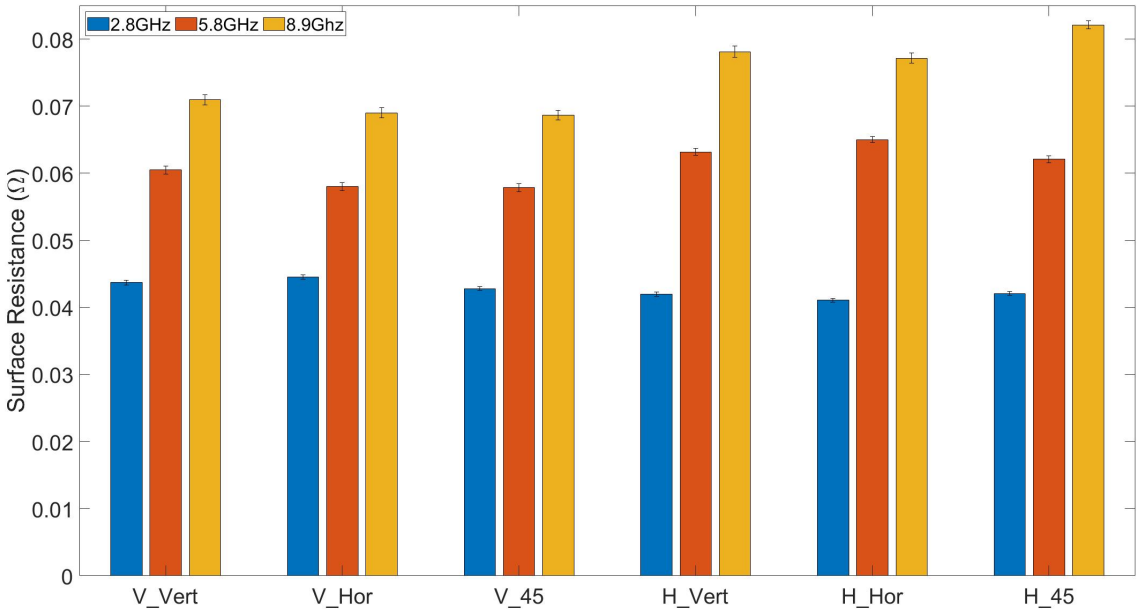

Figure 4.3: R_s measurements of AlSi10Mg as built with a build orientation of Horizontal, Vertical samples.Standard errors are shown by the error bars.

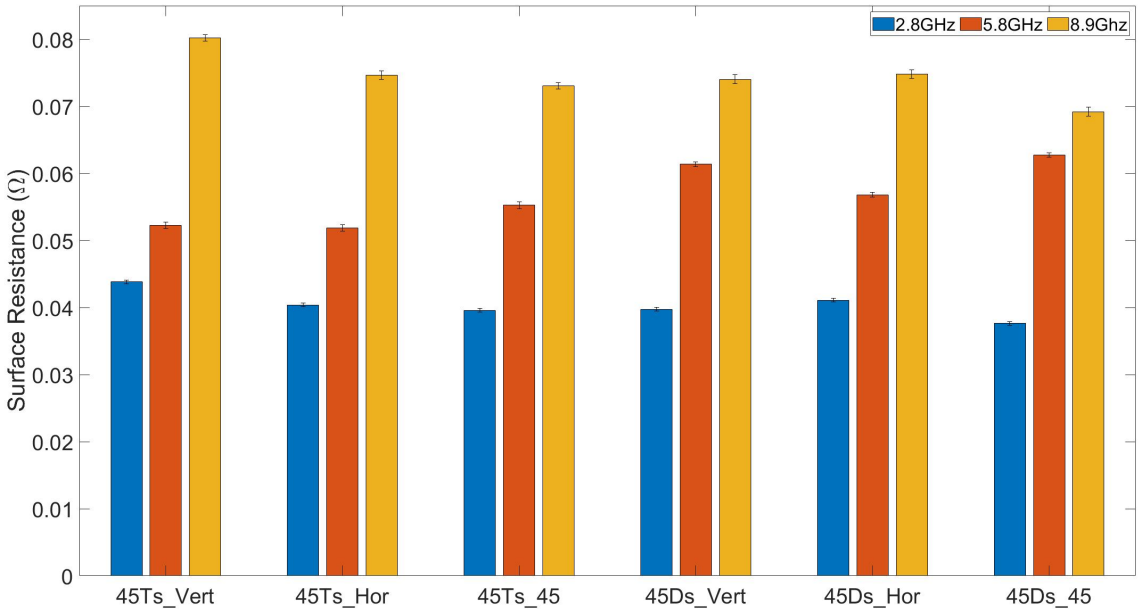

Figure 4.4: R_s measurements of AlSi10Mg with as Build surface for topside(Ts) and downside(Ds). Standard errors are shown by the error bars.

Table 4.1: Measurement Sample Description Modifiers for as-built PBF samples

Sample ID	Measurement Modifier
V_	Vertically built sample
H_	Horizontally built sample
45Ts_	45 degree built sample and topside surface
45Ds_	45 degree built and sample downside surface
vert	magnetic field applied vertically on the sample
hor	magnetic field applied horizontally on the sample
45	magnetic field applied 45 degrees on the sample

Table 4.2: R_s measurements for As-built PBF samples at 2.8GHz

Build Orientation	R_s	Measurement Error (%)
V_Vert	0.0437	1.3
V_Hor	0.0445	1.5
V_45	0.0428	1.34
H_Vert	0.042	0.91
H_Hor	0.0411	0.89
H_45	0.0421	1.3
45Ts_Vert	0.0438	1.4
45Ts_Hor	0.0404	1.4
45Ts_45	0.0396	1.5
45Ds_Vert	0.0398	1.5
45Ds_Hor	0.0411	1.4
45Ds_45	0.0377	1.5

Table 4.3: R_s measurements for As-built PBF samples at 5.8GHz

Build Orientation	R_s	Measurement Error (%)
V_Vert	0.0605	0.99
V_Hor	0.058	0.95
V_45	0.0578	0.93
H_Vert	0.0632	1.3
H_Hor	0.065	1.1
H_45	0.0621	1.5
45Ts_Vert	0.0523	1.1
45Ts_Hor	0.0519	1.1
45Ts_45	0.0552	1
45Ds_Vert	0.0614	1.7
45Ds_Hor	0.0568	1.8
45Ds_45	0.0627	1.9

The method is so reproducible (N = 3) that the errors are very small, so difficult to see. Hence this emphasis for the high statistical significance of the difference measured.

Table 4.4: R_s measurements for As-built PBF samples at 8.9GHz

Build Orientation	R_s	Measurement Error (%)
V_Vert	0.071	0.95
V_Hor	0.069	0.94
V_45	0.0687	0.97
H_Vert	0.0781	0.96
H_Hor	0.0772	1
H_45	0.0821	1.3
45Ts_Vert	0.0802	1.8
45Ts_Hor	0.0746	1.1
45Ts_45	0.731	1.5
45Ds_Vert	0.74	1.1
45Ds_Hor	0.748	1.1
45Ds_45	0.692	1.1

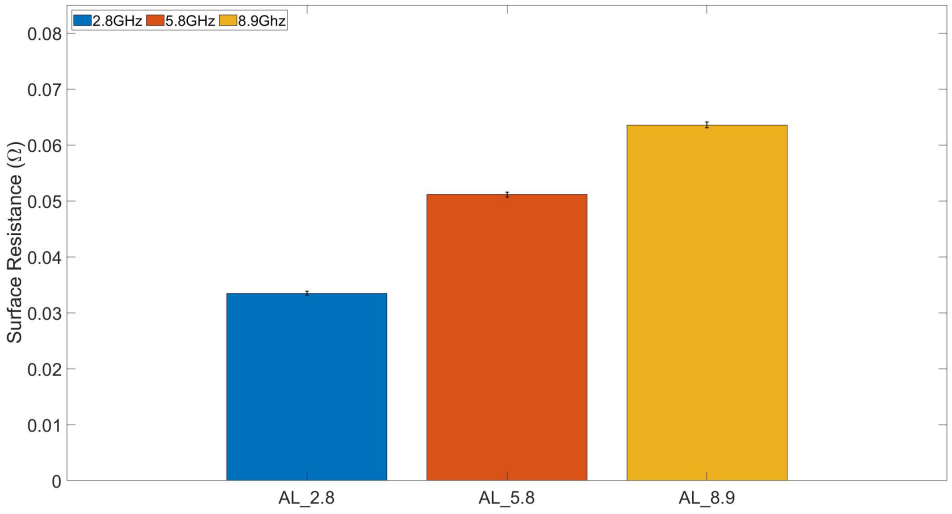

Figure 4.5: Surface Resistance measurements of machined CNC aluminum over 2.8, 5.8 and 8.9GHz

Table 4.5: R_s measurements of bulk aluminium measured at 2.8GHz, 5.8GHz and 8.9 GHz (standard error estimated from N=3 sample)

Frequency (GHz)	R_s	Measurement Error (%)
2.8	0.0335	0.92
5.8	0.0511	1.2
8.9	0.0364	1.3

As can be seen in Figures 4.3 and 4.4, vertically built PBF parts have a lower R_s values when operating at a higher frequency when compared to all other samples. This would be due to the reduced surface roughness. Since skin depth is reduced due to increased frequency, the effect on surface roughness has more of an impact on R_s as the effective cross sectional area of where current can flow reduces, meaning that surface roughness has a larger contribution to the area over which current can flow. Interestingly, at low frequency (2.8GHz), the 45 degree built downside facing surface performed the best overall, having a R_s of 33.7mΩ to 41.1m Ω, where the worst performance surface at 2.8GHz is the vertically built samples, with a R_s of 42.8mΩ to 44.5mΩ across all measurement orientations. This is a prime example as to why measuring these surfaces over a range of frequencies is important, as we have shown that the surface roughness characteristics have an impact on the R_s,

Another interesting discovery is that applying a magnetic field across 45 degrees at 8.9GHz produced a lower R_s value in all cases except the horizontally built part. The reason for this may be due to the surface having large surface features from the beam line and melt pools, due to the surface under test being the last layer made. However, when compared to its bulk aluminium counterpart, it cannot compete in terms of R_s performance at 8.9GHz, with a value of 63.5mΩ, when compared to the lowest value of the AlSi10Mg part being 68.7mΩ which is for a vertically built sample with the magnetic field applied at 45 degrees, although it is important to consider that inside of the waveguide all other surfaces contribute to R_s, resulting in effective surface resistance $R_{s_{eff}}$. So if we were to assume that each sidewall had the same contribution to losses we can average out our values of R_s to make $R_{s_{eff}}$, so at 8.9 GHz values would be; for a vertically applied magnetic field 75.8mΩ, for a field applied horizontally 73.9mΩ and for a field applied at 45 degrees 73.2mΩ. When compared to its bulk counterpart, there is then a significant difference.

4.5 Conclusions and Further Work

This chapter has investigated the effect of build orientation in tandem with the effect of applying a magnetic field in a different orientation across a range of frequencies. This has given insight into how each surface performs as a result of the skin depth changing. This insight has shown that for high frequency applications, using vertically built parts would reduce losses when compared to all other surfaces tested. It was also found that vertically built parts have the worst performance of all surfaces tested at low frequencies, where at 2.8GHz the 45 degree downside facing surface has the best performance in terms of low R_s. These results provide a better understanding of how the orientation of a PBF build can affect the microwave performance and can be used with tools such as COMSOL to incorporate these findings into design protocols.

There are many aspects that are still unknown that contribute to understanding how R_S changes over a range of frequencies for a PBF sample. If further work were to continue, one of the most important steps is understanding the physical geometry by using a drag profile, as this would quantify surface roughness and if there are any correlated characteristics which perform better at different frequencies when applying a magnetic field in different directions. Another aspect which would serve of great importance to understand and optimise for PBF would be build parameters, ranging from laser power to beam diameter. With this new broadband technique, we expect all these parameters to be optimised effectively for low R_s and recommend this for future study.

Chapter 5

Effect of Post Processing on Surface Resistance

5.1 Introduction

For PBF the surface finish is important at higher frequency, as the current occupies the outermost region due to the skin depth. One of the ways to improve this is by post-processing of PBF parts. There are a variety of treatment methods available for metal parts that enhance the mechanical properties of PBF parts, such as hot isostatic pressing, which increases the density of a part[123, 124] at the cost of some changes to geometric factors due to shrinkage [125, 126]. Another type of treatment is tempering, which improves the structural composition of the PBF parts[127, 128], while annealing provides an improved electrical conductivity [129, 130]; the last method being bead blasting, which fires small beads to disrupt the surface and removes a small amount of loose material that improves the surface finish[131, 132, 133]. This chapter describes an investigation on how R_S can be imporved with

the use of post-processing techniques, which alter either the micro geometry of the surface or the micro-structure of the materials surface for the PBF samples.

The post processing techniques chosen keep in mind application for real-world uses for PBF parts, as the majority of these techniques being investigated can be used on complicated and single builds as they do no require any need for direct access to the surface to apply the post process. The post-processes treatments chosen will produce three different outcomes so that an effective understanding can be gained, These outcomes are; to remove loose powder on the surface, to replace the surface with a highly conductive surface and to remove the inherent surface and replace it with a CNC machined surface, making it comparable to its bulk counterpart. The samples used in this investigation are all made of AlSi10Mg (since our focus is one microwave device applications) and are produced using the Renishaw RenAM500 additive manufacturing system using their definition parameters for every component.

5.2 Sample Preparation

Surface resistance measurements for a variety of different types of post-processing techniques have been applied to PBF samples. The chosen techniques are silver plating, media tumbling and CNC machining. All of these samples have been measured with the BBPPR so that an overview of their performance can be gathered over a frequency range from C band to X band. The samples are built in the orientations as described in Chapter 4 and, furthermore, the angle at which the magnetic field is applied to the sample is changed to see if any interesting characteristics can be identified. All samples are in the 'as built' state before any surface treatment is applied.

5.2.1 Silver Plating

Silver plating simply applies a layer of silver to the surface, which is an important factor as we know that due to the skin effect, most of the current occupies the outermost region of the conductor. Therefore, by changing the outermost region material with a plating of a material with high electrical conductivity, we can reduce R_S as the current now flows in the less lossy material, as silver is the best electrical conductor at room temperature. For our three resonant frequencies of 2.8GHz 5.8GHz and 8.9GHz, the expected values of R_s are 1.07mΩ, 1.55mΩ and 1.91mΩ, respectively. Since the majority of the current flows withing the skin depth, the plating thickness needs to be of a subsequent thickness so that the current can be occupied within the plating. As the frequency of operation of the BBPPR has a range of 2.8GHz to 8.9GHz, the specification of the silver plating thickness has to be for 2.8GHz as skin depth is thicker for a lower frequency and so by using Equation 2.2, and with the silver having a nominal electrical conductivity of 6×10^7S/m, the minimal thickness of silver plating is $\approx 1.23\mu m$. The silver plating used for this investigation was a semi-bright silver solution with a plating thickness of 5.0 to 7.5μm, which equates to being 4 times the skin depth required for 2.8GHz but is 7 times the skin depth of the highest mode of operation (8.9GHz), which ensures that over the entire spectrum of measurements taken, the current should be within the plating.

A nickel layer was needed to adhere the silver plating to the PBF part as AlSi10Mg oxidises, so this prevents oxidation and also protects AlSi10Mg from the environment, as it limits the overall deposit porosity of sample. The layer thickness of nickel is 3.0 to 5.0μm, which means the maximum added thickness with layers is 12.5μm ; if tests were done using a waveguide this increase would have to be considered within the design as the plating thickness would change the internal dimensions of the waveguide, as it has gone through the plating process and so one would design

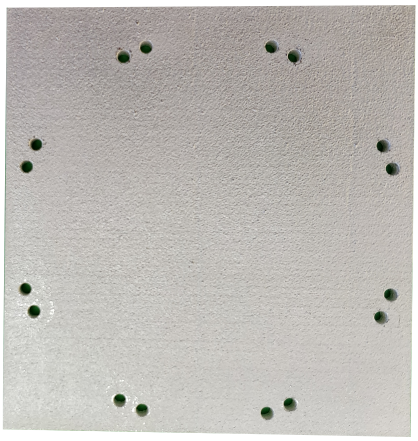

Figure 5.1: Silver plated AlSi10Mg sample produced via PBF which was vertically built. The fixture holes are clearly seen.

the wave guide to have plating of a certain thickness so that it would still operate at your desired frequency. However, due to the use of an end plate replacement, this does not impact the measurement as the only requirements needed for this replacement are a flat and electrically conductive surface. One additional benefit to silver plating is that a silver liquid solution is used during the electro-plating process, which will fill in surface features and produce a new surface profile for the sample, which may have increased benefits such as lower roughness. Hence, the effective R_s is reduced by the double effect of lowering the surface roughness and the increasing of electrical conductivity.

5.2.2 Media Tumbling

The purpose of media tumbling is to remove any loose powder still partially melted to the surface caused by the melt pools of the PBF process. This is achieved by using a medium which is vibrated and 'tumbled' around the part to remove any loose material. In this case, angled cylindrical porcelain was used as the medium

for tumbling as it has minimal abrasion properties, which is desirable due to only wanting to remove the loose powder rather than using a more abrasive media which removes a large amount of material from the sample. This sample can be seen in figure 5.2

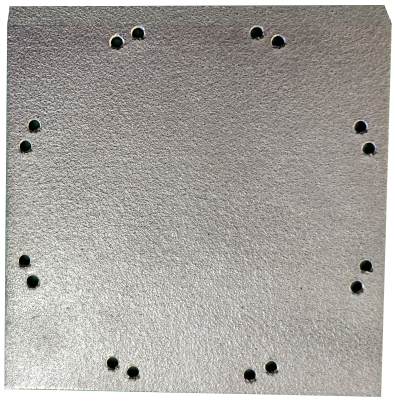

Figure 5.2: Media tumbled AlSi10Mg sample produced via PBF which was built at 45 degrees.

Every sample was tumbled for a duration of 1 hour inside a Frankford vibratory tumbler. To clean the samples after tumbling, isopropyl alcohol and compressed air was used to remove any material which was deposited during the process as loose material from either the media or samples caused by tumbling is dispersed throughout the tumbler and covers everything inside.

5.2.3 CNC Machining

One of the most commonly used manufacturing methods and surface treatment techniques is CNC machining, due to its simplicity relative to application on open surfaces; it is also easily controlled and easily reproducible if machine and tool bits are maintained. The reason for choosing this post-process is that bulk aluminium

parts are also CNC machined, so this can give insight if PBF can be used as an alternative method to produce parts which are then finished with CNC machining. This reduces the time it takes for a CNC machine to be used per part when in a mass fabrication environment. The machined AlSi10Mg sample can be seen in Fig 5.3

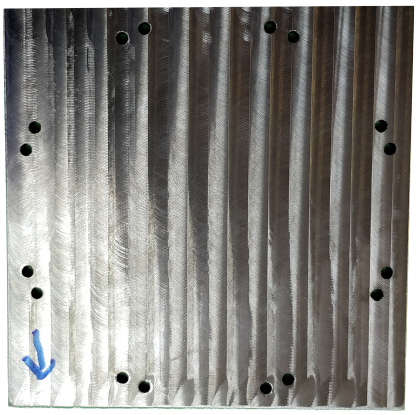

Figure 5.3: CNC machined sample AlSi10Mg sample produce via PBF which was vertically built.

However, though this process can be applied to a sample plate as it has exterior facing surfaces that are exposed, application to a structure such as a waveguide would be next to impossible. If a complete waveguide structure were to be made using the PBF process as a single part, due to the size of the tools needed and the potential complexity of the structure, it would be difficult to impossible to apply a surface finish via CNC machining.

5.3 Measurement Protocol

Similarly to the measurement procedure described in Chapter 4, the screws on the BBPPR was tightened to a 2Nm torque rating to ensure no warping of parts, caused

by over the tightening of the samples. The number of samples produced for each post-process was three, as in Chapter 4 samples, which were built at a angular elevations of 0, 45, and 90 degrees. Another factor to consider is that each post-process was measured at different occasions, although calibration was done at the beginning of each session and every 3 hour interval so that changes in temperature throughout the day (up to 5°C) could be accounted for during calibration. Calibration was also done at the end of every session. For every sample, 3 individual measurements were taken so that a complete and comprehensive data set could be produced, with standard error analysis as before. In addition, in Chapter 4 there were measurements taken with a magnetic field applied in 3 directions on the sample shown in Fig 4.2, so a total of 9 measurements were taken for each sample. With the PBF samples, other materials have been tested and will be reported. Along with these measurements, CNC and media tumbled bulk aluminium samples will be shown as a comparison to their PBF counterparts, and copper PCB will be added as a comparison for silver plating on the surface, as these are both highly conductive materials so merit such a comparison.

5.4 Surface Resistance Measurements

The results gathered are shown in Fig 5.5-5.7 and show the average R_S for each post-processing technique at 3 different frequencies (2.8GHz, 5.8GHz, 8.9GHz). Also shown are the results when applying a magnetic field in 3 different directions.

5.4.1 Tumbled Media

The results gathered from these experiments showed that media tumbling was the worst performing post-process at high frequencies of 8.9GHz and actually increased the value of R_S when compared to its as-built counterpart measured in Chapter 4. Although the R_S does increase at higher frequencies, there is a slight improvement when operating at 2.8GHz, so for a low frequency application there is a justification for this post-process. However, one huge difference is that the bulk sample which was media tumbled has significantly higher losses when compared to their PBF counterparts. This could be caused by a number of different factors, but the main reason could be that the sample was much smaller compared to the square PBF sample, so it was able to move more freely inside the tumbler, enhancing the effects of the tumbling process and significantly altering the surface of the material, and therefore increasing the R_S.

Another outcome is that even though the time in the media tumbler was controlled and the samples were tumbled in fresh media, inconsistencies between all of the samples are larger when operated at higher frequencies. Multiple points arise: that at 8.9GHz the surface finish does have a impact on R_S and that media tumbling does not have the consistency to produce repeatable results; the intended purpose of this process was to remove the partially melted powder on the surface, but what it in fact does is randomly remove material from the surface, which has a larger impact on R_S. Instead, a shorter duration inside the tumbler is more appropriate, just to remove the loose powder before tumbling starts to remove the main body material of the part. The apparent poor performance at high frequency validates the point at which media processing is complete produces a rough surface, as a result increasing R_S. This is expected since at lower frequency this roughness becomes unnoticeable between samples and the differences between each build orientation is

removed, unlike the as-built samples described in Chapter 4. The range between all measured R_S is only 5 % between all values other media tumbling at 2.8GHz.

Interestingly, the characteristic of poorer performance for the downside surface with magnetic field applied in both vertical and at 45 degrees when measured at 5.8GHz shows that the samples themselves may have an issue for their uncharacteristic increased losses at 5.8GHz; all other samples measured at 5.8GHz when media tumbled have R_s between 0.0556Ω - 0.0596Ω and having a measurement of nearly 20% larger may be caused by a issue with the samples. This can be observed in Chapter 4 but was dismissed as the performance was similar to the horizontally built samples, but after post-processing it is clear that there may be an issue with the surface or the material, as the error between them shows a standard error of only 0.5% and 0.7%, respectively, implying the issue is consistent across samples.

Table 5.1: Copper PCB R_s measurements at 2.8GHz, 5.8GHz and 8.9GHz

Frequency (GHz)	R_s (Ω)	Measurement Error (%)
2.8	0.0205	0.94
5.8	0.0296	0.98
8.9	0.0363	1

Table 5.2: Media tumbled R_s measurements of bulk aluminium at 2.8GHz, 5.8GHz and 8.9GHz

Frequency (GHz)	R_s (Ω)	Measurement Error (%)
2.8	0.0465	1.1
5.8	0.047	0.9
8.9	0.0948	1.2

Table 5.3: CNC machined bulk aluminium R_s measurements at 2.8GHz, 5.8GHz and 8.9 GHz

Frequency (GHz)	R_s (Ω)	Measurement Error (%)
2.8	0.0335	0.92
5.8	0.0511	1.2
8.9	0.0636	1.3

Table 5.4: Measurement Sample Description Modifiers for all Post-Processed Samples

Sample ID	Measurement Modifier
Cu	copper PCB
Al _MT	Bulk aluminium media tumblered
Al _CNC	Bulk aluminium CNC machined
MT _	Media tumbled
SP _	Silver plated
M _	CNC machined
V _	Vertically built sample
H _	Horizontally built sample
45Ts _	45 degree built sample and topside surface
45Ds _	45 degree built and sample downside surface
Vert	Magnetic field applied vertically on the sample
Hor	Magnetic field applied horizontally on the sample
45	Magnetic field applied 45 degrees on the sample

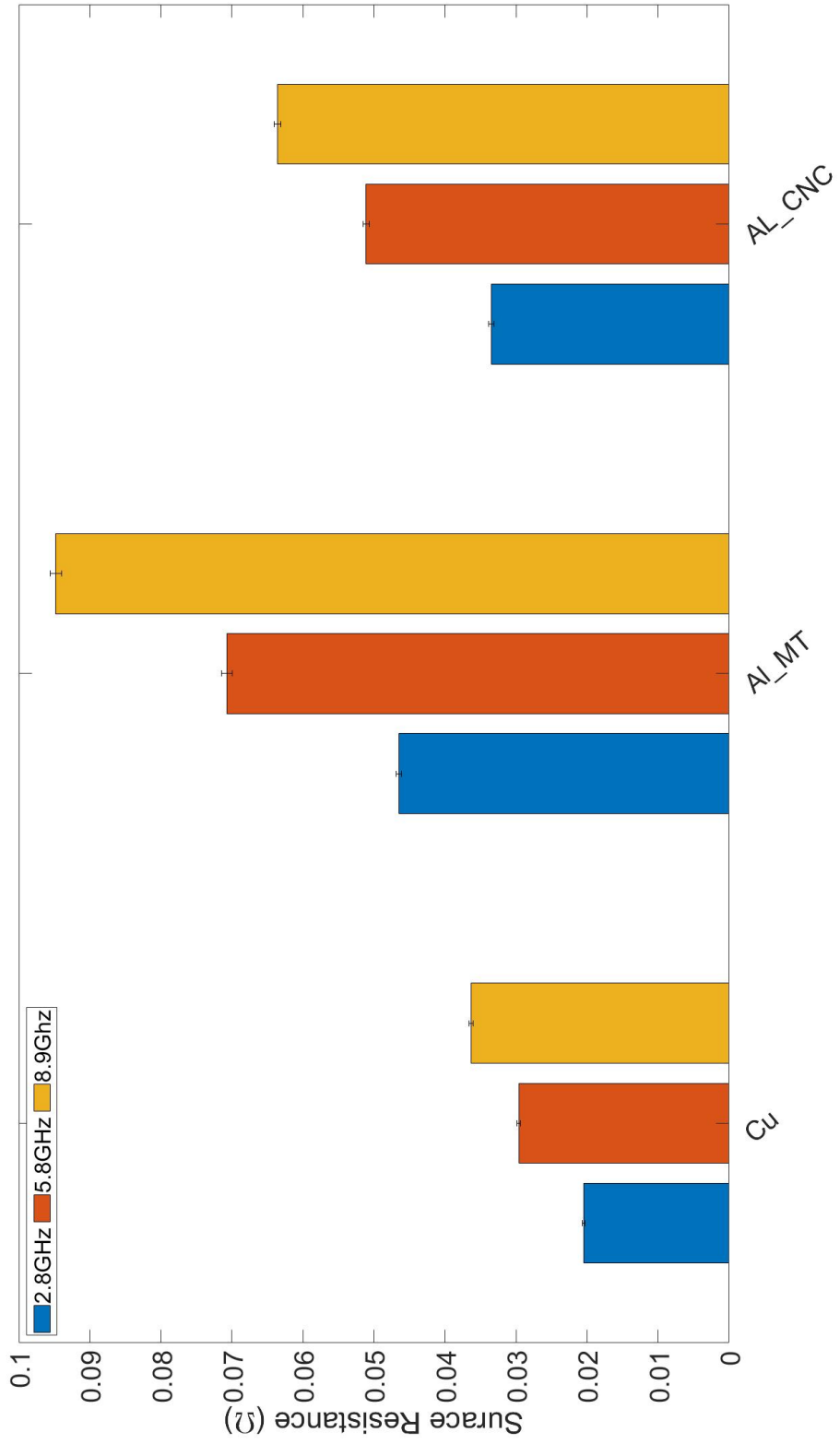

Figure 5.4: R_S Measurements of PCB bulk CNC aluminum and media tumbler aluminum at frequencies of 2.8GHz, 5.8GHz and 8.9GHz.

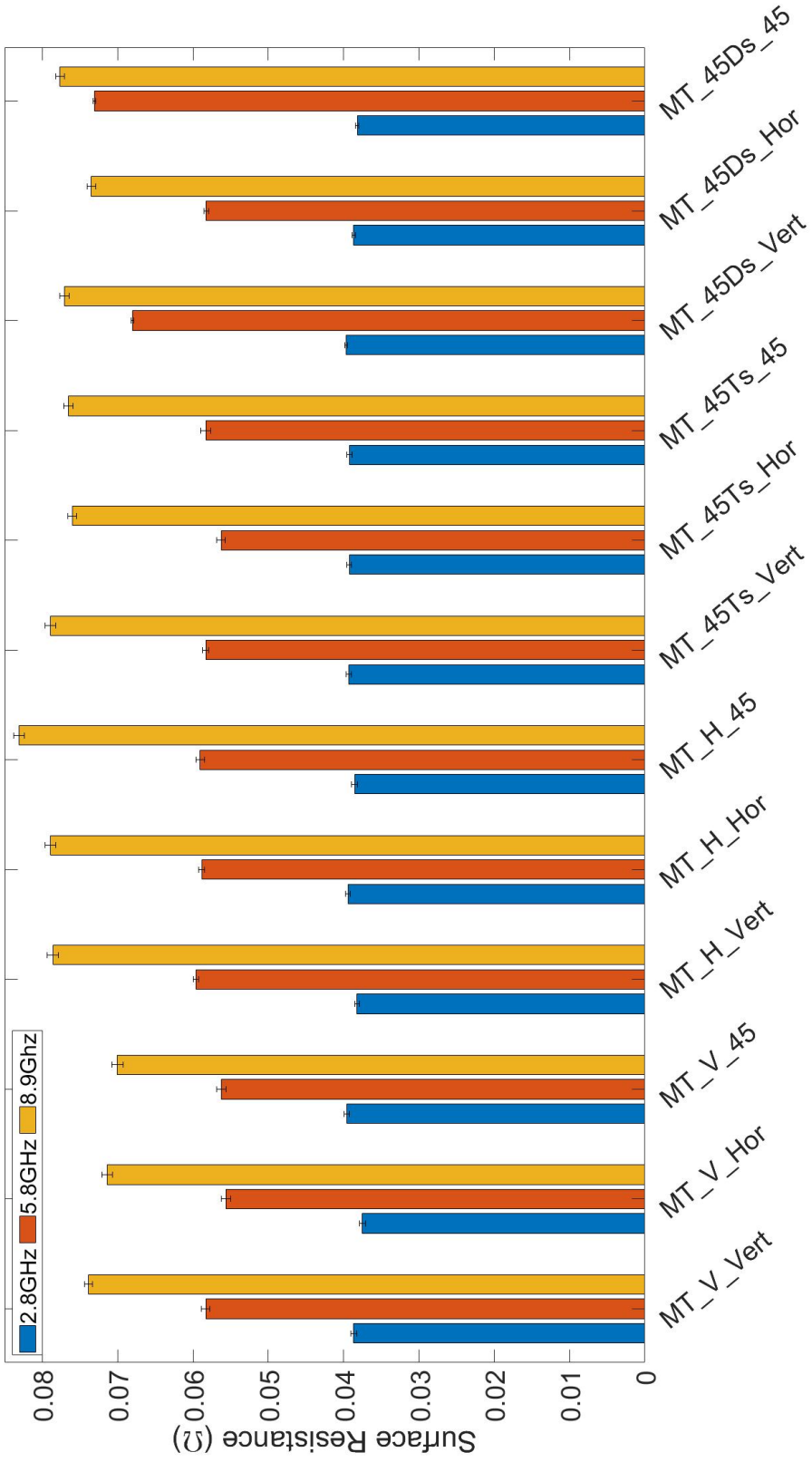

Figure 5.5: Media tumbled AlSi10Mg sample produced via PBF which was built at 45 degrees.

Table 5.5: R_s measurements of PBF samples when media tumbled at 2.8GHz

Build Orientation	R_s (Ω)	Measurement Error (%)
MT_V_Vert	0.0387	0.97
MT_V_Hor	0.0375	0.95
MT_V_45	0.0396	1
MT_H_Vert	0.0382	1.1
MT_H_Hor	0.0394	1.4
MT_H_45	0.0385	1
MT_45Ts_Vert	0.0393	1.1
MT_45Ts_Hor	0.0393	1.2
MT_45Ts_45	0.0392	1
MT_45Ds_Vert	0.0396	2.2
MT_45Ds_Hor	0.0387	2
MT_45Ds_45	0.0382	1.6

Table 5.6: R_s measurements of PBF samples when media tumbled at 5.8GHz

Build Orientation	R_s (Ω)	Measurement Error (%)
MT_V_Vert	0.0583	1
MT_V_Hor	0.0556	0.9
MT_V_45	0.0562	0.94
MT_H_Vert	0.0596	1.6
MT_H_Hor	0.0588	1.5
MT_H_45	0.059	1.1
MT_45Ts_Vert	0.0583	1.5
MT_45Ts_Hor	0.0563	0.96
MT_45Ts_45	0.0583	0.91
MT_45Ds_Vert	0.068	4
MT_45Ds_Hor	0.0582	1.9
MT_45Ds_45	0.073	4.7

Table 5.7: R_s measurements of PBF samples when media tumbled at 8.9GHz

Build Orientation	R_s (Ω)	Measurement Error (%)
MT_V_Vert	0.0739	1.38
MT_V_Hor	0.0714	0.98
MT_V_45	0.07	1
MT_H_Vert	0.0786	1
MT_H_Hor	0.079	1.1
MT_H_45	0.0831	1.2
MT_45Ts_Vert	0.0789	1.1
MT_45Ts_Hor	0.076	1.3
MT_45Ts_45	0.0765	1.2
MT_45Ds_Vert	0.077	1.3
MT_45Ds_Hor	0.0735	1.4
MT_45Ds_45	0.0776	1.2

5.4.2 CNC Machined

As can be expected from CNC machining, which it is controlled with a program written in G-code which is a coordinate based language which gives actions to a machine to ensure repeatability throughout each machining process, the results for R_s are very similar and consistent across the samples. A trend can be seen in some cases in each group of measured build orientation of parts, when the magnetic field is applied vertically and in some cases of applying the field at 45 degrees, R_S is increased at 2.8GHz. This trend, however, is interesting as at lower frequency the effects on R_S should be minimal and should be more apparent at 8.9GHz. However, this leads one to believe that this isn't caused by a rough surface, or by any inherent properties from the PBF process, but in fact could potentially be caused by CNC machining as this may introduce stress fractures within the part as they were only 5mm thick samples, which could affect the interior structure of the part. Similarly the CNC part may have gone through local heating and cooling cycles during each pass of the CNC tool, causing the part to go through heat fluctuations, though coolant is applied to the cutting bit. The increased internal temperature may cause a difference between some samples, which affects the lower frequency measurements due to the increased skin depth and less to the higher frequency measurements.

Compared to their bulk counterparts, the PBF and bulk aluminium, as can be seen, have similar characteristics but in terms of R_S it can be seen that PBF actually performs better. This could be due to different CNC parameters being used for the CNC tooling path, although both had the CNC tooling path to run lengthways along the samples. The speed at which the tool head moves and the RPM of the tool head could cause differences in surface roughness and therefore R_S, as these were machined on different occasions. Even tool wear may potentially cause differences in performance at higher frequencies due to inefficiencies of the cutting tool as it

approaches its end of life [134]. Although all PBF samples were machined together, the surface roughnesses should be similar; this is shown by the higher frequency mode at 8.9GHz, where the effects of the surface roughness on R_S is enhanced at the smaller skin depth, so when operating at higher frequencies the evaluation of the surface roughness becomes easier to identify R_S measurements.

We can conclude that the performance from parts post-processed via CNC machining is a result of their new surface profile compared with as-built. The last point from these CNC parts is that changing the orientation of the applied magnetic field did not have any noticeable effect on R_S, which was not expected. A visual inspection identifies a uniform textured surface on the sample, with patterns where it is noticeably rougher in one orientation than the other. The cause for this may be due to the peaks and troughs within the rough surface being wider and less sharp, meaning that the current along the surface has an easier path to travel as the average surface roughness is less.

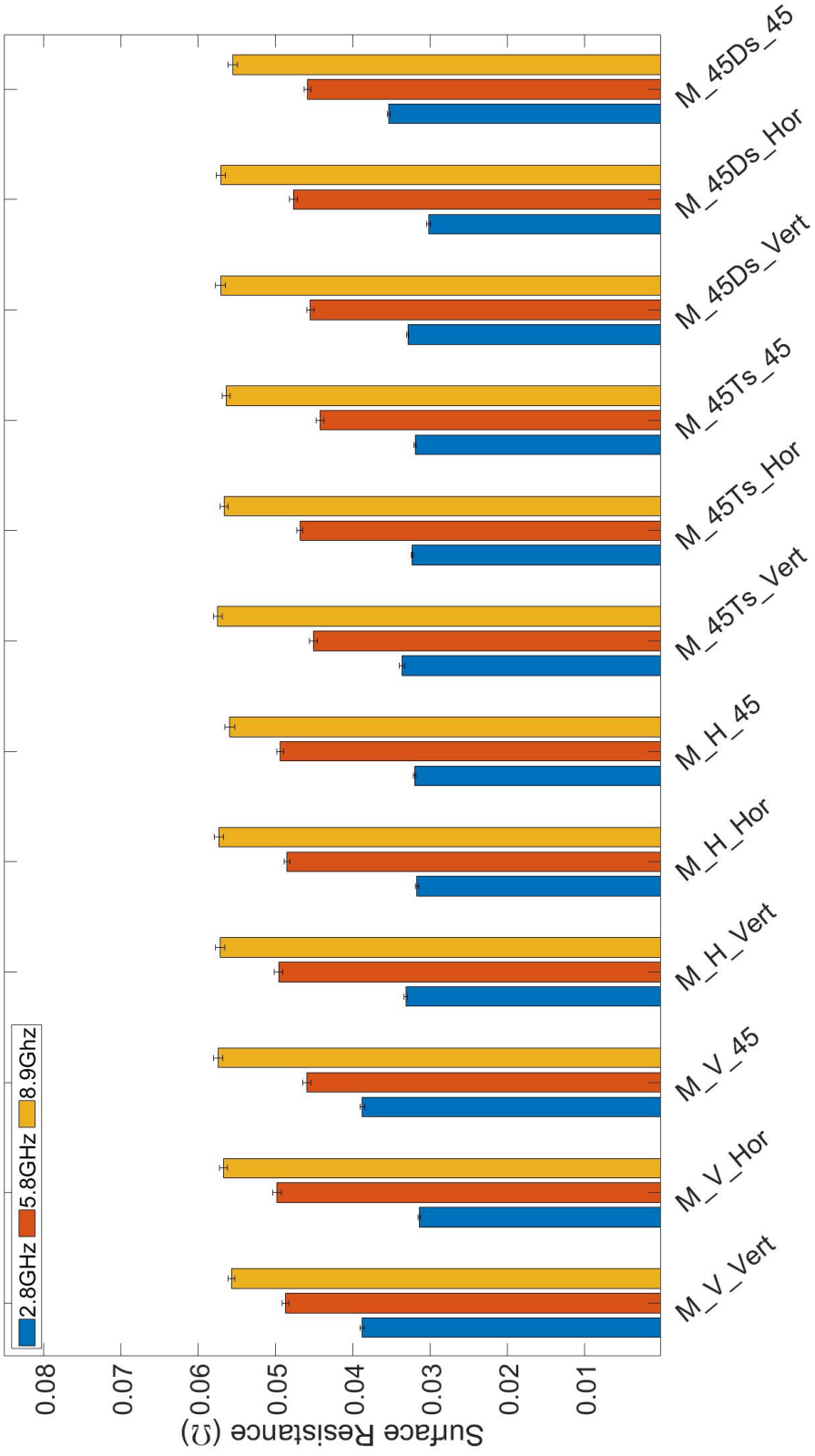

Figure 5.6: CNC machined AlSi10Mg sample produced via PBF which was built at 45 degrees.

Table 5.8: R_s measurements of PBF samples when CNC machined at 2.8GHz

Build Orientation	R_s (Ω)	Measurement Error (%)
M_V_Vert	0.0388	1.5
M_V_Hor	0.0314	1.8
M_V_45	0.0388	1.2
M_H_Vert	0.0331	1.6
M_H_Hor	0.0317	1.7
M_H_45	0.032	1.7
M_45Ts_Vert	0.0336	0.94
M_45Ts_Hor	0.0323	2.1
M_45Ts_45	0.0319	2.5
M_45Ds_Vert	0.0329	2.3
M_45Ds_Hor	0.0301	1.1
M_45Ds_45	0.0354	2.1

Table 5.9: R_s measurements of PBF samples when CNC machined at 5.8GHz

Build Orientation	R_s (Ω)	Measurement Error (%)
M_V_Vert	0.0487	1.1
M_V_Hor	0.098	1.3
M_V_45	0.0459	0.89
M_H_Vert	0.0496	0.95
M_H_Hor	0.0485	1.2
M_H_45	0.0494	1.1
M_45Ts_Vert	0.0451	0.92
M_45Ts_Hor	0.0468	1.3
M_45Ts_45	0.0442	0.89
M_45Ds_Vert	0.0455	1
M_45Ds_Hor	0.0477	0.96
M_45Ds_45	0.0459	1.1

Table 5.10: R_s measurements of PBF samples when CNC machined at 8.9GHz

Build Orientation	R_s (Ω)	Measurement Error (%)
M_V_Vert	0.0557	1.3
M_V_Hor	0.0567	1.1
M_V_45	0.0574	1
M_H_Vert	0.0572	0.9
M_H_Hor	0.0573	0.9
M_H_45	0.0559	0.93
M_45Ts_Vert	0.0575	1
M_45Ts_Hor	0.0566	1.1
M_45Ts_45	0.0564	1.1
M_45Ds_Vert	0.0571	0.92
M_45Ds_Hor	0.0571	0.99
M_45Ds_45	0.0555	0.93

5.4.3 Silver Plating

As can be expected for when the samples are plated to a silver thickness greater than the multiple skin depths, the entire sample exhibits the electrical conductivity properties of the plated silver metal. Therefore, the improvement in R_S is due not only to the potential improvement in surface roughness when plating, but also to the change in the surface conductivity of the samples being tested. So when looking at improvements after post-processing, it is clear that silver plating is the best.

In some cases the R_S value measured at 8.9GHz of the silver samples is lower than the measured R_S at 2.8GHz of the as built samples. Although compared to a copper PCB, the copper has a lower R_S of 20.5mΩ at 2.8GHz when compared to the siver plated samples, which had a average value of value of 22.4mΩ, which is a difference of $\approx 7\%$; at a higher frequency copper had a R_S of 36.4mΩ and silver had an average value of 41.7mΩ, which is a greater difference of $\approx$13%. This can be due to multiple factors, one main point is that the plating of 'Semi - Bright Silver' may not be pure silver and so to expect a pure silver representation of the plating may be false and so, due to impurities, the conductivity of the material to be less than bulk silver. Another contribution is that although the roughness of the part may be reduced due to plating, there may be some inherent structural properties such as leaving small pockets of unplated material due to the plating forming above extreme surface features. An example of the samples having a large impact to the surface is evident when looking at both downside facing surfaces when the magnetic field is applied horizontally and at 45 degrees, as these show uncharacteristic behaviour, where R_s at 2.8GHz is 36% larger than at 8.9GHz, which shouldn't be the case.

This could be caused by a combination of two factors which are either a plating issue (but since both R_S measurements at 2.8 and 8.9 GHz are as expected this is

unlikely to be the case), or measurment, but this can't be the case as these samples were remeasured again to ensure that there was no measurement error (the results had a difference of 1% which is well within measurement error). What may be the issue is due to the nature of the BBPPR where high magnetic field is applied of different regions to the samples when resonating at different frequencies, so these different locations (paired with other variables such as silver plating and surface roughness) may cause this unique result to occur.

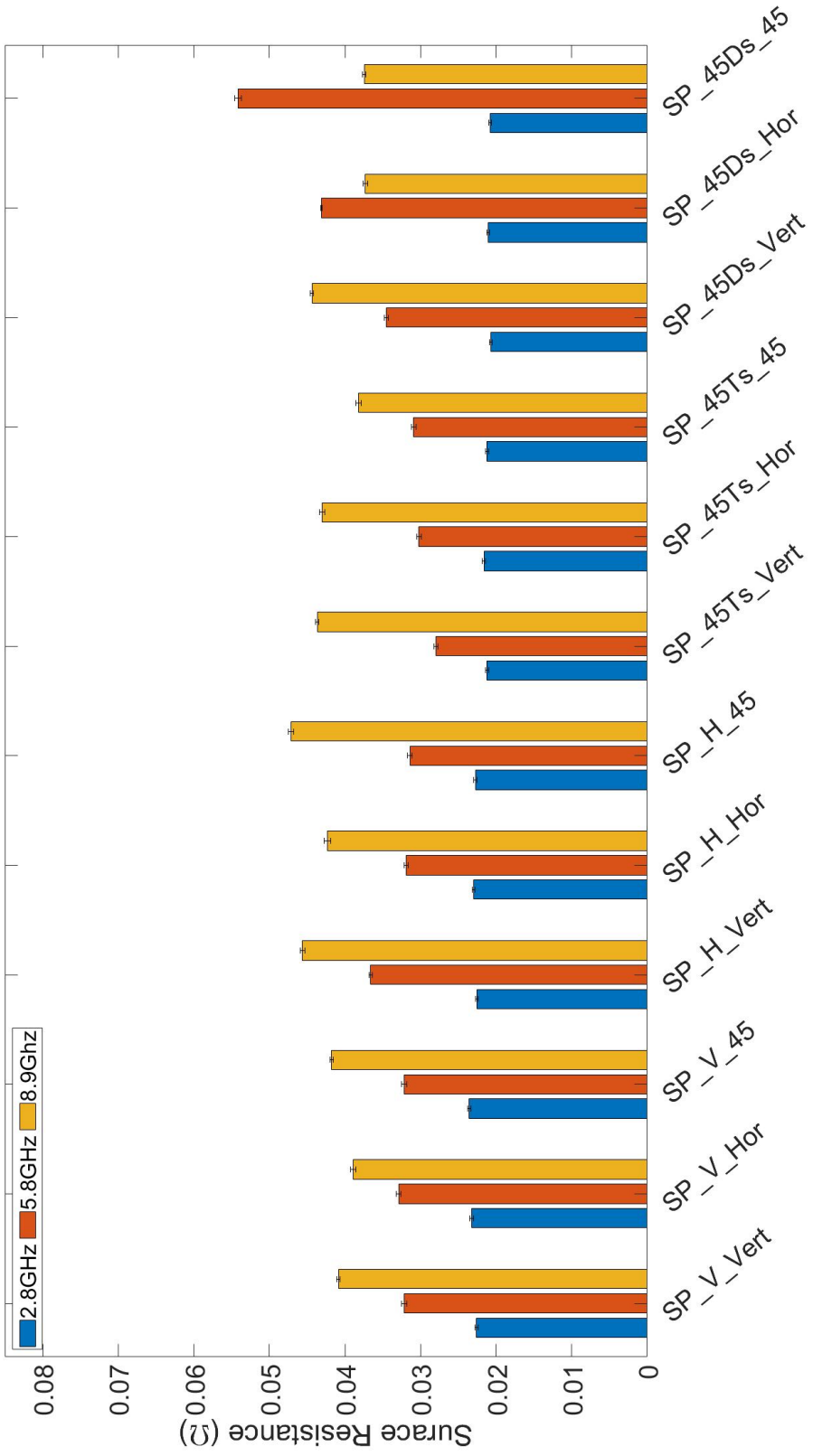

Figure 5.7: Silver plated AlSi10Mg sample produced via PBF which was built at 45 degrees.

Table 5.11: R_s measurements of PBF samples when silver plated at 2.8GHz

Build Orientation	R_s (Ω)	Measurement Error (%)
SP_V_Vert	0.0226	0.95
SP_V_Hor	0.0232	1
SP_V_45	0.0236	1.2
SP_H_Vert	0.0225	1.1
SP_H_Hor	0.023	1.2
SP_H_45	0.0228	1.3
SP_45Ts_Vert	0.0212	0.95
SP_45Ts_Hor	0.0216	1.1
SP_45Ts_45	0.0212	0.97
SP_45Ds_Vert	0.0207	1.2
SP_45Ds_Hor	0.0211	1.4
SP_45Ds_45	0.0208	1.1

Table 5.12: R_s measurements of PBF samples when silver plated at 5.8GHz

Build Orientation	R_s (Ω)	Measurement Error (%)
SP_V_Vert	0.0322	0.94
SP_V_Hor	0.0329	1.1
SP_V_45	0.0322	1
SP_H_Vert	0.0366	1.9
SP_H_Hor	0.0319	1.2
SP_H_45	0.0314	1
SP_45Ts_Vert	0.028	1.1
SP_45Ts_Hor	0.0302	1.1
SP_45Ts_45	0.0309	1
SP_45Ds_Vert	0.0345	1.3
SP_45Ds_Hor	0.0431	1.0
SP_45Ds_45	0.0541	3.9

Table 5.13: R_s measurements of PBF samples when silver plated at 8.9GHz

Build Orientation	R_s (Ω)	Measurement Error (%)
SP_V_Vert	0.0409	1.8
SP_V_Hor	0.0389	1
SP_V_45	0.0418	2
SP_H_Vert	0.0456	1.7
SP_H_Hor	0.0423	1
SP_H_45	0.0471	1.4
SP_45Ts_Vert	0.0437	1.9
SP_45Ts_Hor	0.043	1.3
SP_45Ts_45	0.0382	1.2
SP_45Ds_Vert	0.0443	2
SP_45Ds_Hor	0.0373	1.1
SP_45Ds_45	0.0375	1.6

5.5 Conclusion and Future Work

This chapter has shown the effects of applying post-processing techniques to improve the electrical performance of AlSi10Mg samples produced with PBF and has measured their performance at 2.8GHz, 5.8GHz and 8.9GHz in terms of R_s. The results show that the best performance is achieved when parts are silver plated, which is mainly due to the current passing through the plating rather than the AlSi10Mg, meaning that R_S would inherently be less. When comparing other post-processing methods, where the surface currents only travel through the AlSi10Mg, CNC machining showed significant improvements when compared to media tumbling. Using media tumbling increases R_S when compared to as-built samples when operating at 8.9GHz, but also improves R_S at 2.8GHz. Future work could involve more controlled tests on all post processes, as one test which could be carried out is measuring the effect of media tumbling over time spent tumbled, so that effects on the electrical properties of PBF can be measured and a better understanding of media tumbling for PBF gained to optimise R_S for microwave applications. One major aspect that is missing is again the measurement of surface roughness, which will provide better insight into how the post-processing treatment affects the surface, rather than extrapolating R_S measurements as a sign of surface roughness.

Chapter 6

Final Summary and Future Work

The focus of this thesis has been the electrical properties of PBF manufacturing AlSi10Mg over a range of microwave frequencies with a single sample. Multiple techniques were either deployed in a novel way, or novel measurement fixtures were designed and built to carry out these measurements. With studies into the effect of applying a magnetic field in different orientations for as-built samples using AlSi10Mg alloy, and studies the effects of post-processing of these samples to gain a better understanding how these processes affect the R_S over a range of frequencies, we have obtained a better understanding of the role of post-processing when applied to microwave device applications.

6.1 Measurement Methods for Microwave Surfaces

Three measurement techniques have been proposed with the objective of being able to measure a single PBF sample over a range of microwave frequencies within a single structure so that an understanding can be gained about the R_S performance

of PBF. The three methods proposed were the FPOR, CR and the BBPPR. The FPOR shortcomings came from its mechanical design, reducing its measurement frequency range with one sweep, also with issues with coupling rasing the background signal due to being strongly coupled, resulting in this technique being dropped and a new technique was proposed. The CR was proposed as the current travels along the centre conductor, which was going to become the sample; however, after further investigation and planning the tests to be carried out, it was decided that the sample would be too small and delicate to apply surface treatment, so again a new resonant structure had to be implemented. The last method BBPPR, followed the same principles to achieve its resonance defined by the length of its reference wall, but unlike in the CR the sample would be an end plate replacement to ensure that any flat, electrically conductive sample size could be measured. Additionally, a directional magnetic field is applied to samples so that a anisotropic measurements could be taken to measure R_S values in certain directions.

One of the main pieces of future work would be further development of the FPOR system, as it has the potential to become a measurement technique which can measure PBF over a range of frequencies without any gaps within the data, unlike CR and BBPPR which has discrete frequencies where measurements can occur; the FPOR could also be extended to mm-wave frequencies where AM parts have not yet been deployed. Another aspect of future work would be increasing the operating frequency of BBPPR so that a broader frequency range of resonances can be used to produce a better and more comprehensive data set.

6.2 Build Orientation and Surface Orientation

A range of build orientations for PBF were chosen to see if the angle at which a part is made has inherently worse R_S performance across a range of frequencies, when applying a magnetic field in a single direction to evaluate the electrical surface performance of the sample. It was found that vertically built parts had the best performance at 8.9GHz but also the worst at 2.8GHz. The most important future work that can be done is to perform surface roughness measurements on all samples to directly correlate these data with surface roughness so that a better understanding can be gained.

6.3 Post Processing Treatment

Post-processing treatment has been applied to PBF samples built at 3 different orientations, the post-processing techniques being media tumbling, CNC machining and silver plating. Results gathered for R_S of each post-process showed that the most inconsistent surface finish was produced by media tumbling; the values of R_S are inconsistent and follow no pattern that correlates with either the build orientation of samples, or between the application direction of current to the surface. One process that did show consistency was CNC machining, which even had better performance than its bulk aluminium counterpart. Silver plating showed the best performance overall, as plating the sample changes the material under test at high frequencies, though an important take away is that when compared to a copper PCB sample, the copper had a lower R_S, its value meaning that either the silver plating isn't pure or the inherent roughness of the sample plays an important part in the overall evaluation of R_S. This could be investigated by measuring the solution of the bright

silver or by measuring a ideally flat sample plated by bright silver eliminating the roughness present from the PBF sample and having only the roughness from the plating process itself.

For further work in this area, again surface roughness analysis would be the next step so that a better understanding can be gained from the post-processing treatments when applied to PBF samples. Another step could be taken into controlling all samples going through treatment for CNC machining, e.g. depth of cut, RPM of head and speed at which the tool head moves across a part and tool wear state to see if the age of the tool has a significant impact to surface roughness of PBF parts. For media tumbling, either change of tumble media used and the duration of tumbling and the effect it has on R_S merit further investigation.

References

[1] Leonidas Gargalis, Vincenzo Madonna, Paolo Giangrande, Roberto Rocca, Mark Hardy, Ian Ashcroft, Michael Galea, and Richard Hague. Additive manufacturing and testing of a soft magnetic rotor for a switched reluctance motor. *IEEE Access*, 8:206982–206991, 2020. ISSN 21693536. doi: 10.1109/ACCESS.2020.3037190.

[2] Diego Manfredi, Flaviana Calignano, Manickavasagam Krishnan, Riccardo Canali, Elisa Paola, Sara Biamino, Daniele Ugues, Matteo Pavese, and Paolo Fino. Additive Manufacturing of Al Alloys and Aluminium Matrix Composites (AMCs). In *Light Metal Alloys Applications*. InTech, 6 2014. doi: 10.5772/58534.

[3] Innovate UK. *A landscape for the future of high value manufacturing in the UK*. 2017.

[4] Andrew J. Pinkerton. [INVITED] Lasers in additive manufacturing. *Optics & Laser Technology*, 78:25–32, 4 2016. ISSN 0030-3992. doi: 10.1016/J.OPTLASTEC.2015.09.025.

[5] Avinash Sharma and Carl Carpenter. Additive Manufactured Antenna for NASA's Interstellar Mapping and Acceleration Probe (IMAP). *2023 United States National Committee of URSI National Radio Science Meeting,*

USNC-URSI NRSM 2023 - Proceedings, pages 3–4, 2023. doi: 10.23919/USNC-URSINRSM57470.2023.10042985.

[6] Bing Zhang and Herbert Zirath. Metallic 3-D Printed Rectangular Waveguides for Millimeter-Wave Applications. *IEEE Transactions on Components, Packaging and Manufacturing Technology*, 6(5):796–804, 5 2016. ISSN 2156-3950. doi: 10.1109/TCPMT.2016.2550483.

[7] Talal Skaik, Milan Salek, Peter Hunyor, Hui Wang, Peter G. Huggard, Paul F. Wilson, Mark A. Williams, and Yi Wang. Evaluation of 3-D Printed Monolithic G-Band Waveguide Components. *IEEE Transactions on Components, Packaging and Manufacturing Technology*, 13(2):240–248, 2 2023. ISSN 21563985. doi: 10.1109/TCPMT.2023.3243002.

[8] Chetan M. Thakar, Shailesh S. Parkhe, Ankit Jain, Khongdet Phasinam, G. Murugesan, and Randy Joy Magno Ventayen. 3d Printing: Basic principles and applications. *Materials Today: Proceedings*, 51:842–849, 1 2022. ISSN 2214-7853. doi: 10.1016/J.MATPR.2021.06.272.

[9] Sofia Aquino Monteiro, Camila Scheid, Monique Deon, and Josias Merib. Fundamentals, recent applications, and perspectives of 3D printing in sample preparation approaches. *Microchemical Journal*, page 109385, 9 2023. ISSN 0026-265X. doi: 10.1016/J.MICROC.2023.109385. URL `https://linkinghub.elsevier.com/retrieve/pii/S0026265X23010044`.

[10] Sebastian Hällgren, Lars Pejryd, and Jens Ekengren. Additive Manufacturing and High Speed Machining -cost Comparison of short Lead Time Manufacturing Methods. *Procedia CIRP*, 50:384–389, 1 2016. ISSN 2212-8271. doi: 10.1016/J.PROCIR.2016.05.049.

[11] J. P. Kruth, M. C. Leu, and T. Nakagawa. Progress in Additive Manufacturing

and Rapid Prototyping. *CIRP Annals*, 47(2):525–540, 1 1998. ISSN 0007-8506. doi: 10.1016/S0007-8506(07)63240-5.

[12] Jingchao Jiang, Xun Xu, and Jonathan Stringer. Support Structures for Additive Manufacturing: A Review. *Journal of Manufacturing and Materials Processing 2018, Vol. 2, Page 64*, 2(4):64, 9 2018. ISSN 2504-4494. doi: 10.3390/JMMP2040064. URL `https://www.mdpi.com/2504-4494/2/4/64/htmhttps://www.mdpi.com/2504-4494/2/4/64`.

[13] Yi Liu, Peng Zhang, Hang Cheng Zhang, Weiming Wang, Tianqi Song, Xin Yan, Wei Zeng, and Yi Jun Yang. Self-supporting parametric polyhedral structure for 3D printing. *Advances in Engineering Software*, 186:103529, 12 2023. ISSN 0965-9978. doi: 10.1016/J.ADVENGSOFT.2023.103529.

[14] Soyeon Park, Wan Shou, Liane Makatura, Wojciech Matusik, and Kun (Kelvin) Fu. 3D printing of polymer composites: Materials, processes, and applications. *Matter*, 5(1):43–76, 1 2022. ISSN 2590-2385. doi: 10.1016/J.MATT.2021.10.018.

[15] David Kazmer. Three-Dimensional Printing of Plastics. *Applied Plastics Engineering Handbook: Processing, Materials, and Applications: Second Edition*, pages 617–634, 1 2017. doi: 10.1016/B978-0-323-39040-8.00029-8.

[16] Laura Schittecatte, Valérie Geertsen, Daniel Bonamy, Thuy Nguyen, and Patrick Guenoun. From resin formulation and process parameters to the final mechanical properties of 3D printed acrylate materials. *MRS Communications*, 13(3):357–377, 6 2023. ISSN 21596867. doi: 10.1557/S43579-023-00352-3/TABLES/1. URL `https://link.springer.com/article/10.1557/s43579-023-00352-3`.

[17] M. Kurimoto, T. Sawada, T. Kato, and Y. Suzuoki. 3D Printing of 2 layered permittivity-graded material using UV-cured-resin/alumina composite. *Pro-*

ceedings of the IEEE International Conference on Properties and Applications of Dielectric Materials, 2018-May:1010–1013, 6 2018. doi: 10.1109/ICPADM.2018.8401209.

[18] Pedro Gonçalves Martinho. Rapid manufacturing and tooling. *Design and Manufacturing of Plastics Products: Integrating Traditional Methods With Additive Manufacturing*, pages 381–456, 1 2021. doi: 10.1016/B978-0-12-819775-2.00008-5.

[19] S. Rahmati. Direct Rapid Tooling. *Comprehensive Materials Processing*, 10: 303–344, 1 2014. doi: 10.1016/B978-0-08-096532-1.01013-X.

[20] Jigang Huang, Qin Qin, and Jie Wang. A Review of Stereolithography: Processes and Systems. *Processes 2020, Vol. 8, Page 1138*, 8(9):1138, 9 2020. ISSN 2227-9717. doi: 10.3390/PR8091138. URL `https://www.mdpi.com/2227-9717/8/9/1138/htmhttps://www.mdpi.com/2227-9717/8/9/1138`.

[21] Weiyi Wang, Jianhua Ye, Huanming Gong, Xinzhong Pi, Chenghu Wang, and Yujia Xia. Computer-stereolithography-based laser rapid prototyping & manufacturing system. *IFAC Proceedings Volumes*, 32(2):61–66, 7 1999. ISSN 1474-6670. doi: 10.1016/S1474-6670(17)56013-9.

[22] Amit M.E. Arefin, Nava Raj Khatri, Nitin Kulkarni, and Paul F. Egan. Polymer 3D Printing Review: Materials, Process, and Design Strategies for Medical Applications. *Polymers 2021, Vol. 13, Page 1499*, 13(9):1499, 5 2021. ISSN 2073-4360. doi: 10.3390/POLYM13091499. URL `https://www.mdpi.com/2073-4360/13/9/1499/htmhttps://www.mdpi.com/2073-4360/13/9/1499`.

[23] Amit Pariskar, Peeyush Kumar Sharma, Upadhyayula Suryanarayana Murty, and Subham Banerjee. Effect of Tartrazine as Photoabsorber for Improved Printing Resolution of 3D Printed “Ghost Tablets”: Non-Erodible Inert Ma-

trices. *Journal of Pharmaceutical Sciences*, 112(4):1020–1031, 4 2023. ISSN 0022-3549. doi: 10.1016/J.XPHS.2022.11.014.

[24] Young Geun Park, Insik Yun, Won Gi Chung, Wonjung Park, Dong Ha Lee, and Jang Ung Park. High-Resolution 3D Printing for Electronics. *Advanced Science*, 9(8):2104623, 3 2022. ISSN 2198-3844. doi: 10.1002/ADVS.202104623. URL https://onlinelibrary.wiley.com/doi/full/10.1002/advs.202104623https://onlinelibrary.wiley.com/doi/abs/10.1002/advs.202104623https://onlinelibrary.wiley.com/doi/10.1002/advs.202104623.

[25] Diego Betancourt, Klaus Wolf, Dirk Plettemeier, and Frank Ellinger. Additive Manufactured Double-Ridged Horn Antenna for UWB Applications. *Progress in Electromagnetics Research C*, 73:47–53, 2017. ISSN 15309681. doi: 10.2528/PIERC17021410.

[26] B. Jacobs, J. W. Odendaal, and J. Joubert. The Effect of Manufacturing and Assembling Tolerances on the Performance of Double-Ridged Horn Antennas. *http://dx.doi.org/10.1163/156939310791958761*, 24(10):1279–1290, 7 2012. ISSN 09205071. doi: 10.1163/156939310791958761. URL https://www.tandfonline.com/doi/abs/10.1163/156939310791958761.

[27] Bing Zhang, Yong Xin Guo, Hucheng Sun, and Yanjie Wu. Metallic, 3D-Printed, K-Band-Stepped, Double-Ridged Square Horn Antennas. *Applied Sciences 2018, Vol. 8, Page 33*, 8(1):33, 12 2017. ISSN 2076-3417. doi: 10.3390/APP8010033. URL https://www.mdpi.com/2076-3417/8/1/33/htmhttps://www.mdpi.com/2076-3417/8/1/33.

[28] Abdullah Genc, Ibrahim Bahadir Basyigit, Tuna Goksu, and Selcuk Helhel. Investigation of the Performances of X-Ku Band 3D Printing Pyramidal Horn Antennas Coated with the Different Metals.

[29] Sungwoo Lee, Youngoo Yang, Kang Yoon Lee, Kyung Young Jung, and Keum Cheol Hwang. Robust Design of 3D-Printed 6–18 GHz Double-Ridged TEM Horn Antenna. *Applied Sciences 2018, Vol. 8, Page 1582*, 8(9):1582, 9 2018. ISSN 2076-3417. doi: 10.3390/APP8091582. URL https://www.mdpi.com/2076-3417/8/9/1582/htmhttps://www.mdpi.com/2076-3417/8/9/1582.

[30] Rajinth Shanthar, Kun Chen, and Chamil Abeykoon. Powder-Based Additive Manufacturing: A Critical Review of Materials, Methods, Opportunities, and Challenges. *Advanced Engineering Materials*, page 2300375, 8 2023. ISSN 1527-2648. doi: 10.1002/ADEM.202300375. URL https://onlinelibrary.wiley.com/doi/full/10.1002/adem.202300375https://onlinelibrary.wiley.com/doi/abs/10.1002/adem.202300375https://onlinelibrary.wiley.com/doi/10.1002/adem.202300375.

[31] Thomas Duda and L. Venkat Raghavan. 3D Metal Printing Technology. *IFAC-PapersOnLine*, 49(29):103–110, 1 2016. ISSN 2405-8963. doi: 10.1016/J.IFACOL.2016.11.111.

[32] I. Gibson, D. W. Rosen, and B. Stucker. Additive manufacturing technologies: Rapid prototyping to direct digital manufacturing. *Additive Manufacturing Technologies: Rapid Prototyping to Direct Digital Manufacturing*, pages 1–459, 2010. doi: 10.1007/978-1-4419-1120-9/COVER.

[33] Daniel Powell, Allan E.W. Rennie, Louise Geekie, and Neil Burns. Understanding powder degradation in metal additive manufacturing to allow the upcycling of recycled powders. *Journal of Cleaner Production*, 268:122077, 9 2020. ISSN 0959-6526. doi: 10.1016/J.JCLEPRO.2020.122077.

[34] David E. Cooper, Mark Stanford, Kevin A. Kibble, and Gregory J. Gibbons. Additive Manufacturing for product improvement at Red Bull Technology.

Materials & Design, 41:226–230, 10 2012. ISSN 0261-3069. doi: 10.1016/J.MATDES.2012.05.017.

[35] Paolo C. Priarone, Vincenzo Lunetto, Eleonora Atzeni, and Alessandro Salmi. Laser powder bed fusion (L-PBF) additive manufacturing: On the correlation between design choices and process sustainability. *Procedia CIRP*, 78:85–90, 1 2018. ISSN 2212-8271. doi: 10.1016/J.PROCIR.2018.09.058.

[36] Gideon N. Levy, Ralf Schindel, and J. P. Kruth. RAPID MANUFACTURING AND RAPID TOOLING WITH LAYER MANUFACTURING (LM) TECHNOLOGIES, STATE OF THE ART AND FUTURE PERSPECTIVES. *CIRP Annals*, 52(2):589–609, 1 2003. ISSN 0007-8506. doi: 10.1016/S0007-8506(07)60206-6.

[37] Alexander Paolini, Stefan Kollmannsberger, and Ernst Rank. Additive manufacturing in construction: A review on processes, applications, and digital planning methods. *Additive Manufacturing*, 30:100894, 12 2019. ISSN 2214-8604. doi: 10.1016/J.ADDMA.2019.100894.

[38] Yong Huang, Ming C. Leu, Jyoti Mazumder, and Alkan Donmez. Additive manufacturing: Current state, future potential, gaps and needs, and recommendations. *Journal of Manufacturing Science and Engineering, Transactions of the ASME*, 137(1), 2 2015. ISSN 15288935. doi: 10.1115/1.4028725/375256. URL `https://dx.doi.org/10.1115/1.4028725`.

[39] Enea Sacco and Seung Ki Moon. Additive manufacturing for space: status and promises. *International Journal of Advanced Manufacturing Technology*, 105(10):4123–4146, 12 2019. ISSN 14333015. doi: 10.1007/S00170-019-03786-Z/TABLES/7. URL `https://link.springer.com/article/10.1007/s00170-019-03786-z`.

[40] Oscar A. Peverini, Mauro Lumia, Giuseppe Addamo, Giuseppe Virone, and

Nelson J. G. Fonseca. How 3D-Printing Is Changing RF Front-End Design for Space Applications. *IEEE Journal of Microwaves*, 3(2):800–814, 4 2023. ISSN 2692-8388. doi: 10.1109/JMW.2023.3250343.

[41] Jose Antonio Lorente, Monica Martinez Mendoza, Axel Zafra Petersson, Laurent Pambaguian, Alejandro Alvarez Melcon, and Christoph Ernst. Single part microwave filters made from selective laser melting. pages 1421–1424, 12 2022. doi: 10.23919/EUMC.2009.5296127.

[42] Paul Booth and Elena Valles Lluch. Enhancing the Performance of Waveguide Filters Using Additive Manufacturing. *Proceedings of the IEEE*, 105(4):613–619, 11 2016. ISSN 0018-9219. doi: 10.1109/JPROC.2016.2616494.

[43] Paul Booth, Malcolm Skeen, and Simon Stirland. Low cost, short lead-time feed chain components for multi-beam antennas; Low cost, short lead-time feed chain components for multi-beam antennas. *2009 3rd European Conference on Antennas and Propagation*, 2009.

[44] Michael Kilian, Andreas Schinagl-Weiß, Alexander Sommer, Christian Hartwanger, and Michael Schneider. Ku-Band SFB-Cluster manufactured by Additive Manufacturing Techniques; Ku-Band SFB-Cluster manufactured by Additive Manufacturing Techniques. *2019 13th European Conference on Antennas and Propagation (EuCAP)*, 2019.

[45] Cheng Guo, Jin Li, Yang Yu, Fan Zhang, Sheng Li, Moataz M. Attallah, Xiaobang Shang, Anxue Zhang, Yi Wang, and Michael J. Lancaster. Shaping and Slotting High-Q Spherical Resonators for Suppression of Higher Order Modes. *IEEE MTT-S International Microwave Symposium Digest*, 2019-June: 1205–1208, 6 2019. ISSN 0149645X. doi: 10.1109/MWSYM.2019.8700752.

[46] Jose R. Montejo-Garai, Jorge A. Ruiz-Cruz, and Jesus M. Rebollar. Evaluation of Additive Manufacturing Techniques Applied to a Waveguide Mode

Transducer. *IEEE Transactions on Components, Packaging and Manufacturing Technology*, 10(5):887–894, 5 2020. ISSN 21563985. doi: 10.1109/TCPMT.2020.2982735.

[47] George C. Southworth. Principles and Applications of Waveguide Transmission. *Bell System Technical Journal*, 29(3):295–342, 1950. ISSN 15387305. doi: 10.1002/J.1538-7305.1950.TB02348.X.

[48] Yann Cailloce, Philippe Hourlay, Florent Lebrun, and Baptiste Palacin. Additive manufacturing of Ku band horn antennas for telecommunications space applications. *IET Conference Publications*, 2018(CP741), 2018. doi: 10.1049/CP.2018.0602.

[49] F. Tchoffo Talom and S. Turpault. Additive manufacturing for RF microwave devices: Design, performances and treatments improvement evaluations. *Proceedings of the 2017 19th International Conference on Electromagnetics in Advanced Applications, ICEAA 2017*, pages 1473–1476, 10 2017. doi: 10.1109/ICEAA.2017.8065560.

[50] Oscar A. Peverini, Mauro Lumia, Flaviana Calignano, Giuseppe Addamo, Massimo Lorusso, Elisa Paola Ambrosio, Diego Manfredi, and Giuseppe Virone. Selective laser melting manufacturing of microwave waveguide devices. *Proceedings of the IEEE*, 105(4):620–631, 2017. ISSN 15582256. doi: 10.1109/JPROC.2016.2620148.

[51] G Addamo, O A Peverini, F Paonessa, G Virone, F Calignano, and D Manfredi. Additive Manufacturing of K/Ka/Q/V-Band Feed-Horns; Additive Manufacturing of K/Ka/Q/V-Band Feed-Horns. 2019.

[52] M Hollenbeck, K Wamick, C Cathey, J Opra, and R Smith. Selective Laser Melting aluminum waveguide attenuation at K-band. In *2017 IEEE MTT-S*

International Microwave Symposium (IMS), pages 45–47, 6 2017. doi: 10.1109/MWSYM.2017.8058605.

[53] Nicholas Clark, Samuel Hefford, and Adrian Porch. Effect of build orientation and surface finish on surface resistance in microwave components produced by Selective Laser Melting. *European Microwave Week 2017: "A Prime Year for a Prime Event", EuMW 2017 - Conference Proceedings; 47th European Microwave Conference, EuMC 2017*, 2017-January:508–511, 12 2017. doi: 10.23919/EUMC.2017.8230901.

[54] G Addamo, O A Peverini, M Lumia, G Virone, R Tascone, F Calignano, and D Manfredi. Experimental research activity on additive manufacturing of microwave passive waveguide components. In *2017 47th European Microwave Conference (EuMC)*, pages 496–499, 10 2017. doi: 10.23919/EuMC.2017.8230898.

[55] Samuel Hefford, Nicholas Clark, Richard Gumbleton, and Adrian Porch. Liftoff Dielectric Resonator for the Microwave Surface Resistance Measurement of Metal Plates. *IEEE Transactions on Instrumentation and Measurement*, 70, 2021. ISSN 15579662. doi: 10.1109/TIM.2020.3040834.

[56] Richard Gumbleton, Robert Batson, Kenneth Nai, and Adrian Porch. Effect of Build Orientation and Laser Power on Microwave Loss in Metal Additive Manufactured Components. *IEEE Access*, 9:44514–44520, 2021. ISSN 21693536. doi: 10.1109/ACCESS.2021.3067306.

[57] Na Li and Fei Zheng. Effect of micro/nano-scale rough surface on the quality factor of the filter: Model and simulation. *2010 IEEE International Conference on Mechatronics and Automation, ICMA 2010*, pages 1744–1748, 2010. doi: 10.1109/ICMA.2010.5588739.

[58] Samuel P. Morgan. Effect of Surface Roughness on Eddy Cur-

rent Losses at Microwave Frequencies. *Journal of Applied Physics*, 20(4):352–362, 4 1949. ISSN 0021-8979. doi: 10.1063/1.1698368. URL https://pubs.aip.org/aip/jap/article/20/4/352/159367/Effect-of-Surface-Roughness-on-Eddy-Current-Losses.

[59] Milan V. Lukić and Dejan S. Filipovic. Modeling of 3-D surface roughness effects with application to μ-coaxial lines. *IEEE Transactions on Microwave Theory and Techniques*, 55(3):518–525, 3 2007. ISSN 00189480. doi: 10.1109/TMTT.2007.891688.

[60] Christopher L. Holloway and Edward F. Kuester. Power loss associated with conducting and superconducting rough interfaces. *IEEE Transactions on Microwave Theory and Techniques*, 48(10):1601–1610, 10 2000. ISSN 00189480. doi: 10.1109/22.873886.

[61] Leung Tsang, Xiaoxiong Gu, and Henning Braunisch. Effects of random rough surface on absorption by conductors at microwave frequencies. *IEEE Microwave and Wireless Components Letters*, 16(4):221–223, 4 2006. ISSN 15311309. doi: 10.1109/LMWC.2006.872109.

[62] Konstantin Lomakin, Gerald Gold, and Klaus Helmreich. Analytical Waveguide Model Precisely Predicting Loss and Delay Including Surface Roughness. *IEEE TRANSACTIONS ON MICROWAVE THEORY AND TECHNIQUES*, 66(6), 2018. doi: 10.1109/TMTT.2018.2827383. URL http://www.ieee.org/publications_standards/publications/rights/index.html.

[63] C. R. Garcia, R. C. Rumpf, H. H. Tsang, and J. H. Barton. Effects of extreme surface roughness on 3D printed horn antenna. *Electronics Letters*, 49(12):734–736, 6 2013. ISSN 1350-911X. doi: 10.1049/EL.2013.1528. URL https://onlinelibrary.wiley.com/doi/full/10.1049/el.2013.1528https:

//onlinelibrary.wiley.com/doi/abs/10.1049/el.2013.1528https://ietresearch.onlinelibrary.wiley.com/doi/10.1049/el.2013.1528.

[64] Ming Ye, Lu Wang, Simeng Gao, Shiquan Fan, and Yongning He. Microwave surface resistance/resistivity measurement using microstrip complementary split ring resonator sensor. *2018 IEEE MTT-S International Wireless Symposium, IWS 2018 - Proceedings*, pages 1–3, 6 2018. doi: 10.1109/IEEE-IWS.2018.8400951.

[65] Jerzy Krupka and Janina Mazierska. Improvement of accuracy in measurements of the surface resistance of superconductors using dielectric resonators. *IEEE Transactions on Applied Superconductivity*, 8(4):164–167, 1998. ISSN 10518223. doi: 10.1109/77.740681.

[66] E. Hammerstad and O. Jensen. ACCURATE MODELS FOR MICROSTRIP COMPUTER-AIDED DESIGN. *IEEE MTT-S International Microwave Symposium Digest*, pages 107–409, 1980. ISSN 0149645X. doi: 10.1109/MWSYM.1980.1124303.

[67] Nicholas Clark. Microwave methods for additive layer manufacturing. 2017.

[68] RF Module - COMSOL 5.1 Release Highlights. URL https://www.comsol.com/release/5.1/rf-module.

[69] A. Hernandez, E. Martin, J. Margineda, and J. M. Zamarro. Resonant cavities for measuring the surface resistance of metals at X-band frequencies. *Journal of Physics E: Scientific Instruments*, 19(3):222, 3 1986. ISSN 0022-3735. doi: 10.1088/0022-3735/19/3/013. URL https://iopscience.iop.org/article/10.1088/0022-3735/19/3/013https://iopscience.iop.org/article/10.1088/0022-3735/19/3/013/meta.

[70] Howard E. Bussey. Standards and Measurements of Microwave Surface Impedance, Skin Depth, Conductivity and Q. *IRE Transactions on Instru-*

mentation, I-9(2):171–175, 1960. ISSN 21681902. doi: 10.1109/IRE-I.1960.5006910.

[71] V. Jerzy Krupka, Martin Klinger, Matthias Kuhn, Andreas Baranyak, Michael Stiller, Johann Hinken, and Józef Modelski. Surface Resistance Measurements of HTS Films by Means of Sapphire Dielectric Resonators. *IEEE Transactions on Applied Superconductivity*, 3(3):3043–3048, 1993. ISSN 15582515. doi: 10.1109/77.234839.

[72] Bi Zhang, P. Fabbricatore, G. Gemme, R. Musenich, and R. Parodi. A surface resistance measurement method for flat superconducting samples with a dielectric resonator structure. *Physica C: Superconductivity*, 235-240(PART 5): 3375–3376, 12 1994. ISSN 0921-4534. doi: 10.1016/0921-4534(94)91214-9.

[73] Janina Mazierska. Dielectric resonator as a possible standard for characterization of high temperature superconducting films for microwave applications. *Journal of Superconductivity*, 10(2):73–84, 1997. ISSN 08961107. doi: 10.1007/BF02763176/METRICS. URL `https://link.springer.com/article/10.1007/BF02763176`.

[74] Andrei P. Mourachkine and Alain R.F. Barel. Microwave Measurement of Surface Resistance by the Parallel-Plate Dielectric Resonator Method. *IEEE Transactions on Microwave Theory and Techniques*, 43(3):544–551, 1995. ISSN 15579670. doi: 10.1109/22.372099.

[75] Janina Mazierska and Charles Wilker. Accuracy issues in surface resistance measurements of high temperature superconductors using dielectric resonators (corrected). *IEEE Transactions on Applied Superconductivity*, 11(4):4140–4147, 12 2001. ISSN 10518223. doi: 10.1109/77.979858.

[76] Samuel John Hefford. Microwave Processing in Additive Manufacturing. 2019.

[77] H. F. Cook. The dielectric behaviour of some types of human tissues at microwave frequencies. *British Journal of Applied Physics*, 2(10):295, 10 1951. ISSN 0508-3443. doi: 10.1088/0508-3443/2/10/304. URL https://iopscience.iop.org/article/10.1088/0508-3443/2/10/304https://iopscience.iop.org/article/10.1088/0508-3443/2/10/304/meta.

[78] U. Raveendranath, S. Bijukumar, and K. T. Mathew. Broadband coaxial cavity resonator for complex permittivity measurements of liquids. *IEEE Transactions on Instrumentation and Measurement*, 49(6):1305–1312, 12 2000. ISSN 00189456. doi: 10.1109/19.893275.

[79] Seyed Hossein Mirjahanmardi and Omar Ramahi. Highly accurate liquid permittivity measurement using coaxial lines. *2019 IEEE International Symposium on Antennas and Propagation and USNC-URSI Radio Science Meeting, APSURSI 2019 - Proceedings*, pages 101–102, 7 2019. doi: 10.1109/APUSNCURSINRSM.2019.8888373.

[80] R. J. Sheppard and E. H. Grant. Design and construction of a coaxial line cell for measuring the complex permittivity of a liquid. *Journal of Physics E: Scientific Instruments*, 5(12):1208, 12 1972. ISSN 0022-3735. doi: 10.1088/0022-3735/5/12/023. URL https://iopscience.iop.org/article/10.1088/0022-3735/5/12/023https://iopscience.iop.org/article/10.1088/0022-3735/5/12/023/meta.

[81] Thierry Bore, Habibullah Bhuyan, Tilman Bittner, Alexander Scheuermann, and Norman Wagner. Electromagnetic Characterization of Coarse-Grained Soils with a One Port Large Coaxial Cell. *2018 12th International Conference on Electromagnetic Wave Interaction with Water and Moist Substances, ISEMA 2018*, 8 2018. doi: 10.1109/ISEMA.2018.8442281.

[82] Robert Tempke, Christina Wildfire, Dushyant Shekhawat, and Terence

Musho. Dielectric measurement of powdery materials using a coaxial transmission line. *IET Science, Measurement & Technology*, 14(10):972–978, 12 2020. ISSN 1751-8830. doi: 10.1049/IET-SMT.2020.0055. URL https://onlinelibrary.wiley.com/doi/full/10.1049/iet-smt.2020.0055https://onlinelibrary.wiley.com/doi/abs/10.1049/iet-smt.2020.0055https://ietresearch.onlinelibrary.wiley.com/doi/10.1049/iet-smt.2020.0055.

[83] Juan R. Mosig, Jean Claude E. Besson, Marianne Gex-Fabry, and Fred E. Gardiol. Reflection of an Open-Ended Coaxial Line and Application to Nondestructive Measurement of Materials. *IEEE Transactions on Instrumentation and Measurement*, IM-30(1):46–51, 1981. ISSN 15579662. doi: 10.1109/TIM.1981.6312437.

[84] Ali Farshkaran and Emily Porter. Coaxial Probe-based Measurements of Biological Tissues: Inaccuracies in Sensing Volume when Calculated from Sensing Radius and Sensing Depth. *2021 International Conference on Electromagnetics in Advanced Applications, ICEAA 2021*, pages 110–113, 8 2021. doi: 10.1109/ICEAA52647.2021.9539727.

[85] J. S. Bobowski and T. Johnson. Permittivity measurements of biological samples by an open-ended coaxial line. *Progress In Electromagnetics Research B*, (40):159–183, 2012. ISSN 19376472. doi: 10.2528/PIERB12022906.

[86] Udo Kaatze and Yuri Feldman. Broadband dielectric spectrometry of liquids and biosystems. *Measurement Science and Technology*, 17(2):R17, 12 2005. ISSN 0957-0233. doi: 10.1088/0957-0233/17/2/R01. URL https://iopscience.iop.org/article/10.1088/0957-0233/17/2/R01https://iopscience.iop.org/article/10.1088/0957-0233/17/2/R01/meta.

[87] R. Olmi, M. Bini, A. Ignesti, and C. Riminesi. Non-destructive permittivity

measurement of solid

}materials. *Measurement Science and Technology*, 11(11):1623, 11 2000. ISSN 0957-0233. doi: 10.1088/0957-0233/11/11/312.

[88] Paul D. Domich, Michael D. Janezic, and Richard G. Geyer. Analysis of an Open-Ended Coaxial Probe with Lift-Off for Nondestructive Testing. *IEEE Transactions on Instrumentation and Measurement*, 43(5):711–718, 1994. ISSN 15579662. doi: 10.1109/19.328897.

[89] The accurate measurement of permittivity by means of an open resonator. *Proceedings of the Royal Society of London. A. Mathematical and Physical Sciences*, 325(1563):493–509, 12 1971. ISSN 0080-4630. doi: 10.1098/RSPA.1971.0181. URL `https://royalsocietypublishing.org/doi/10.1098/rspa.1971.0181`.

[90] Tomasz Karpisz and Bartlomiej Salski. Measurement of Dielectrics From 20 to 50 GHz With a Fabry – Pérot Open Resonator. *IEEE Transactions on Microwave Theory and Techniques*, 67(5):1901–1908, 2019. doi: 10.1109/TMTT.2019.2905549.

[91] Taavi M. Hirvoncn, Pcrtti Vainikainen, Andrzej Lozowski, and Antti V. Räisänen. Measurement of dielectrics at 100 GHz with an open resonator connected to a network analyzer. *IEEE Transactions on Instrumentation and Measurement*, 45(4):780–786, 1996. ISSN 00189456. doi: 10.1109/19.516996.

[92] Piotr Czekala, Bartlomiej Salski, Pawel Kopyt, Malgorzata Warecka, Sebastian Dziedziewicz, Rafal Lech, and Piotr Kowalczyk. Beam Waist in a Plano-Concave Fabry-Perot Open Resonator. *2022 24th International Microwave and Radar Conference, MIKON 2022*, 2022. doi: 10.23919/MIKON54314.2022.9924949.

[93] Rezwanur Rahman, Douglas K. McCarty, and Manika Prasad. Sub-THz

complex dielectric constants of smectite clay thin samples with Na+/Ca++ ions. *Journal of Geophysical Research: Solid Earth*, 120(9):6219–6225, 9 2015. ISSN 2169-9356. doi: 10.1002/2015JB011956. URL `https://onlinelibrary.wiley.com/doi/full/10.1002/2015JB011956https://onlinelibrary.wiley.com/doi/abs/10.1002/2015JB011956https://agupubs.onlinelibrary.wiley.com/doi/10.1002/2015JB011956`.

[94] Zhengrong Tian and Charles Free. Measurement techniques for the evaluation of thick-film materials used in wireless applications. *Microelectronics International*, 18(2):21–25, 5 2001. ISSN 13565362. doi: 10.1108/13565360110391600/FULL/PDF.

[95] S. Pullteap, H. C. Seat, and T. Bosch. Temperature and distance-dependent errors in a dual-cavity fibre Fabry-Perot interferometer for vibration analysis. *Conference Record - IEEE Instrumentation and Measurement Technology Conference*, 2007. ISSN 10915281. doi: 10.1109/IMTC.2007.379296.

[96] W. Culshaw. Reflectors for a Microwave Fabry-Perot Interferometer. *IRE Transactions on Microwave Theory and Techniques*, 7(2):221–228, 1959. ISSN 00972002. doi: 10.1109/TMTT.1959.1124685.

[97] Nan Jiang, Sergey Flyax, Wolfgang Kurz, Martin Jakobi, Savas Tasoglu, Alexander W. Koch, and Ali K. Yetisen. Intracranial Sensors for Continuous Monitoring of Neurophysiology. *Advanced Materials Technologies*, 6 (12):2100339, 12 2021. ISSN 2365-709X. doi: 10.1002/ADMT.202100339. URL `https://onlinelibrary.wiley.com/doi/full/10.1002/admt.202100339https://onlinelibrary.wiley.com/doi/abs/10.1002/admt.202100339https://onlinelibrary.wiley.com/doi/10.1002/admt.202100339`.

[98] Renishaw. AlSi10Mg-0403 powder for additive manufacturing. Technical report, 2015.

[99] John Dunkley Dr. Advances in atomisation techniques for the formation of metal powders. *Advances in Powder Metallurgy: Properties, Processing and Applications*, pages 3–18, 1 2013. doi: 10.1533/9780857098900.1.3.

[100] Timothée Delacroix, Fernando Lomello, Frédéric Schuster, Hicham Maskrot, and Jean Paul Garandet. Influence of powder recycling on 316L stainless steel feedstocks and printed parts in laser powder bed fusion. *Additive Manufacturing*, 50:102553, 2 2022. ISSN 2214-8604. doi: 10.1016/J.ADDMA.2021.102553.

[101] W. Liu, Z. Chen, T. Viola, and G. H. Huff. 3-D Printed Directional Couplers in Circular Waveguide. *IEEE Microwave and Wireless Components Letters*, 31(6):561–564, 6 2021. ISSN 15581764. doi: 10.1109/LMWC.2021.3070745.

[102] Ziren Wang, Jinchun Gao, Yilin Zhou, and Zhongyang Cheng. High-Frequency Behavior Analysis and Modeling of Silver Plated Printed Circuit Board with Electrochemical Migration. *Journal of Electronic Materials*, 48(12):8039–8046, 12 2019. ISSN 1543186X. doi: 10.1007/S11664-019-07651-3/METRICS. URL `https://link.springer.com/article/10.1007/s11664-019-07651-3`.

[103] A. Yli-Pentti. Electroplating and Electroless Plating. *Comprehensive Materials Processing*, 4:277–306, 1 2014. doi: 10.1016/B978-0-08-096532-1.00413-1.

[104] T. Asher, A. Inberg, E. Glickman, N. Fishelson, and Y. Shacham-Diamand. Formation and characterization of low resistivity sub-100 nm copper films deposited by electroless on SAM. *Electrochimica Acta*, 54(25):6053–6057, 10 2009. ISSN 0013-4686. doi: 10.1016/J.ELECTACTA.2009.02.089.

[105] Sung Te Chen, Yu Cheng Chung, Jau Shiung Fang, Yi Lung Cheng, and Giin Shan Chen. Enhancement of seeding for electroless Cu plating of metallic barrier layers by using alkyl self-assembled monolayers. *Applied Surface*

Science, 405:350–358, 5 2017. ISSN 0169-4332. doi: 10.1016/J.APSUSC.2017.02.027.

[106] Derek King, John Middendorf, Kathleen Cissel, Thomas Key, and Carmen Carney. Selective laser melting for the preparation of an ultra-high temperature ceramic coating. *Ceramics International*, 45(2):2466–2473, 2 2019. ISSN 0272-8842. doi: 10.1016/J.CERAMINT.2018.10.173.

[107] Gi Dae Kim and Byoung Gook Loh. Characteristics of chip formation in micro V-grooving using elliptical vibration cutting. *Journal of Micromechanics and Microengineering*, 17(8):1458, 6 2007. ISSN 0960-1317. doi: 10.1088/0960-1317/17/8/007. URL `https://iopscience.iop.org/article/10.1088/0960-1317/17/8/007https://iopscience.iop.org/article/10.1088/0960-1317/17/8/007/meta`.

[108] N. Ramachandran, S. S. Pande, and N. Ramakrishnan. The role of deburring in manufacturing: A state-of-the-art survey. *Journal of Materials Processing Technology*, 44(1-2):1–13, 7 1994. ISSN 0924-0136. doi: 10.1016/0924-0136(94)90033-7.

[109] Sung Lim Ko and David A. Dornfeld. A Study on Burr Formation Mechanism. *Journal of Engineering Materials and Technology*, 113(1):75–87, 1 1991. ISSN 0094-4289. doi: 10.1115/1.2903385. URL `https://asmedigitalcollection.asme.org/materialstechnology/article/113/1/75/402588/A-Study-on-Burr-Formation-Mechanism`.

[110] Seyed Ali Niknam and Victor Songmene. Deburring and edge finishing of aluminum alloys : a review.

[111] Hongyu Li, David Walker, Xiao Zheng, Guoyu Yu, Christina Reynolds, al Hongyu Li, Wang Zhang, and Tony Li. Advanced techniques for robotic polishing of aluminum mirrors. *https://doi.org/10.1117/12.2311625*,

10692(15):152–163, 6 2018. ISSN 1996756X. doi: 10.1117/12.2311625. URL https://www.spiedigitallibrary.org/conference-proceedings-of-spie/10692/106920N/Advanced-techniques-for-robotic-polishing-of-aluminum-mirrors/10.1117/12.2311625.fullhttps://www.spiedigitallibrary.org/conference-proceedings-of-spie/10692/106920N/Advanced-techniques-for-robotic-polishing-of-aluminum-mirrors/10.1117/12.2311625.short.

[112] W Morton, S Green, A Rennie, and T Abram. Surface finishing techniques for SLM manufactured stainless steel 316L components. In *Innovative Developments in Virtual and Physical Prototyping*, pages 503–509. CRC Press, 9 2011. doi: 10.1201/b11341-82.

[113] M. Kahlin, H. Ansell, D. Basu, A. Kerwin, L. Newton, B. Smith, and J.J. Moverare. Improved fatigue strength of additively manufactured Ti6Al4V by surface post processing. *International Journal of Fatigue*, 134:105497, 5 2020. ISSN 01421123. doi: 10.1016/j.ijfatigue.2020.105497.

[114] D. Pozar. *Microwave Engineering Fourth Edition*. 2005. ISBN 9780470631553. doi: TK7876.P692011.

[115] J. P. Del Risco and J. D. Baena. Extremely thin Fabry-Perot resonators based on high permitivity artificial dielectric. *2016 10th International Congress on Advanced Electromagnetic Materials in Microwaves and Optics, METAMATERIALS 2016*, pages 40–42, 11 2016. doi: 10.1109/METAMATERIALS.2016.7746420.

[116] P. K. Yu and Alexander Lamb Cullen. Measurement of permittivity by means of an open resonator. I. Theoretical. *Proceedings of the Royal Society of Lon-*

don. A. Mathematical and Physical Sciences, 380(1778):49–71, 3 1982. ISSN 0080-4630. doi: 10.1098/rspa.1982.0029.

[117] Minoru Sanagi, Toshihide Itoga, and Shigeji Nogi. Axially symmetrical Fabry-Perot oscillator with multiple devices inserted in dielectric substrate. *Asia-Pacific Microwave Conference Proceedings, APMC*, 1:337–340, 1997. doi: 10.1109/APMC.1997.659372.

[118] Bartlomiej Salski, Marzena Olszewska-Placha, Pawel Kopyt, and Mateusz Krysicki. Loss tangent uncertainty in resonant microwave characterization of dielectric materials. *2022 24th International Microwave and Radar Conference, MIKON 2022*, 2022. doi: 10.23919/MIKON54314.2022.9924845.

[119] Petr Piksa, Stanislav Zvanovec, Petr Cerny, and Milos Mazanek. Full-wave modeling of Fabry-Perot resonator in millimeter waves. *Proceedings of the 14th Conference on Microwave Techniques, COMITE 2008*, 2008. doi: 10.1109/COMITE.2008.4569927.

[120] Gaussian beams, explained by RP; laser beam, fundamental transverse modes, propagation. URL `https://www.rp-photonics.com/gaussian_beams.html`.

[121] Benjamin B. Yang, Sarah L. Katz, Keely J. Willis, Marcus J. Weber, Irena Knezevic, Susan C. Hagness, and John H. Booske. A high-Q terahertz resonator for the measurement of electronic properties of conductors and low-loss dielectrics. *IEEE Transactions on Terahertz Science and Technology*, 2(4):449–459, 2012. ISSN 2156342X. doi: 10.1109/TTHZ.2012.2199578.

[122] R. Faraji-Dana and Y. Chow. Edge condition of the field and A.C. resistance of a rectangular strip conductor. *IEE Proceedings H: Microwaves, Antennas and Propagation*, 137(2):133–140, 1990. ISSN 0950107X. doi: 10.1049/IP-H-2.1990.0025/CITE/REFWORKS.

[123] G. Appa Rao, Mahendra Kumar, M. Srinivas, and D. S. Sarma. Effect of standard heat treatment on the microstructure and mechanical properties of hot isostatically pressed superalloy inconel 718. *Materials Science and Engineering: A*, 355(1-2):114–125, 8 2003. ISSN 09215093. doi: 10.1016/S0921-5093(03)00079-0.

[124] M. Dietze, H. P. Buchkremer, and D. Stöver. Densification behaviour of a PM titanium alloy during HIP. *Metal Powder Report*, 46(10):30–35, 10 1991. ISSN 0026-0657. doi: 10.1016/0026-0657(91)90974-6.

[125] Laura Cordova, Ton Bor, Marc de Smit, Simone Carmignato, Mónica Campos, and Tiedo Tinga. Effects of powder reuse on the microstructure and mechanical behaviour of Al–Mg–Sc–Zr alloy processed by laser powder bed fusion (LPBF). *Additive Manufacturing*, 36:101625, 12 2020. ISSN 2214-8604. doi: 10.1016/J.ADDMA.2020.101625.

[126] A. du Plessis and E. Macdonald. Hot isostatic pressing in metal additive manufacturing: X-ray tomography reveals details of pore closure. *Additive Manufacturing*, 34:101191, 8 2020. ISSN 2214-8604. doi: 10.1016/J.ADDMA.2020.101191.

[127] Livia Zumofen, Andreas Kirchheim, and Hans Jörg Dennig. Laser powder bed fusion of 30CrNiMo8 steel for quenching and tempering: examination of the processability and mechanical properties. *Progress in Additive Manufacturing*, 5(1):75–81, 3 2020. ISSN 23639520. doi: 10.1007/S40964-020-00121-X/FIGURES/6. URL `https://link.springer.com/article/10.1007/s40964-020-00121-x`.

[128] Honglei Zhen, Bin Zhao, Long Quan, and Junyu Fu. Effect of 3D Printing Process Parameters and Heat Treatment Conditions on the Mechanical Properties and Microstructure of PEEK Parts. *Polymers 2023, Vol.*

15, Page 2209, 15(9):2209, 5 2023. ISSN 2073-4360. doi: 10.3390/POLYM15092209. URL https://www.mdpi.com/2073-4360/15/9/2209/htmhttps://www.mdpi.com/2073-4360/15/9/2209.

[129] J. Kennedy, P. P. Murmu, J. Leveneur, A. Markwitz, and J. Futter. Controlling preferred orientation and electrical conductivity of zinc oxide thin films by post growth annealing treatment. *Applied Surface Science*, 367:52–58, 3 2016. ISSN 0169-4332. doi: 10.1016/J.APSUSC.2016.01.160.

[130] Qing Ye Jin, Dongseok Kang, Kyungsik Ha, Jea Hyun Yu, and Wookjin Lee. Simulation of annealing process on AISI 316 L stainless steel fabricated via laser powder bed fusion using finite element method with creep. *Additive Manufacturing*, 60:103255, 12 2022. ISSN 2214-8604. doi: 10.1016/J.ADDMA.2022.103255.

[131] Bandar AlMangour and Jenn Ming Yang. Improving the surface quality and mechanical properties by shot-peening of 17-4 stainless steel fabricated by additive manufacturing. *Materials & Design*, 110:914–924, 11 2016. ISSN 0264-1275. doi: 10.1016/J.MATDES.2016.08.037.

[132] Lucia Denti and Antonella Sola. On the Effectiveness of Different Surface Finishing Techniques on A357.0 Parts Produced by Laser-Based Powder Bed Fusion: Surface Roughness and Fatigue Strength. *Metals 2019, Vol. 9, Page 1284*, 9(12):1284, 11 2019. ISSN 2075-4701. doi: 10.3390/MET9121284. URL https://www.mdpi.com/2075-4701/9/12/1284/htmhttps://www.mdpi.com/2075-4701/9/12/1284.

[133] Y. G. Liu, H. M. Li, and M. Q. Li. Characterization of surface layer in TC17 alloy treated by air blast shot peening. *Materials & Design (1980-2015)*, 65:120–126, 1 2015. ISSN 0261-3069. doi: 10.1016/J.MATDES.2014.09.019.

[134] Turgay Kivak. Optimization of surface roughness and flank wear using the

Taguchi method in milling of Hadfield steel with PVD and CVD coated inserts. *Measurement*, 50(1):19–28, 4 2014. ISSN 0263-2241. doi: 10.1016/J.MEASUREMENT.2013.12.017.

Appendix A

Appendix

A.1 Frequency response graph with respect to measured surface resistance

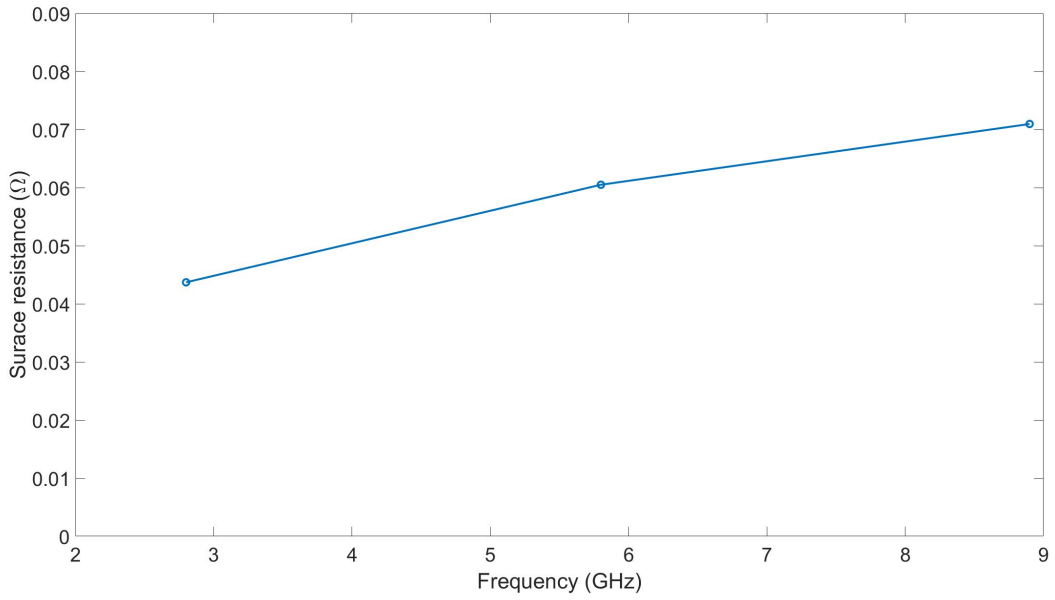

Figure A.1: As built samples frequency response of R_S when a vertical magnetic filed is applied for a vertically built part.

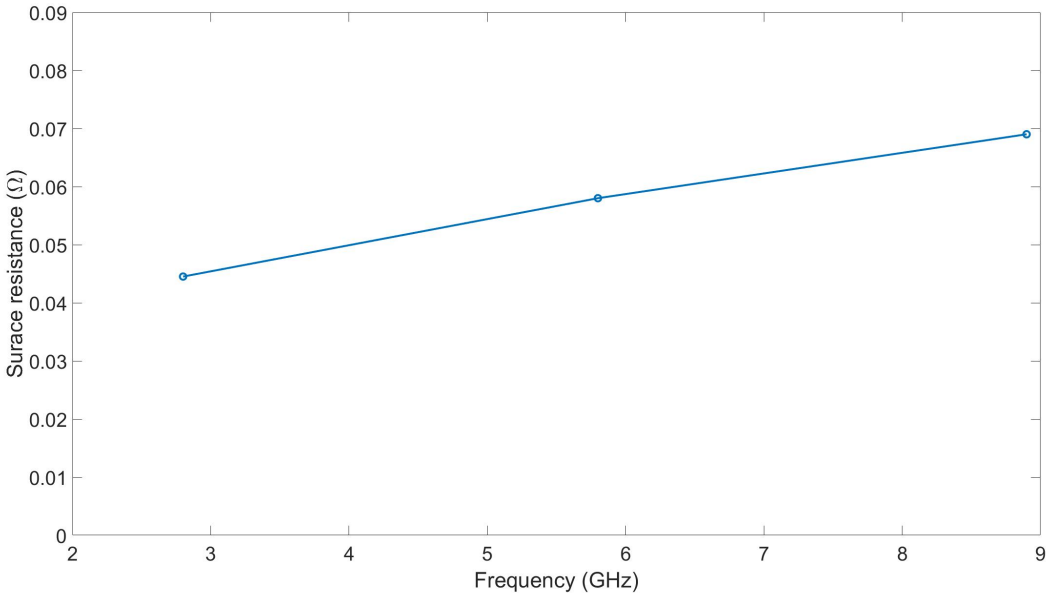

Figure A.2: As built samples frequency response of R_S when a horizontal magnetic filed is applied for a vertically built part.

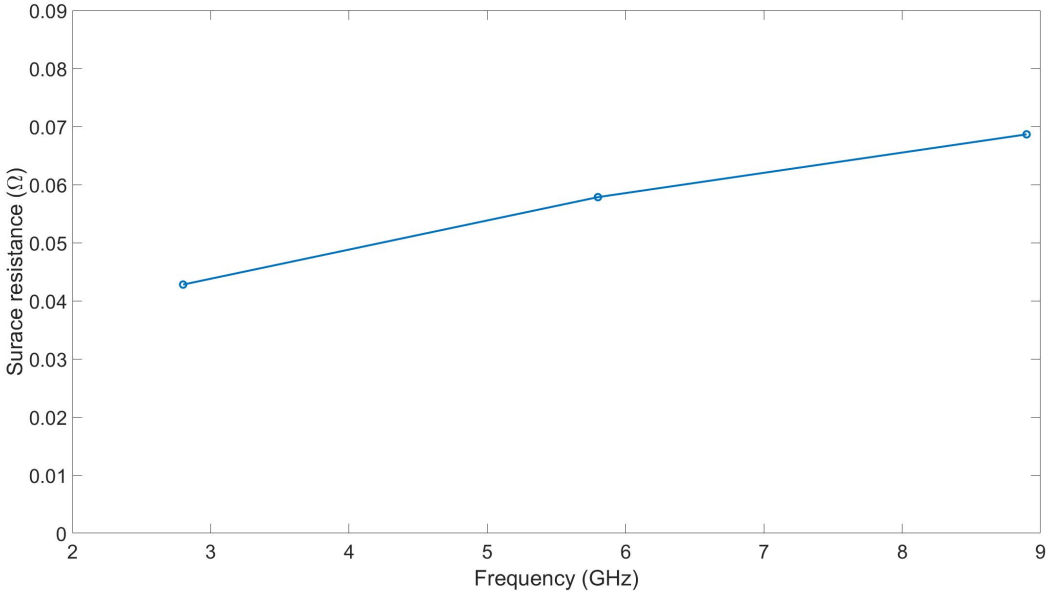

Figure A.3: As built samples frequency response of R_S when the magnetic filed is applied at a 45 degrees for a vertically built part.

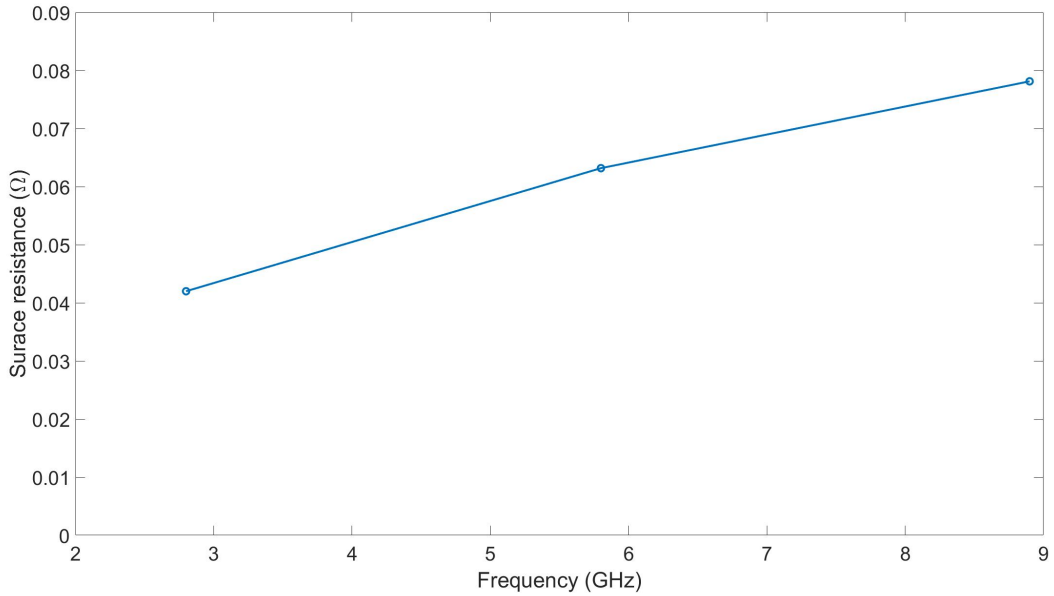

Figure A.4: As built samples frequency response of R_S when a vertical magnetic filed is applied for a horizontally built part.

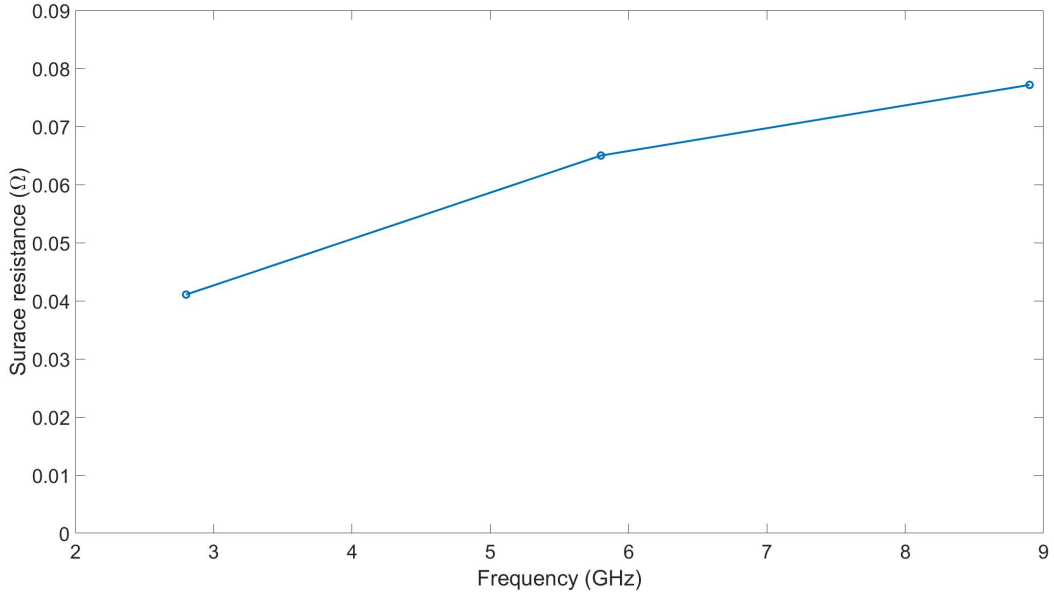

Figure A.5: As built samples frequency response of R_S when a horizontal magnetic filed is applied for a horizontally built part.

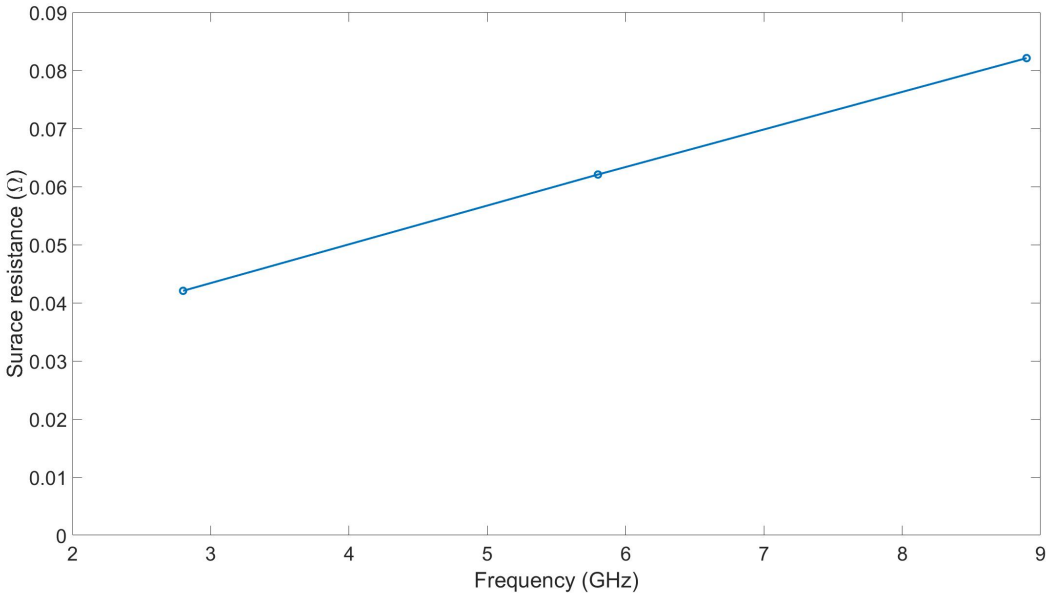

Figure A.6: As built samples frequency response of R_S when the magnetic filed is applied at a 45 degrees for a horizontally built part.

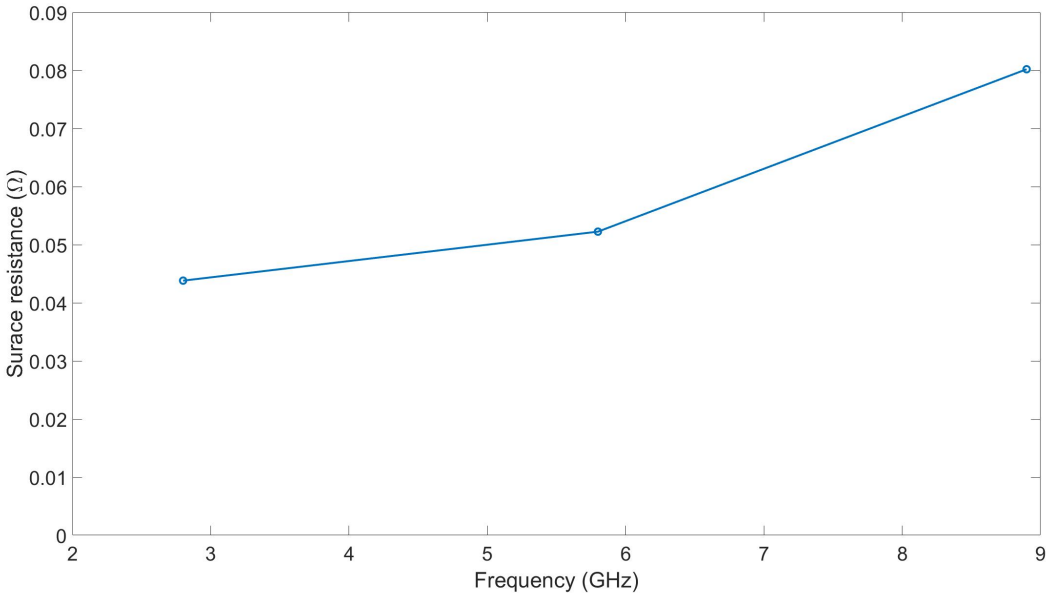

Figure A.7: As built samples frequency response of R_S when a vertical magnetic filed is applied for the 45 degrees built part upwards facing surface.

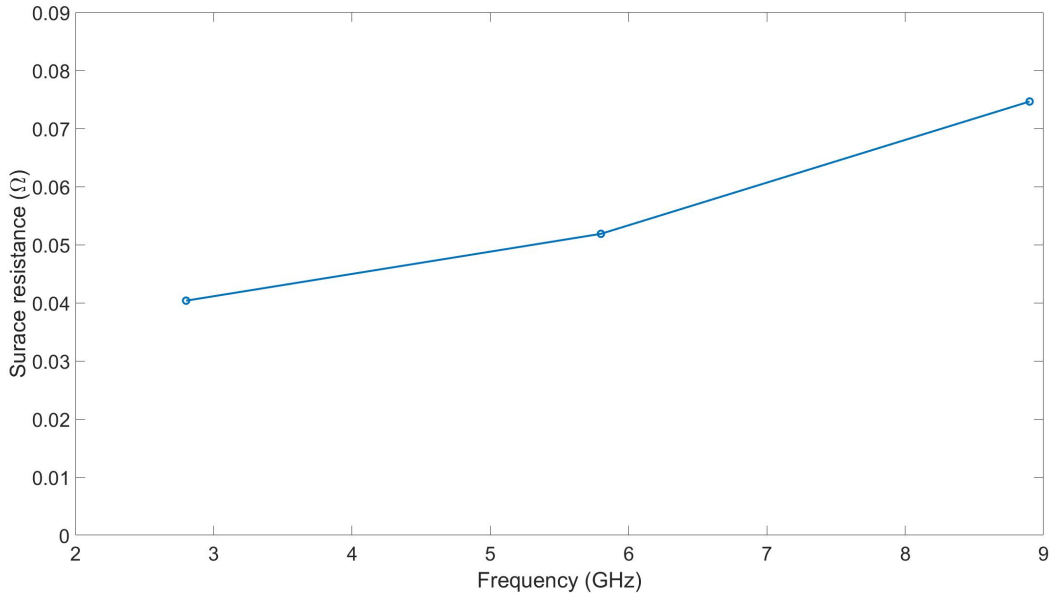

Figure A.8: As built samples frequency response of R_S when a horizontal magnetic filed is applied for the 45 degrees built part upwards facing surface.

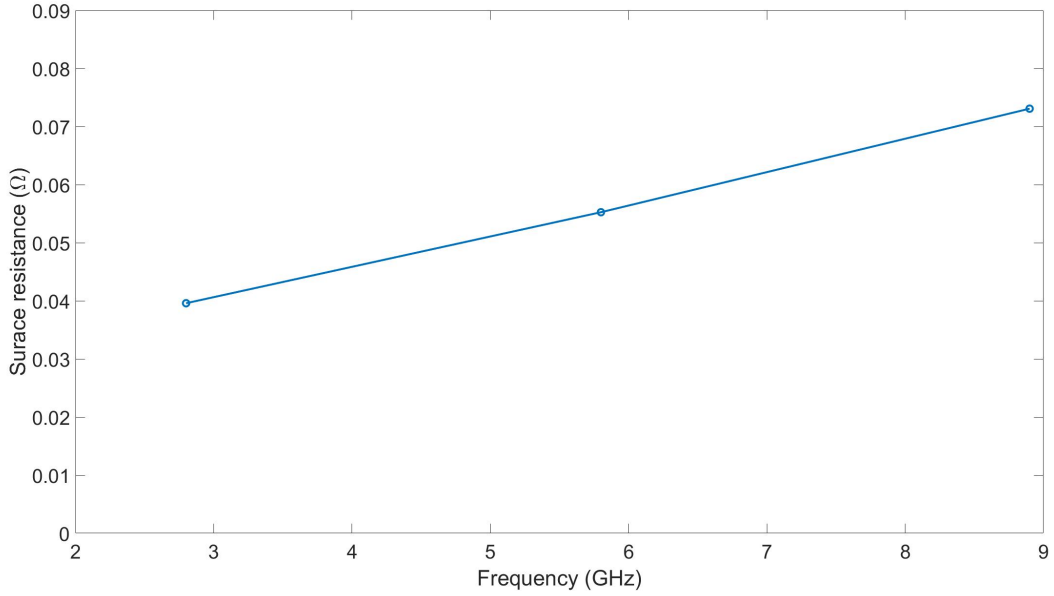

Figure A.9: As built samples frequency response of R_S when the magnetic filed is applied at a 45 degrees for the 45 degrees built part upwards facing surface.

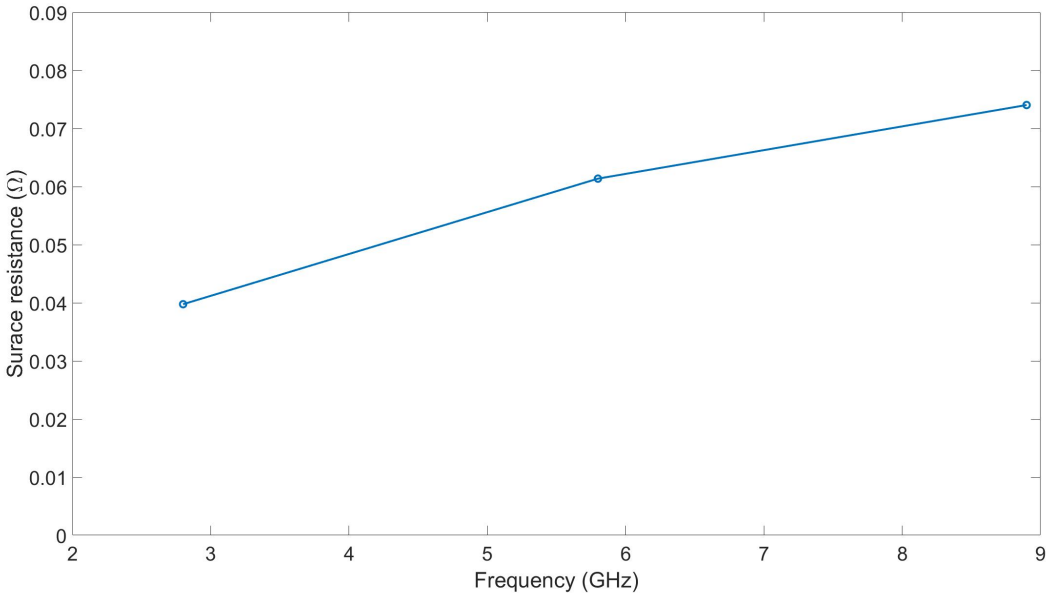

Figure A.10: As built samples frequency response of R_S when a vertical magnetic filed is applied for the 45 degrees built part downwards facing surface.

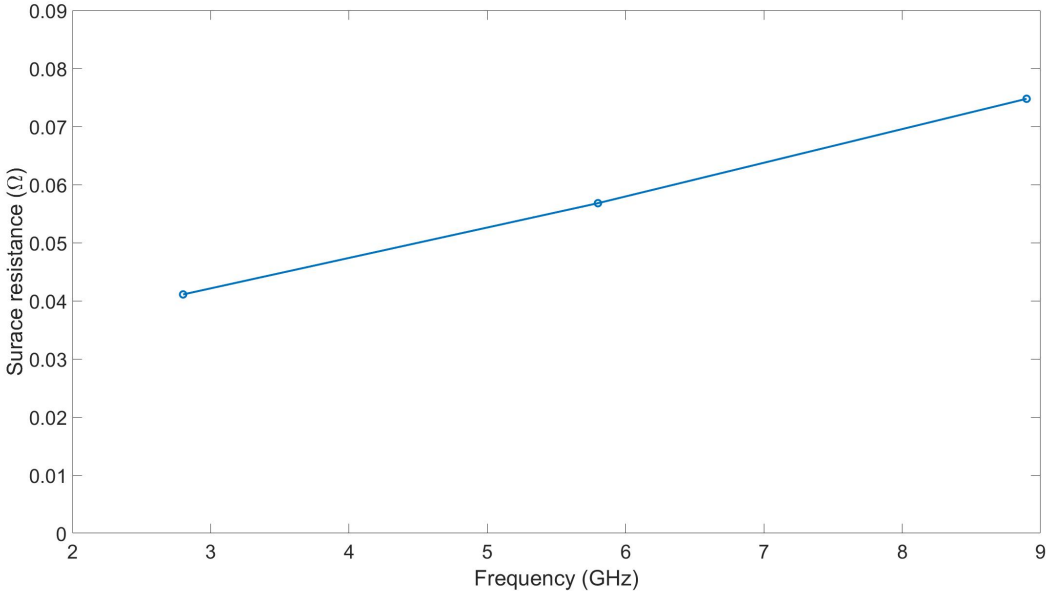

Figure A.11: As built samples frequency response of R_S when a horizontal magnetic filed is applied for the 45 degrees built part downwards facing surface.

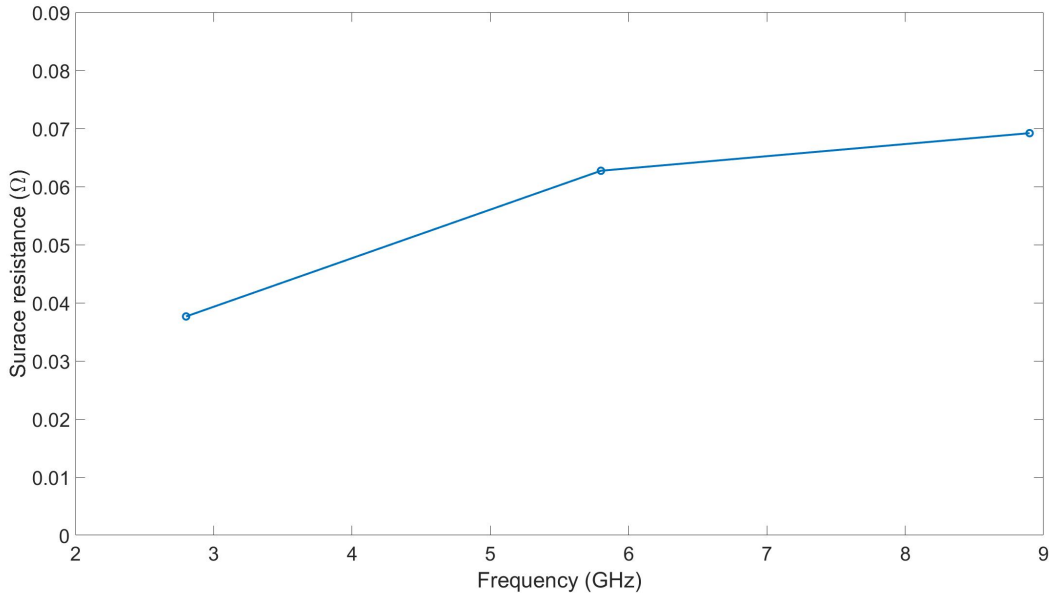

Figure A.12: As built samples frequency response of R_S when the magnetic filed is applied at a 45 degrees for the 45 degrees built part downwards facing surface.

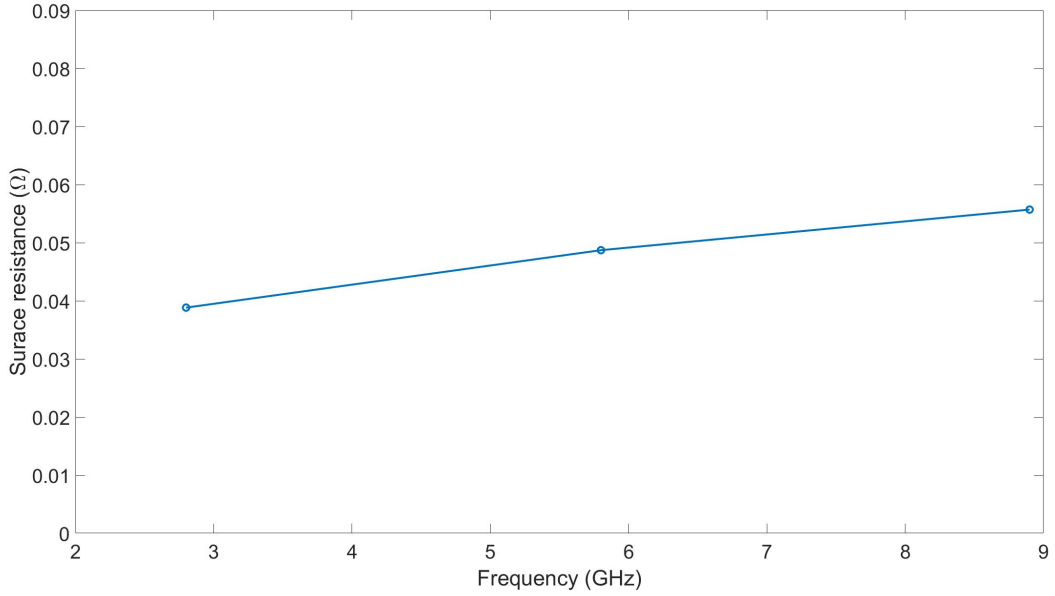

Figure A.13: Machined samples frequency response of R_S when a vertical magnetic filed is applied for a vertically built part.

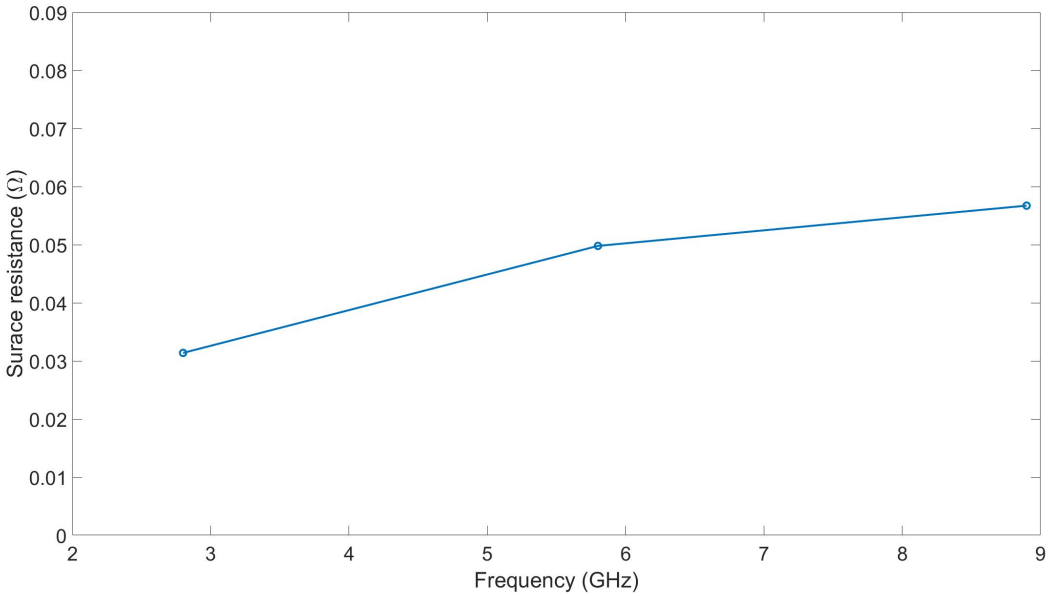

Figure A.14: Machined samples frequency response of R_S when a horizontal magnetic filed is applied for a vertically built part.

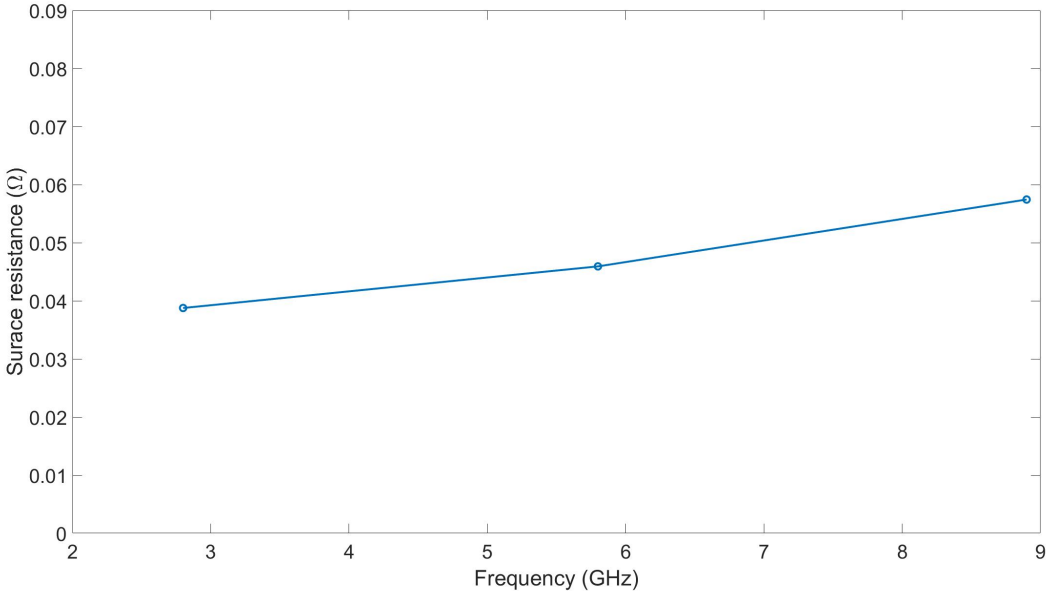

Figure A.15: Machined samples frequency response of R_S when the magnetic filed is applied at a 45 degrees for a vertically built part.

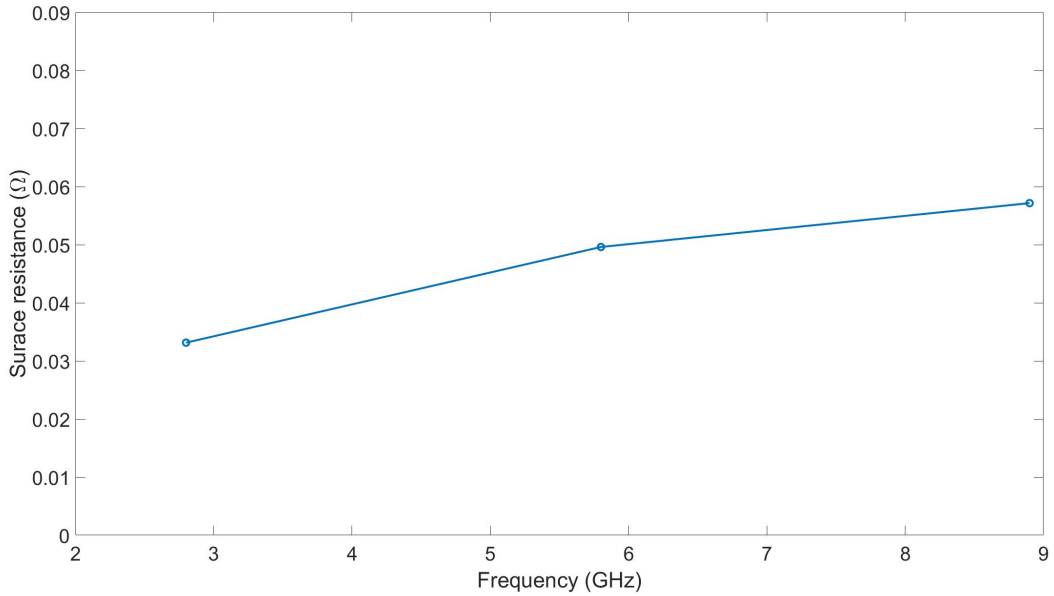

Figure A.16: Machined samples frequency response of R_S when a vertical magnetic filed is applied for a horizontally built part.

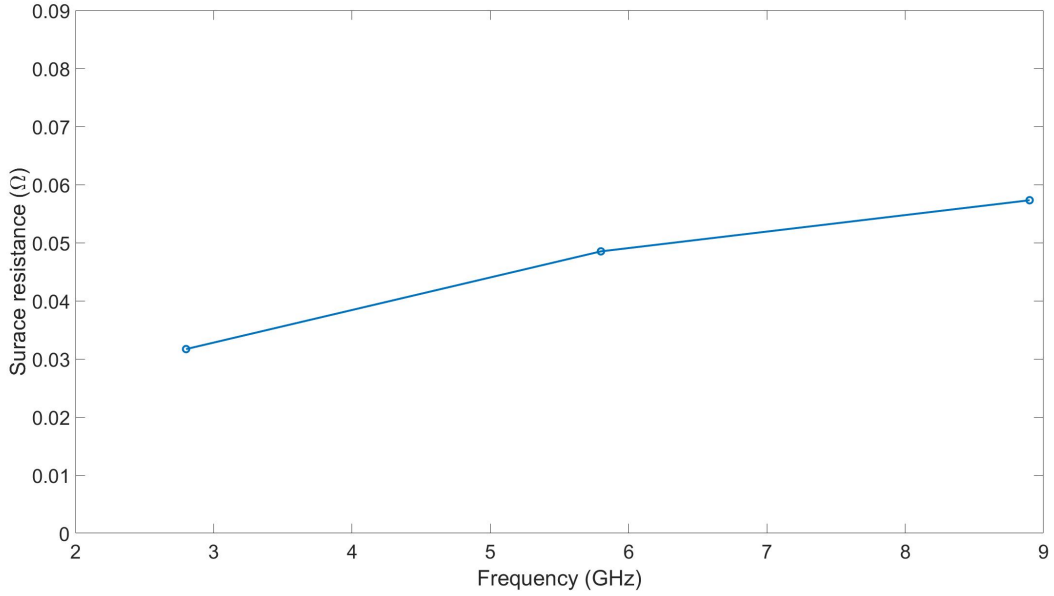

Figure A.17: Machined samples frequency response of R_S when a horizontal magnetic filed is applied for a horizontally built part.

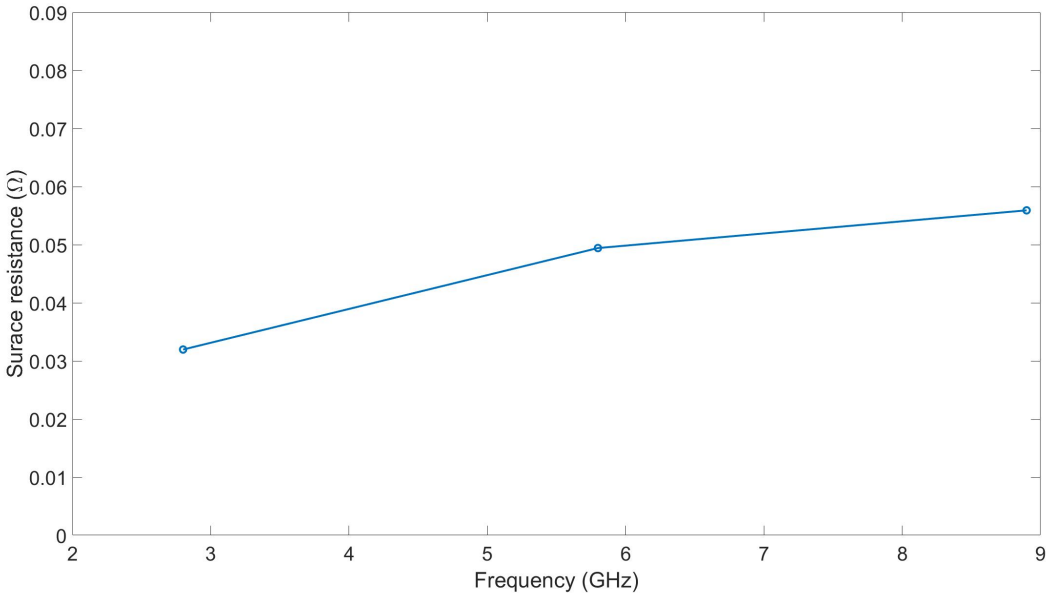

Figure A.18: Machined samples frequency response of R_S when the magnetic filed is applied at a 45 degrees for a horizontally built part.

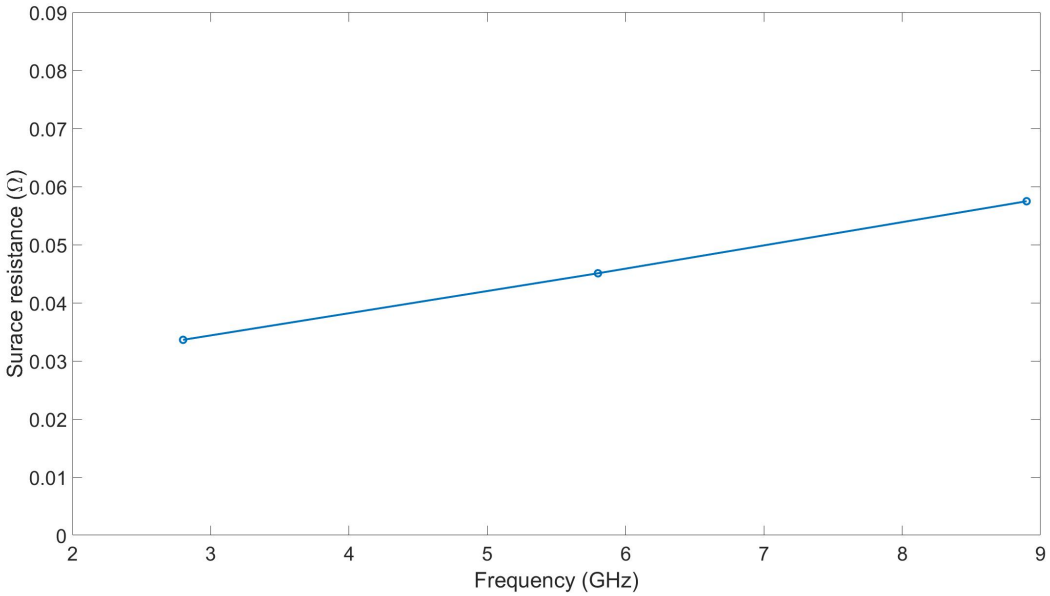

Figure A.19: Machined samples frequency response of R_S when a vertical magnetic filed is applied for the 45 degrees built part upwards facing surface.

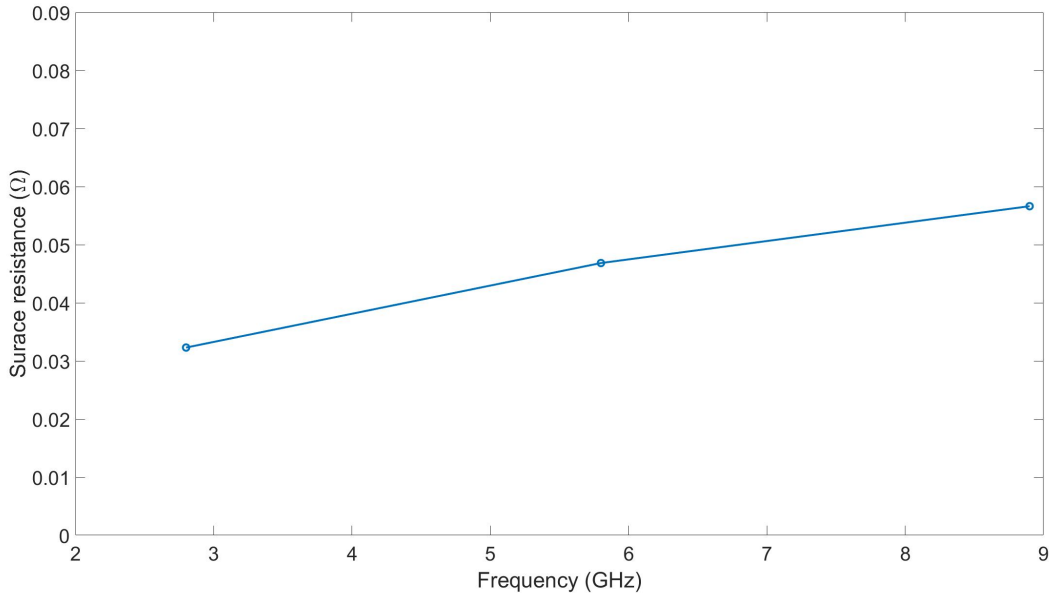

Figure A.20: Machined samples frequency response of R_S when a horizontal magnetic filed is applied for the 45 degrees built part upwards facing surface.

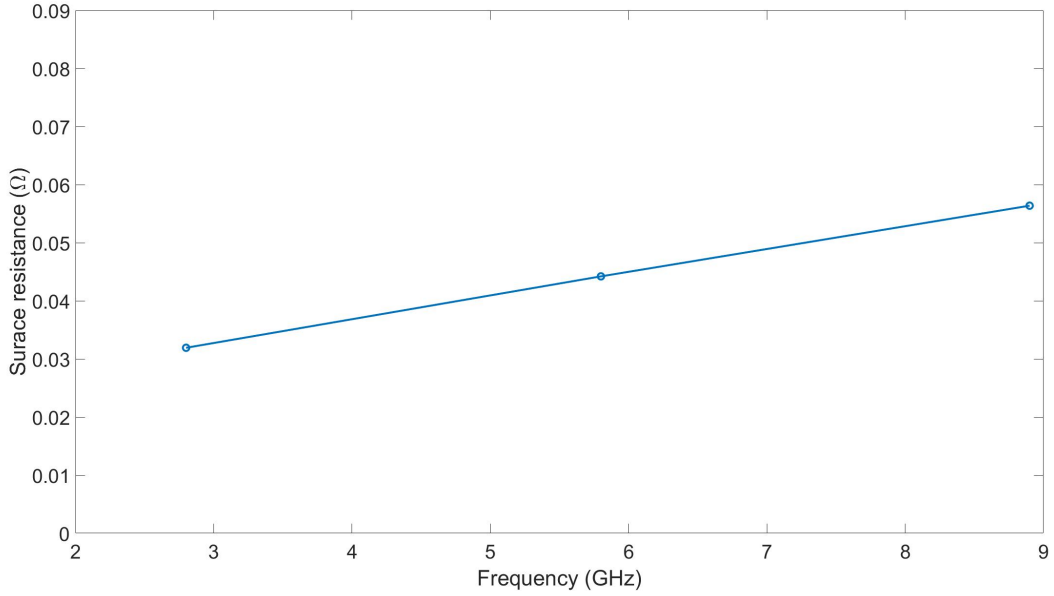

Figure A.21: Machined samples frequency response of R_S when the magnetic filed is applied at a 45 degrees for the 45 degrees built part upwards facing surface.

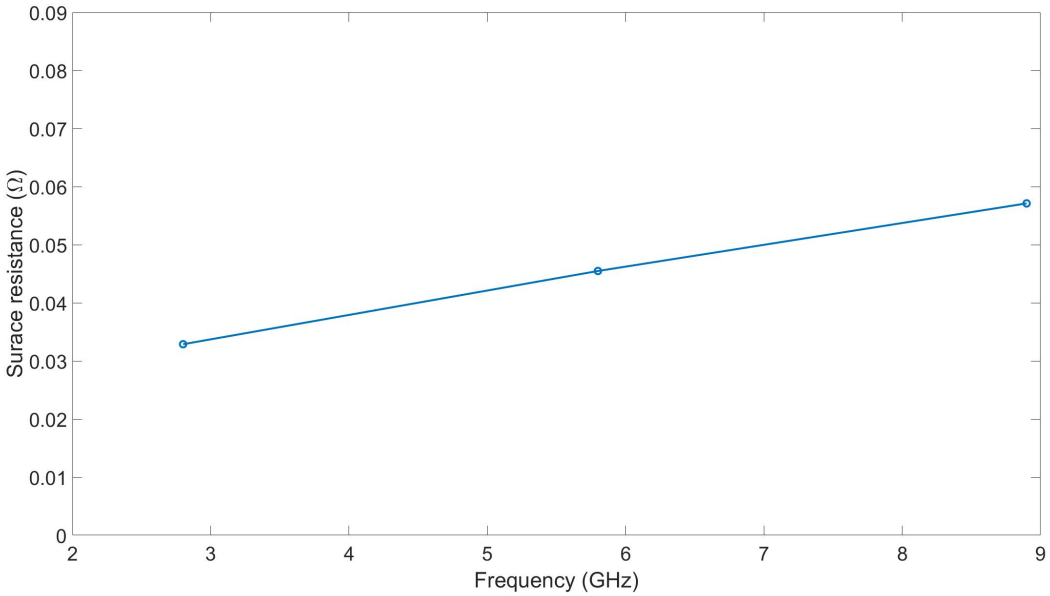

Figure A.22: Machined samples frequency response of R_S when a vertical magnetic filed is applied for the 45 degrees built part downwards facing surface.

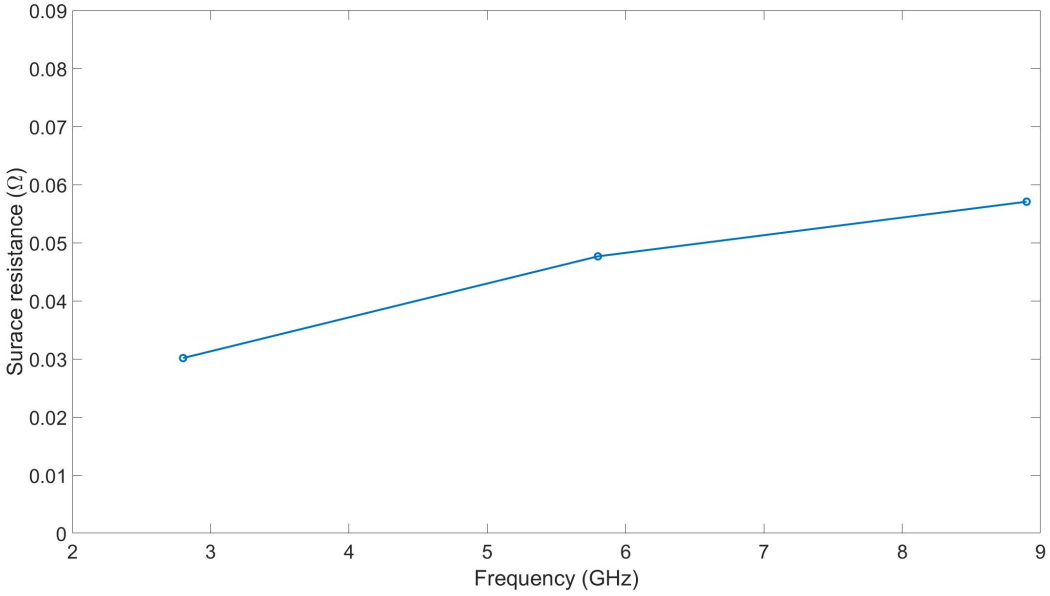

Figure A.23: Machined samples frequency response of R_S when a horizontal magnetic filed is applied for the 45 degrees built part downwards facing surface.

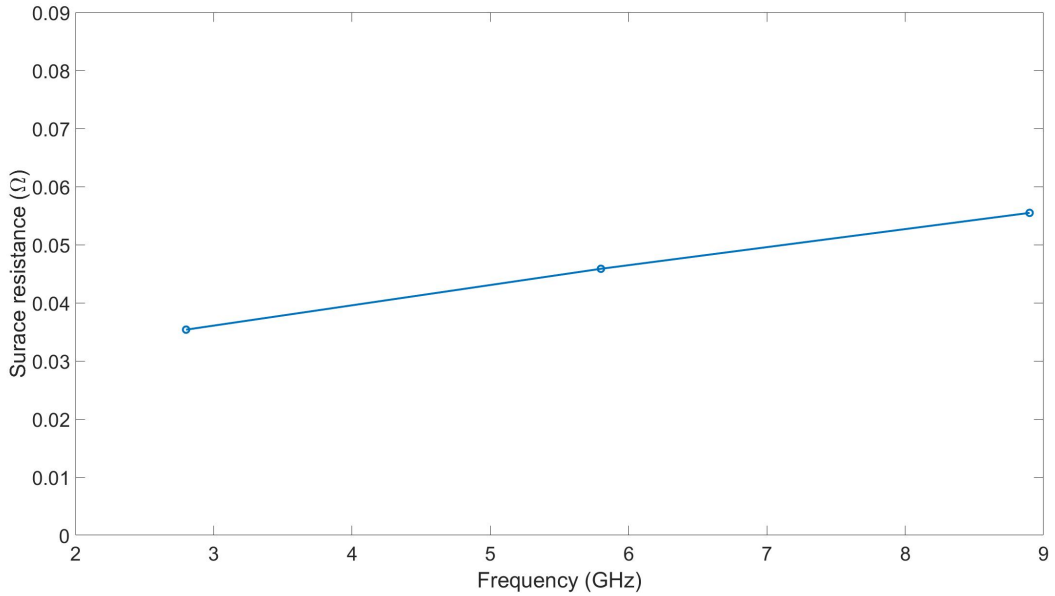

Figure A.24: Machined samples frequency response of R_S when the magnetic filed is applied at a 45 degrees for the 45 degrees built part downwards facing surface.

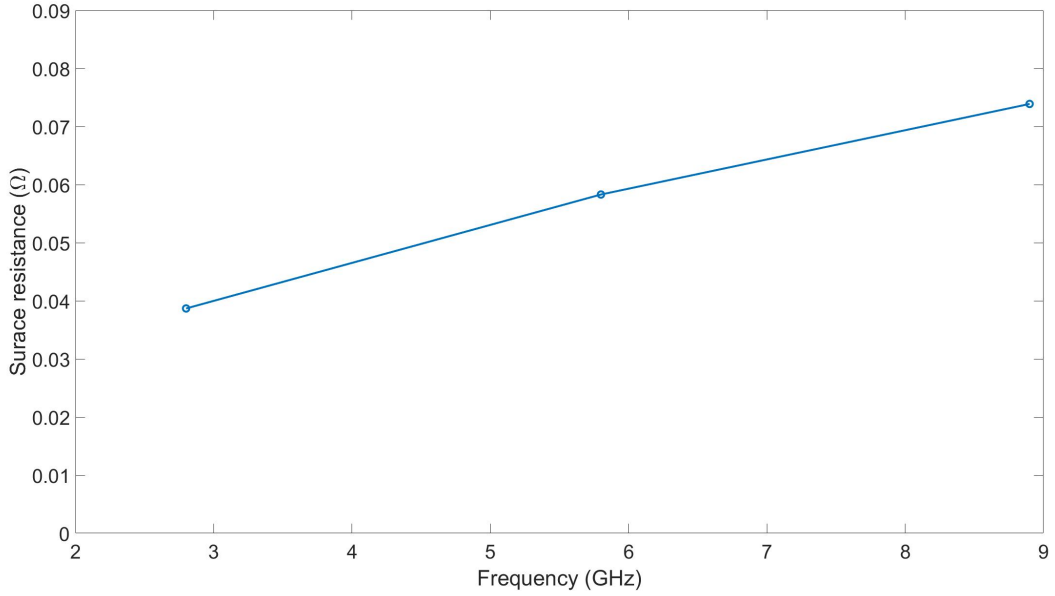

Figure A.25: Media tumbled samples frequency response of R_S when a vertical magnetic filed is applied for a vertically built part.

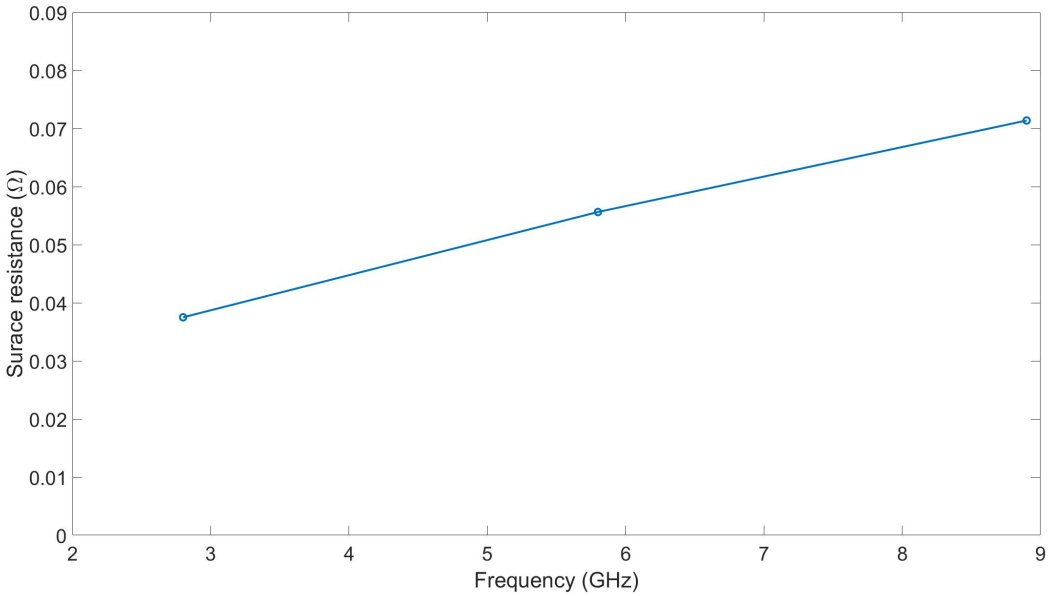

Figure A.26: Media tumbled samples frequency response of R_S when a horizontal magnetic filed is applied for a vertically built part.

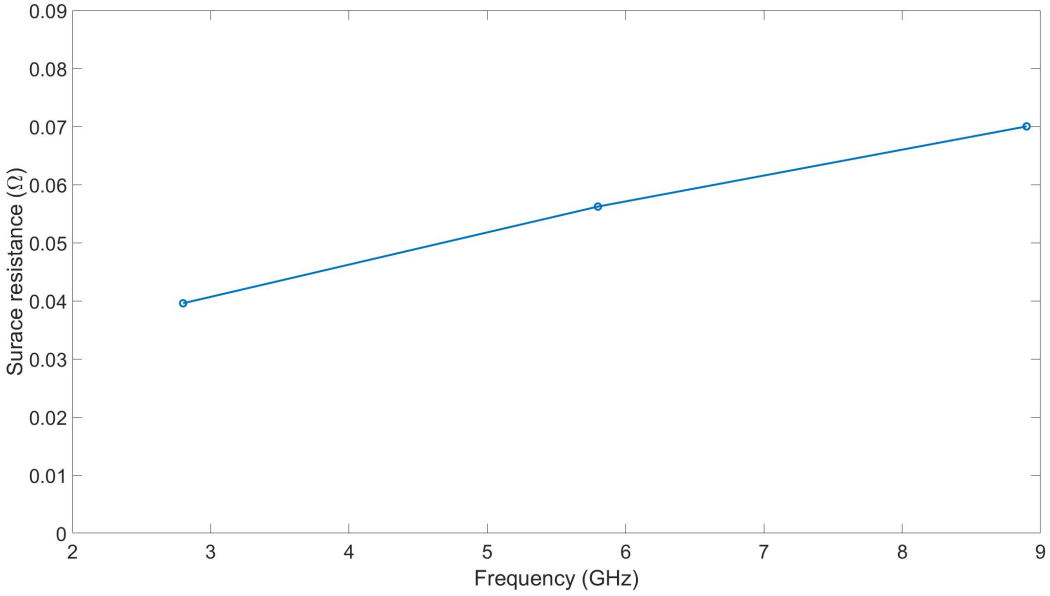

Figure A.27: Media tumbled samples frequency response of R_S when the magnetic filed is applied at a 45 degrees for a vertically built part.

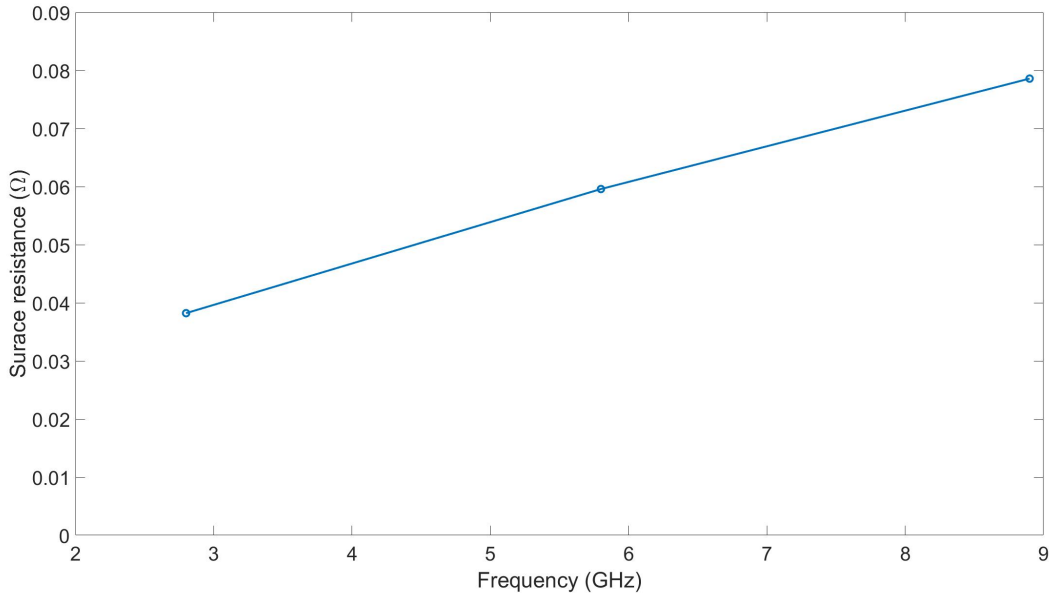

Figure A.28: Media tumbled samples frequency response of R_S when a vertical magnetic filed is applied for a horizontally built part.

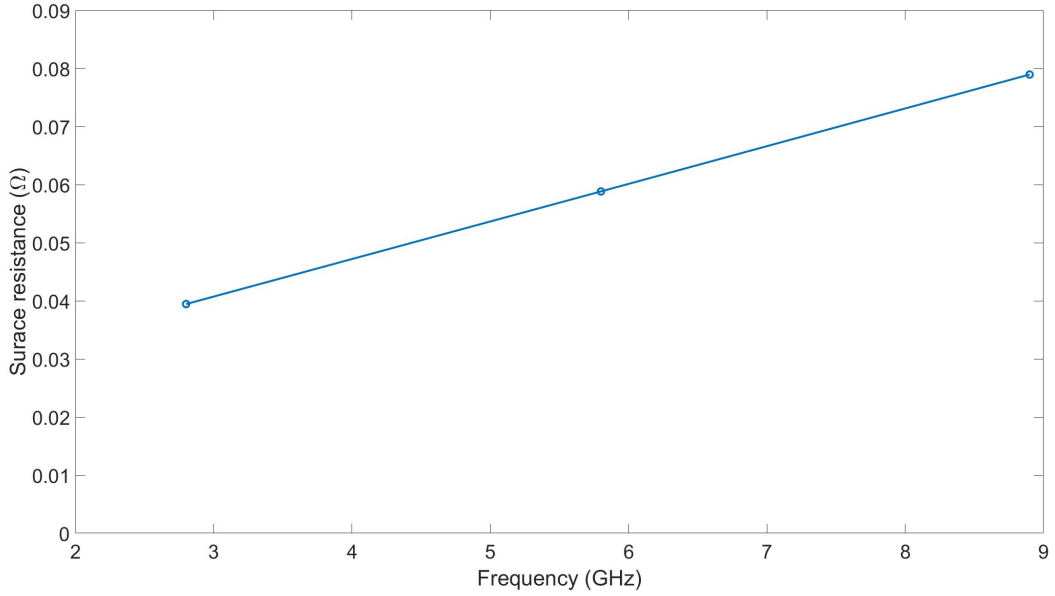

Figure A.29: Media tumbled samples frequency response of R_S when a horizontal magnetic filed is applied for a horizontally built part.

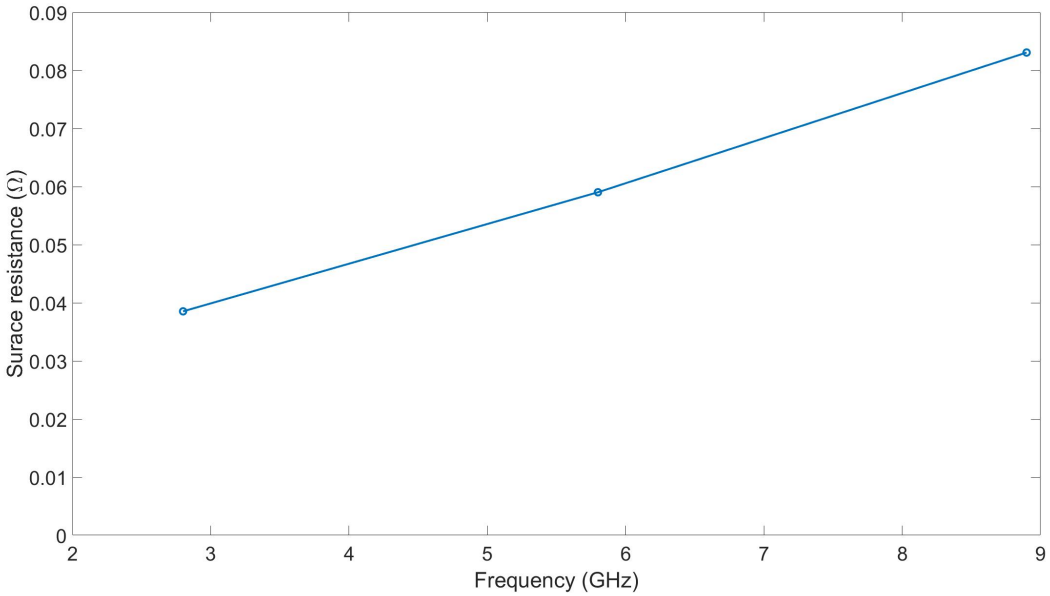

Figure A.30: Media tumbled samples frequency response of R_S when the magnetic filed is applied at a 45 degrees for a horizontally built part.

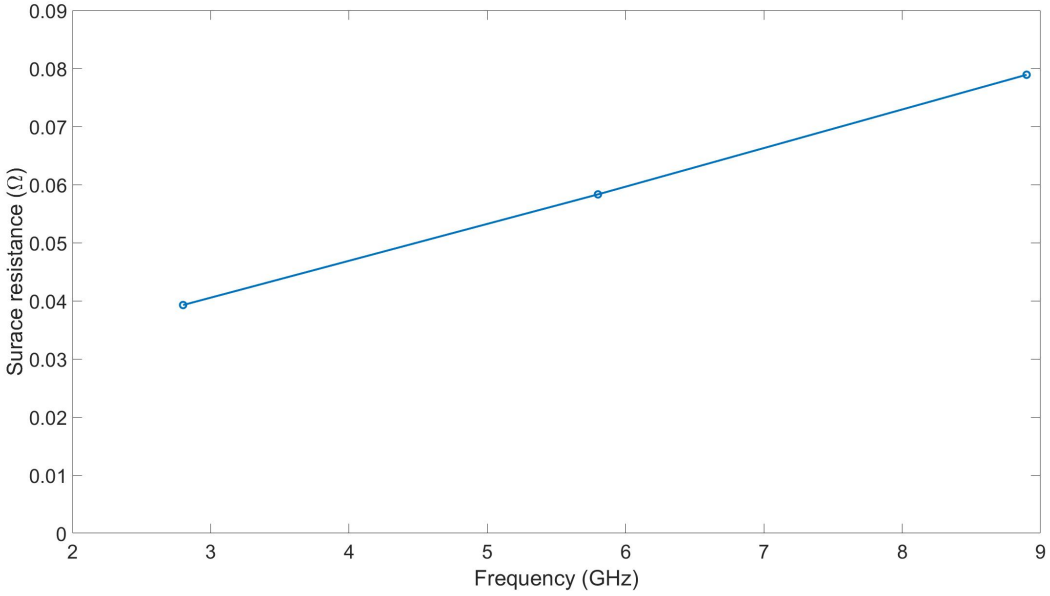

Figure A.31: Media tumbled samples frequency response of R_S when a vertical magnetic filed is applied for the 45 degrees built part upwards facing surface.

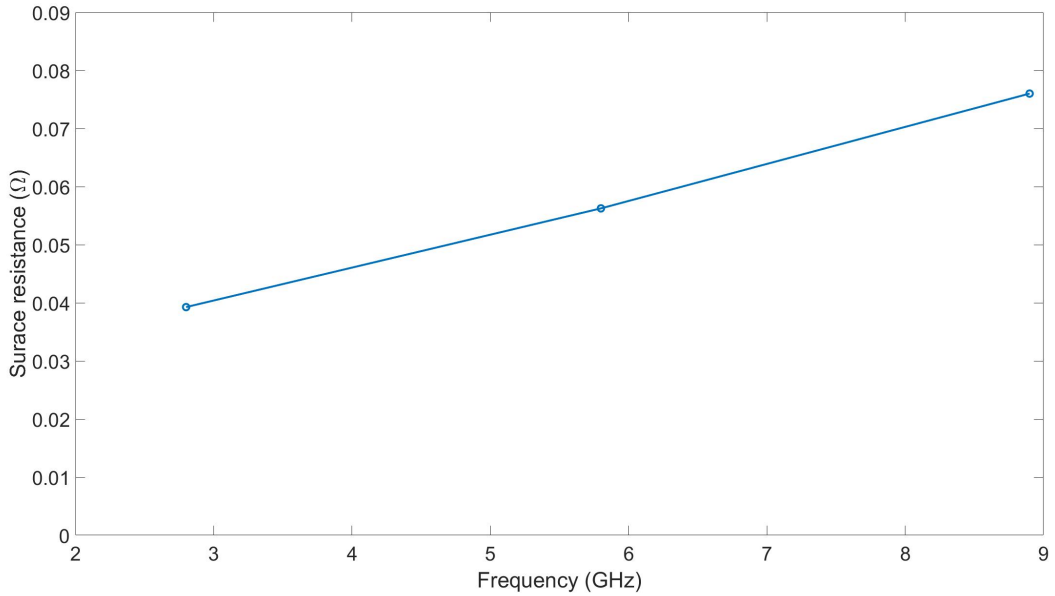

Figure A.32: Media tumbled samples frequency response of R_S when a horizontal magnetic filed is applied for the 45 degrees built part upwards facing surface.

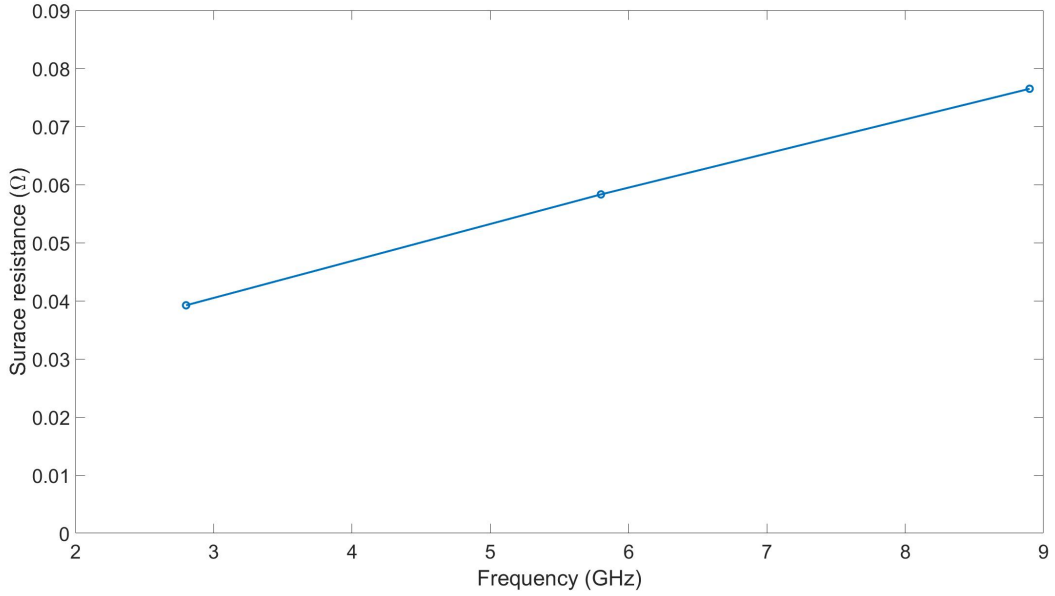

Figure A.33: Media tumbled samples frequency response of R_S when the magnetic filed is applied at a 45 degrees for the 45 degrees built part upwards facing surface.

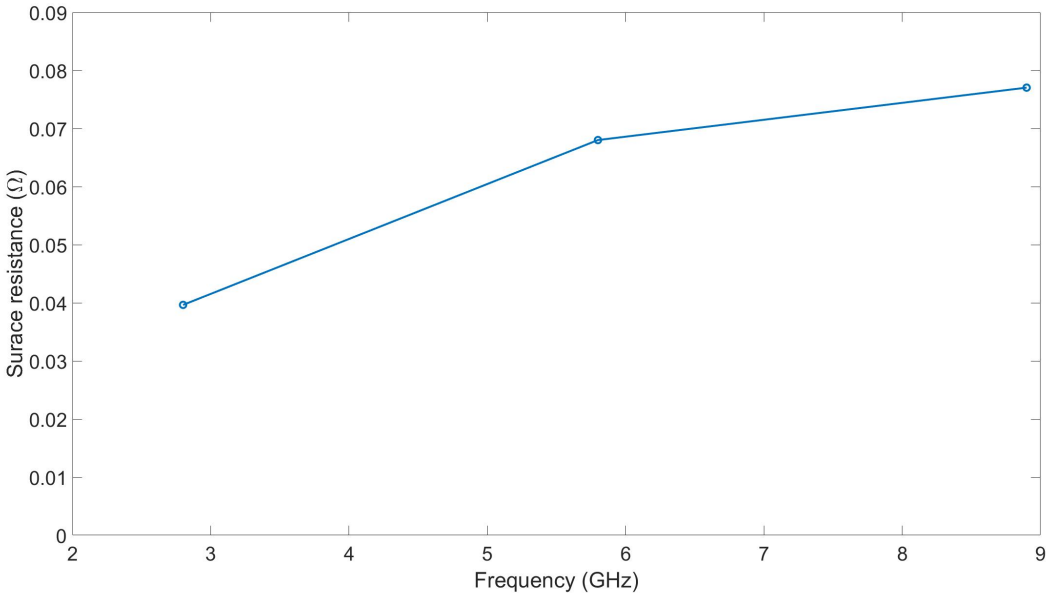

Figure A.34: Media tumbled samples frequency response of R_S when a vertical magnetic filed is applied for the 45 degrees built part downwards facing surface.

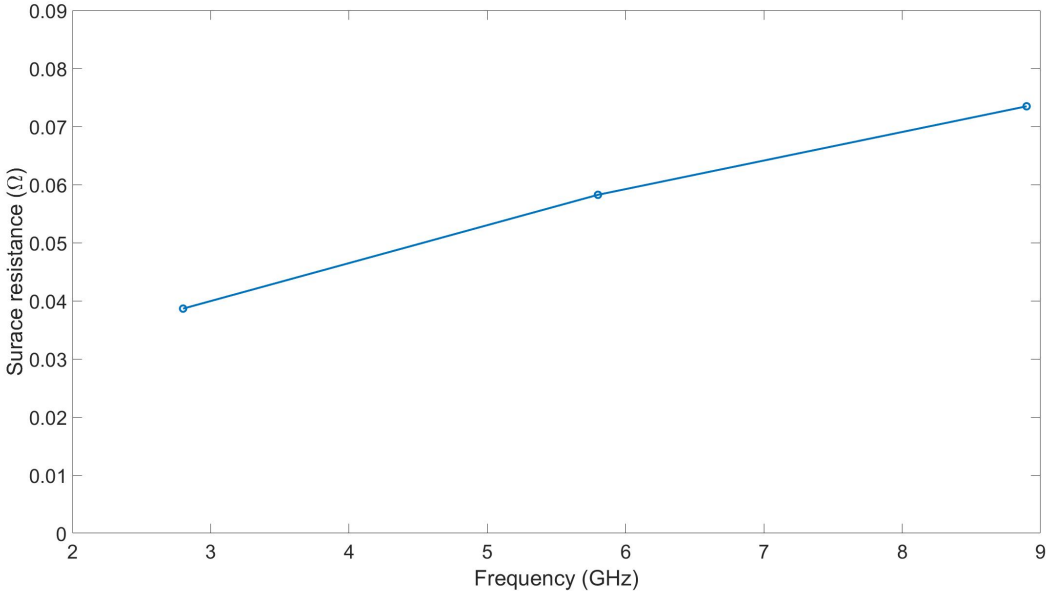

Figure A.35: Media tumbled samples frequency response of R_S when a horizontal magnetic filed is applied for the 45 degrees built part downwards facing surface.

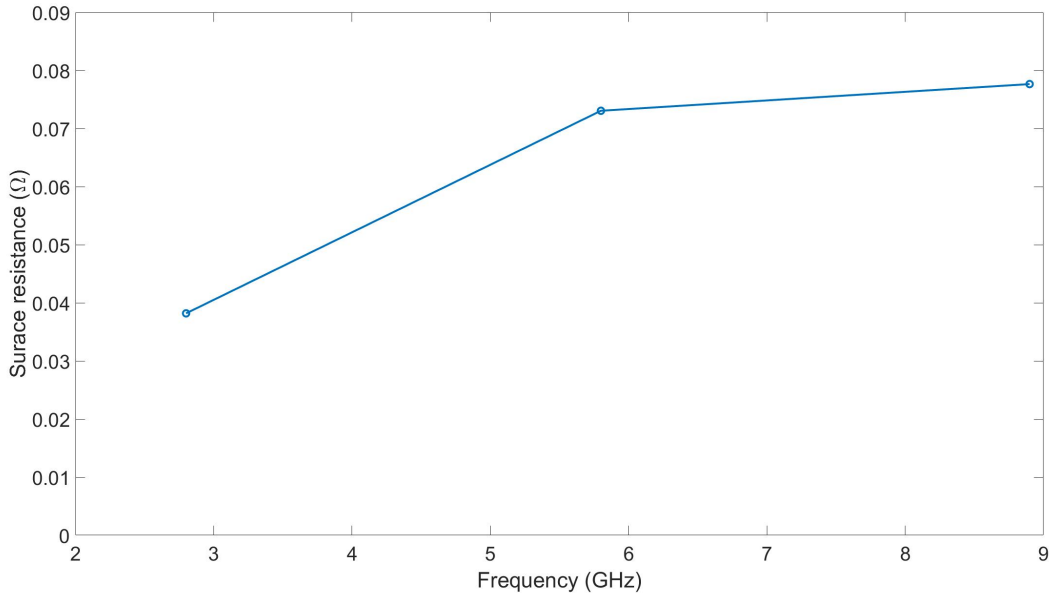

Figure A.36: Media tumbled samples frequency response of R_S when the magnetic filed is applied at a 45 degrees for the 45 degrees built part downwards facing surface.

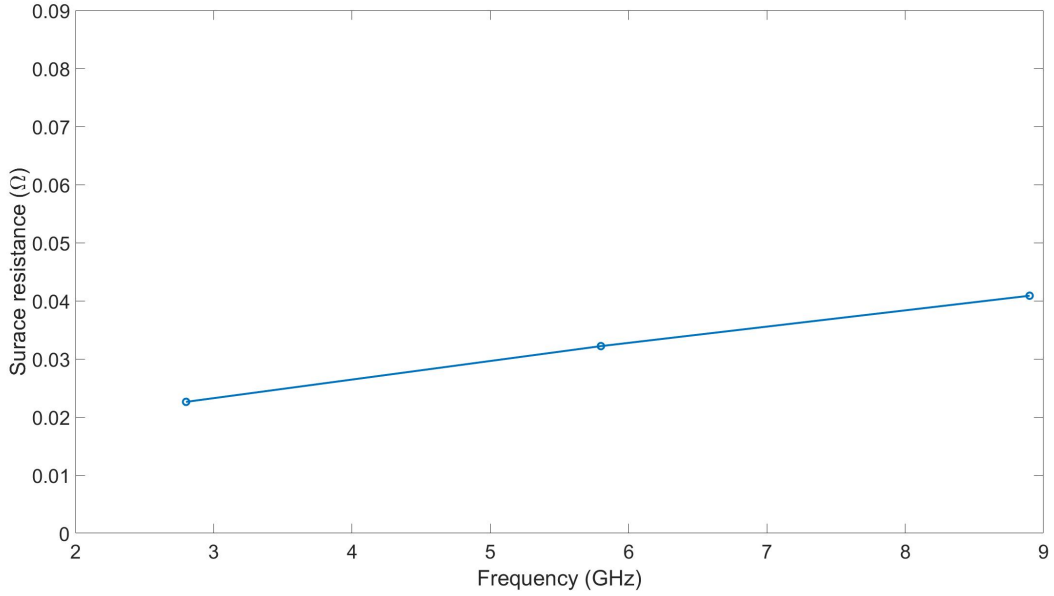

Figure A.37: Silver plated samples frequency response of R_S when a vertical magnetic filed is applied for a vertically built part.

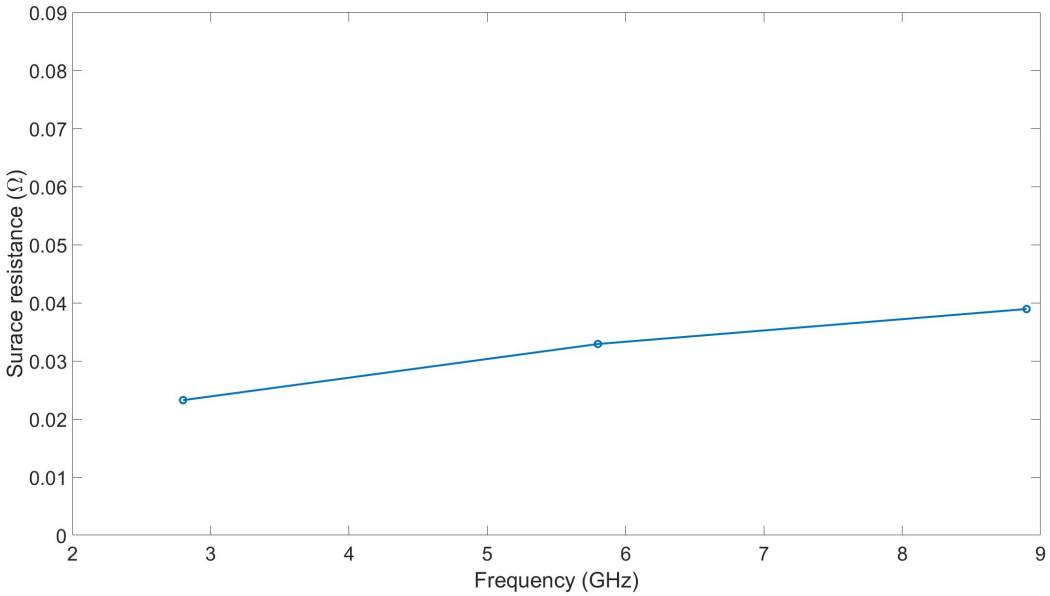

Figure A.38: Silver plated samples frequency response of R_S when a horizontal magnetic filed is applied for a vertically built part.

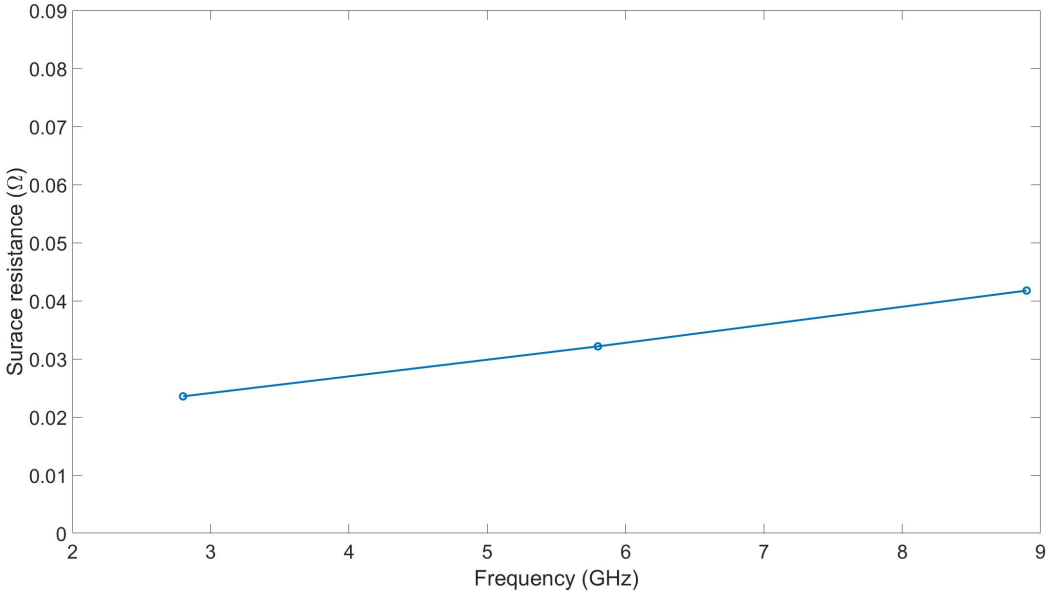

Figure A.39: Silver plated samples frequency response of R_S when the magnetic filed is applied at a 45 degrees for a vertically built part.

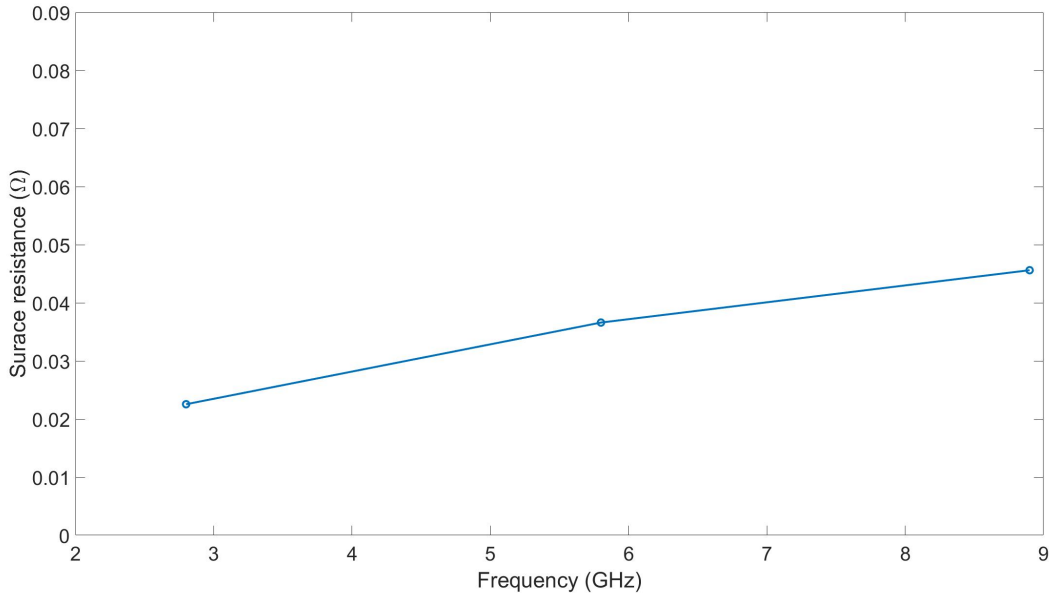

Figure A.40: Silver plated samples frequency response of R_S when a vertical magnetic filed is applied for a horizontally built part.

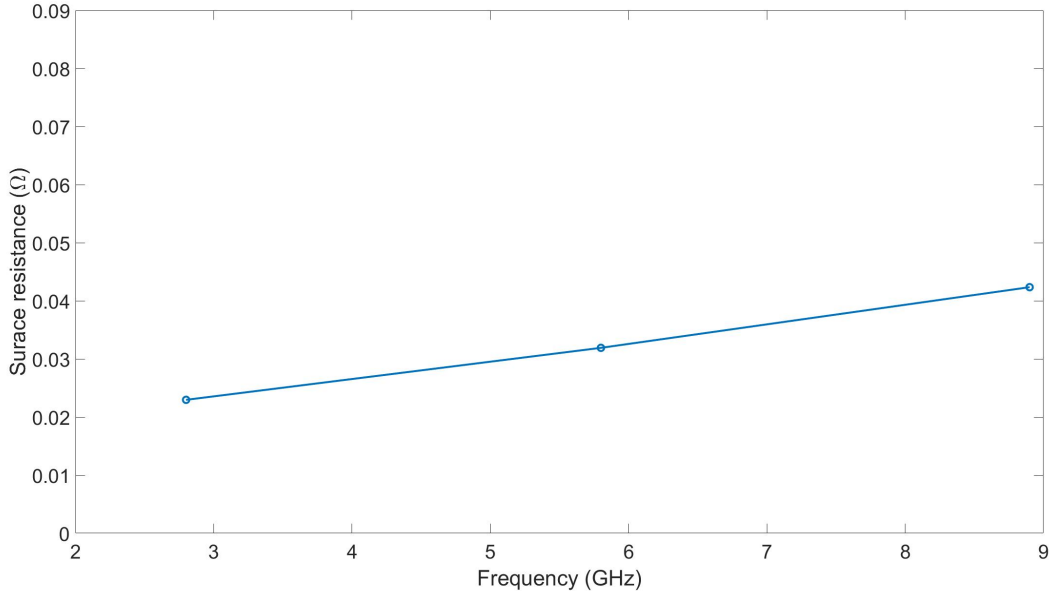

Figure A.41: Silver plated samples frequency response of R_S when a horizontal magnetic filed is applied for a horizontally built part.

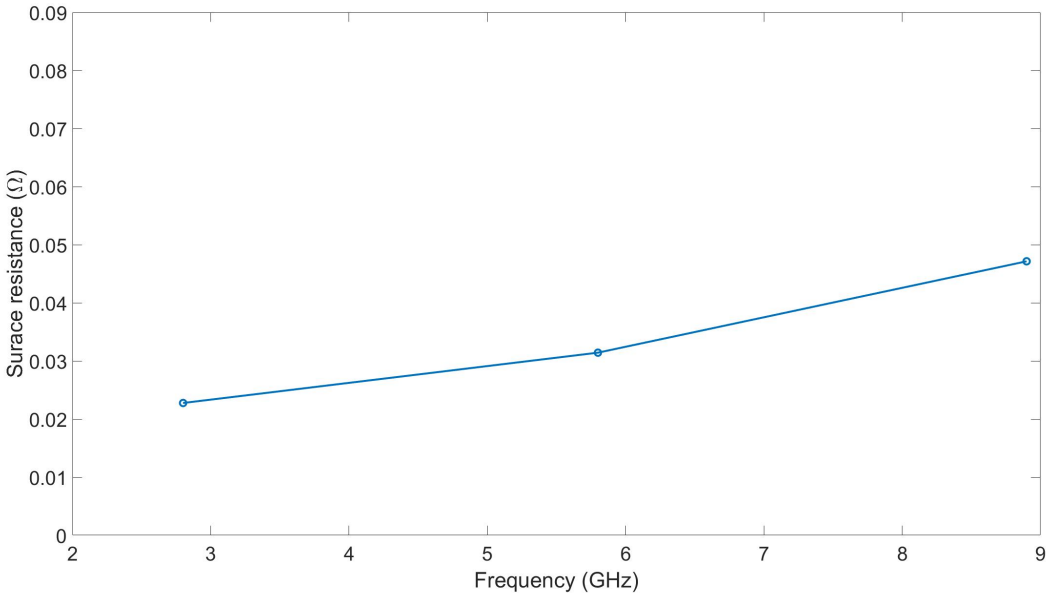

Figure A.42: Silver plated samples frequency response of R_S when the magnetic filed is applied at a 45 degrees for a horizontally built part.

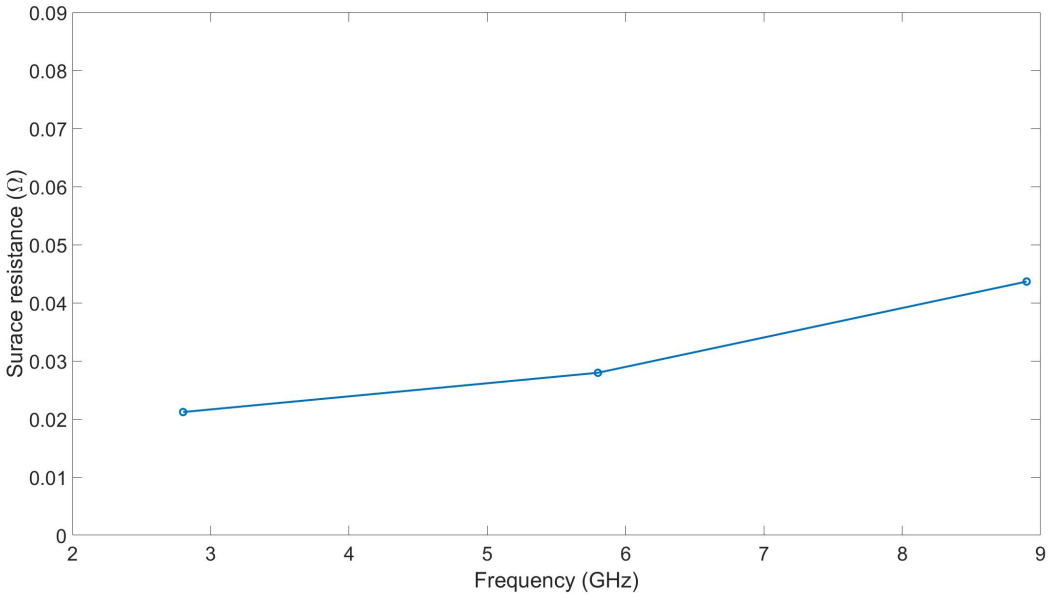

Figure A.43: Silver plated samples frequency response of R_S when a vertical magnetic filed is applied for the 45 degrees built part upwards facing surface.

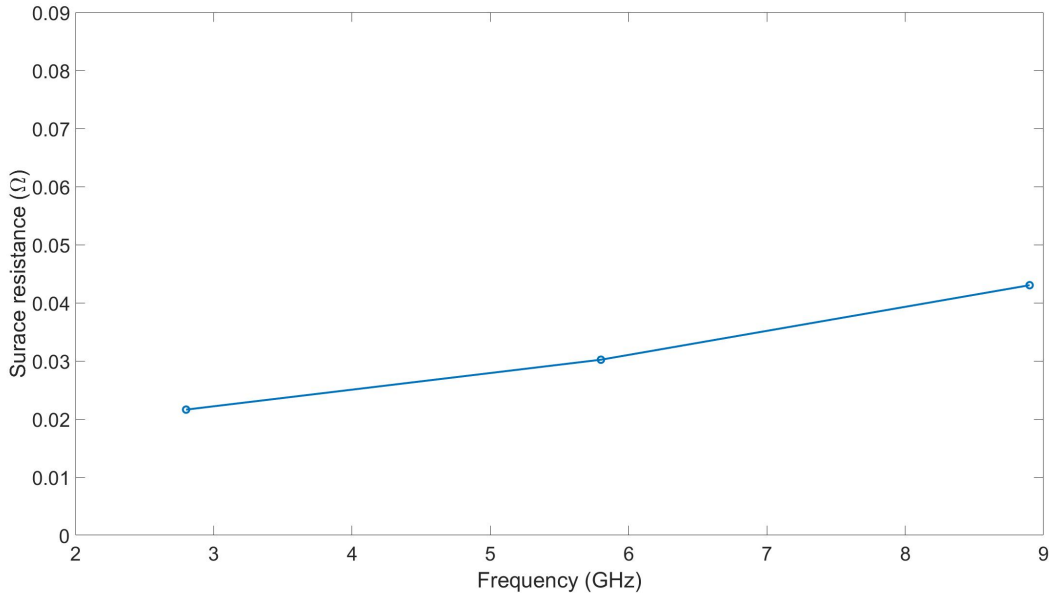

Figure A.44: Silver plated samples frequency response of R_S when a horizontal magnetic filed is applied for the 45 degrees built part upwards facing surface.

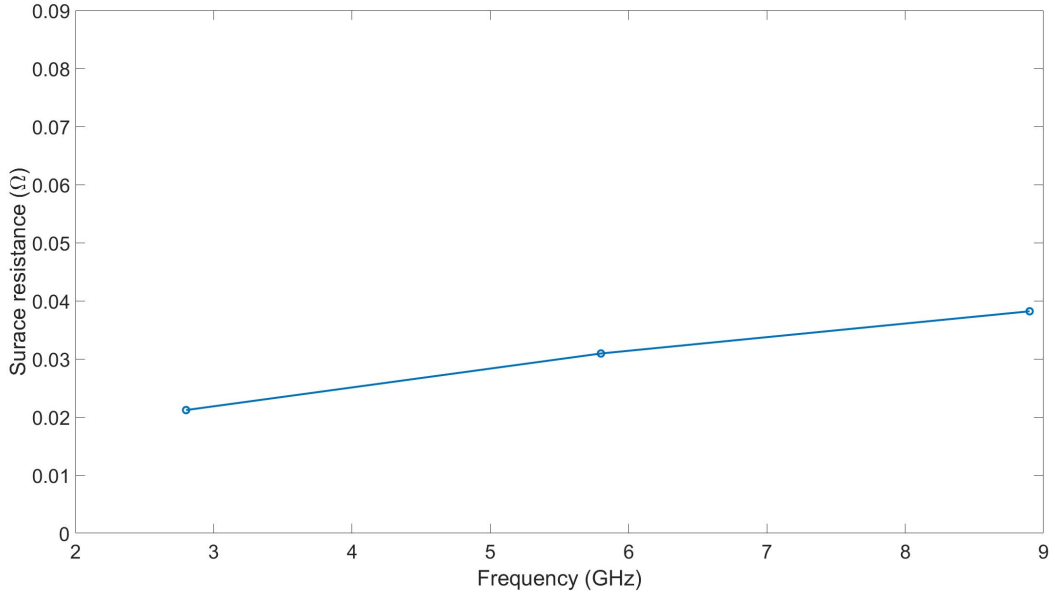

Figure A.45: Silver plated samples frequency response of R_S when the magnetic filed is applied at a 45 degrees for the 45 degrees built part upwards facing surface.

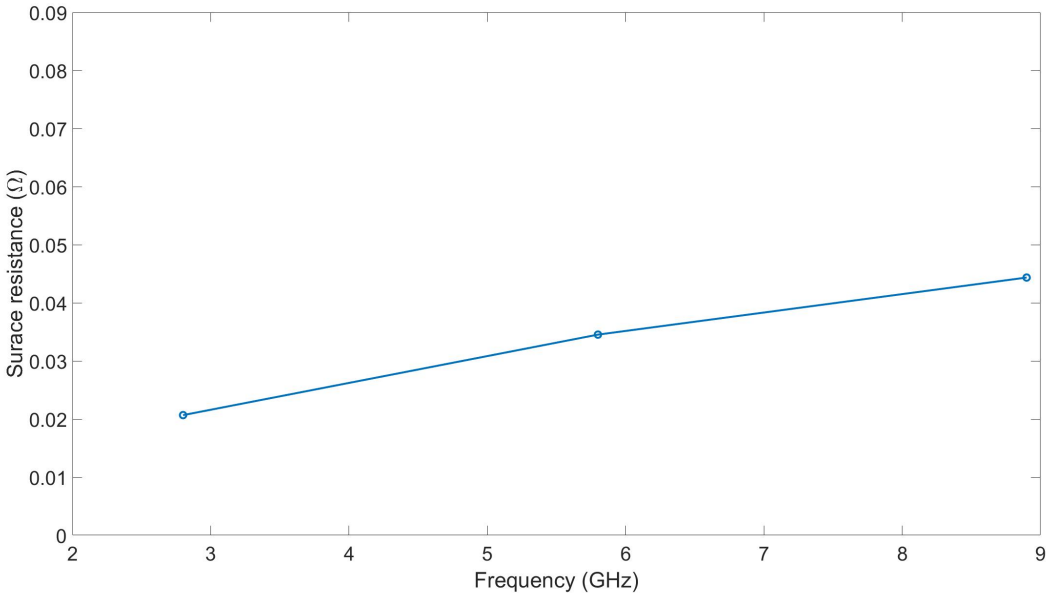

Figure A.46: Silver plated samples frequency response of R_S when a vertical magnetic filed is applied for the 45 degrees built part downwards facing surface.

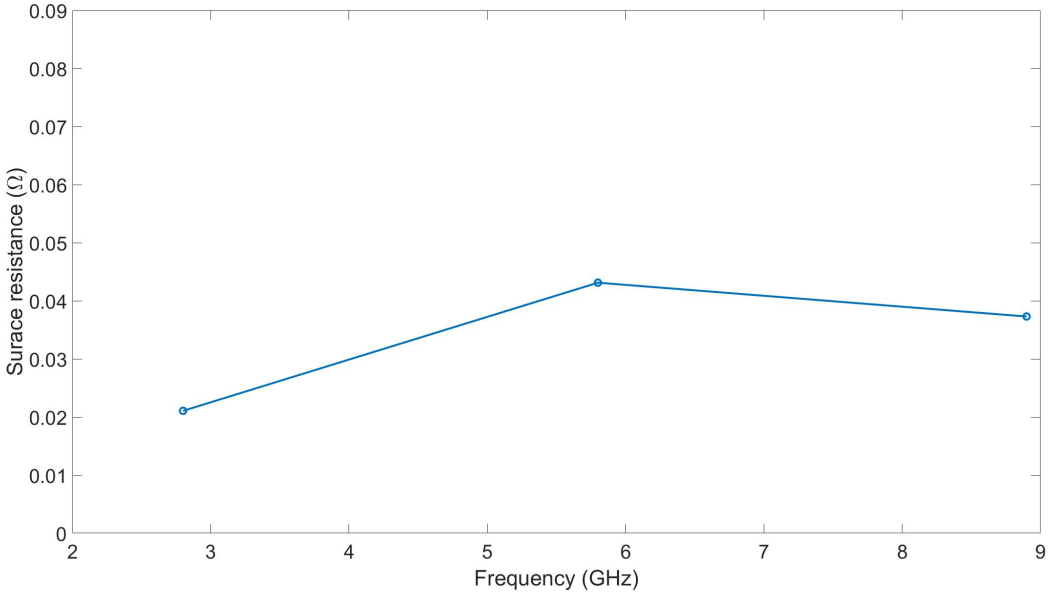

Figure A.47: Silver plated samples frequency response of R_S when a horizontal magnetic filed is applied for the 45 degrees built part downwards facing surface.

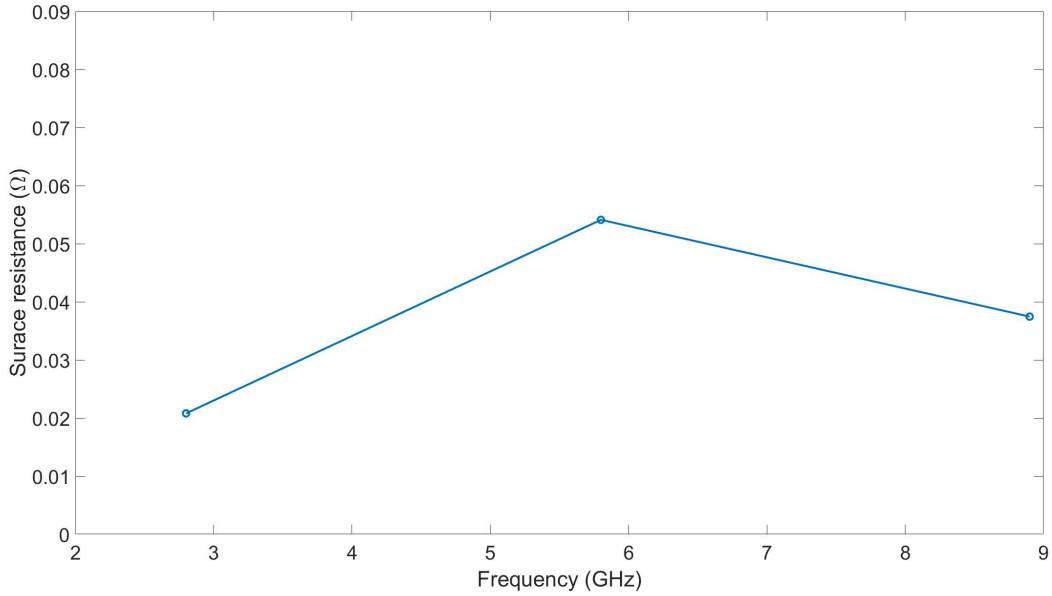

Figure A.48: Silver plated samples frequency response of R_S when the magnetic filed is applied at a 45 degrees for the 45 degrees built part downwards facing surface.

A.2 Published papers

IEEE Access
Multidisciplinary ⋮ Rapid Review ⋮ Open Access Journal

Received March 1, 2021, accepted March 14, 2021, date of publication March 19, 2021, date of current version March 26, 2021.

Digital Object Identifier 10.1109/ACCESS.2021.3067306

Effect of Build Orientation and Laser Power on Microwave Loss in Metal Additive Manufactured Components

RICHARD GUMBLETON[1], ROBERT BATSON[1], KENNETH NAI[2], AND ADRIAN PORCH[1]
[1]Centre for High Frequency Engineering, Cardiff University, CF24 3AA Cardiff, U.K.
[2]Group Engineering Division, Renishaw PLC, GL12 8JR Wotton-Under-Edge, U.K.

Corresponding author: Richard Gumbleton (gumbletonr1@cardiff.ac.uk)

This work was supported in part by the Engineering and Physical Sciences Research Council (EPSRC), and in part by Renishaw PLC through the Industrial Cooperative Awards in Science and Technology (ICASE) Studentship Program under Grant EP/R511882/1 and Grant EP/S513611/1.

ABSTRACT The adoption of metal additive manufacturing into the production of passive microwave components is still in its relative infancy. However, it is of increasing interest due to the offer of geometrical design freedom and significant weight reduction. The electrical properties of additive manufactured components are still inferior to traditional manufacturing techniques owing to the poor surface finish, especially on overhanging surfaces, which are unavoidable in three-dimensional microwave components. In this paper we present experimental findings on the disparity in microwave surface resistance values between three common build orientations, as well as findings that establish a connection between increasing downskin laser power and a reduction in surface resistance for overhanging surfaces. Finally, additive manufactured rectangular waveguide sections are measured to assess the influence of combined upward and downward facing surfaces on surface resistance.

INDEX TERMS Additive manufacture, metals, laser power, microwave, surface resistance, waveguide.

I. INTRODUCTION

Additive layer manufacturing (ALM) is of increasing interest within the aero/space industries due to its unique offering of unparalleled geometric design freedom. ALM produces parts with significant weight reduction compared with traditional manufacturing techniques, whilst maintaining up to 99.8% density [1]. Powder bed fusion (PBF), one form of ALM, uses spherical metal powder melted by a high power laser in successive layers to form three-dimensional components. A schematic of the PBF process is shown in Fig. 1. Although PBF adoption is still in relative infancy [2], many studies have been performed on their application to microwave communication components [3]–[5]. The electrical properties of PBF components are still inferior to machined alternatives [6], [7], however, the overall positive performance is somewhat surprising given the poor surface finish apparent on PBF surfaces. In particular, overhanging or downwards facing surfaces (with respect to the build direction) experience excessive dross formation and can generate significantly higher roughness than in other orientations [8], [9]. This suggests that some surfaces within a three-dimensional component will have better microwave performance than others, quantified in terms of microwave power loss. The main techniques used in literature to asses microwave PBF structures take a macro approach by measuring a complete waveguide component and comparing its performance to a traditional manufactured equivalent or simulation results [10], [11]. In this study, a more fundamental, experimental approach is taken; individual surfaces of different build orientations are assessed for microwave surface resistance (R_S), which are subsequently optimised through changes in PBF laser power.

The associate editor coordinating the review of this manuscript and approving it for publication was Xi Zhu.

II. BACKGROUND

A. MICROWAVE LOSS

At microwave frequencies, the skin effect causes electrical current to be carried in only the outermost regions of material at a depth known as the skin depth

$$\delta = \sqrt{\frac{1}{\pi f \mu \sigma}} \tag{1}$$

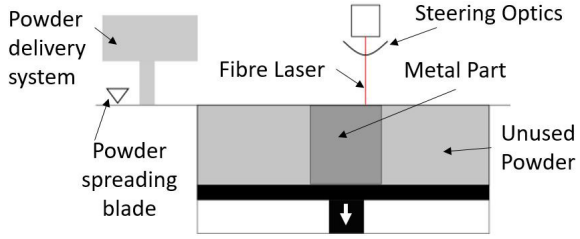

FIGURE 1. Schematic of the laser powder bed fusion manufacturing process. ©2019 Gumbleton *et al.* Reprinted from [12] (CC BY).

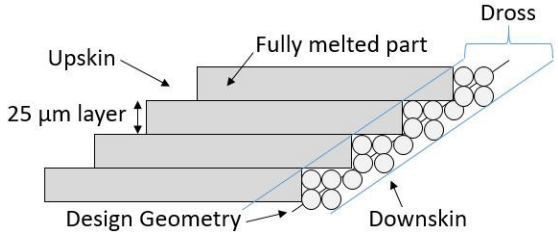

FIGURE 2. Schematic of dross formation on the downward facing surfaces during powder bed fusion manufacturing.

where f is the operating frequency (Hz), μ is magnetic permeability (H/m) and σ is electrical conductivity (S/m). For aluminium (of bulk conductivity $\sigma = 2.6 \times 10^7$ S/m) at a nominal frequency of 6.4 GHz (used in our characterisation experiments) the skin depth is calculated to be ≈ 1.2 μm. Therefore, with the majority of current carried at the surface of the material, even micro-surface features can have a significant impact on microwave loss; the relationship between roughness and microwave loss is well established in literature [13]. Power dissipation in a conductor at microwave frequencies is defined by

$$P_c = \frac{R_S}{2} \int_S |H_S|^2 dS \tag{2}$$

where S is the surface area on which the current flows (m^2), H_S is the tangential magnetic field at the metal surface (A/m) and R_S (Ω) is the quantifying metric for microwave loss, which encompasses surface roughness through an effective conductivity (σ_{eff}) as

$$R_S = \sqrt{\frac{\pi f \mu}{\sigma_{\text{eff}}}} \tag{3}$$

Since the average particle size is ~47 μm for AlSi10Mg powder (with a range between 15 and 120 μm [14]) and $\delta \approx 1.4$ μm, it is justified to assume that the majority of current is flowing in one PBF layer. Therefore particular attention can be paid to optimising the outermost layers on each surface, such that the mechanical properties defined by the core PBF parameters remain unaltered. This is akin to the normal process of coating base metals such as brass with a thin layer of silver or gold for use in microwave components.

B. OVERHANG ROUGHNESS

The high degree of surface roughness seen on overhanging surfaces is, in part, attributed to dross formation, where a fraction of the laser energy penetrates below the desired layer and partially melts powder to the surface [15]; a representation of this phenomena is shown in Fig. 2. The adherence of partially melted powders is explained, at a fundamental level, by the surface energy of their spherical shapes. A sphere has the largest surface area for a shape of fixed volume, requiring less energy to form new bonds with other surfaces than is required to fully melt the powder [16].

In the context of PBF, 'downskin' is used to refer to a scan path which is not directly on top of a previously processed layer. The downskin applies to any downwards facing surface at an angle below the set activation angle, 60° in this case, relative to the build plate. Conversely, an 'upskin' refers to any laser path that does not have a proceeding layer directly above; each case has a different set of process parameters for manufacture. The downskin process parameters are set so that the laser raster passes several times over the dross region, melting more of the adhered powder with each pass. Studies have identified that for parts built in a 45° orientation, high laser energy density on the downskin layers can lead to a reduction in surface roughness [17], which may correlate to a reduction in surface resistance.

III. EXPERIMENTAL SETUP

Samples are prepared in AlSi10Mg using a Renishaw RenAM500 additive manufacturing system, which utilises a 500 W, ytterbium fibre laser of 1080 nm wavelength and 70 μm focal diameter. The samples have been built in horizontal, vertical and 45° orientations, as shown in Fig. 3, with varying laser power setups for vertical and 45° plates. The populated build plate is shown in Fig. 4. The default laser power for 45° upskin and downskin is 100 W, while the default laser power for the border scan on vertical built parts is 350 W, which are identified by (D) in Table. 1; these samples are used to quantify disparity in R_S between the different build orientations. The remaining samples are subjected to

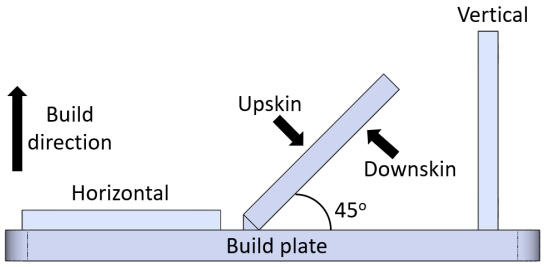

FIGURE 3. Schematic of the three build orientations used for sample manufacture.

TABLE 1. Laser power levels of 45° upskin and downskin and vertical built sample plates.

	45° Upskin & Downskin	Vertical
Power (W)	0, 60, 80, 100 (D), 120, 140, 160,	250, 270, 290, 310, 350 (D), 370, 410, 430, 450, 470,

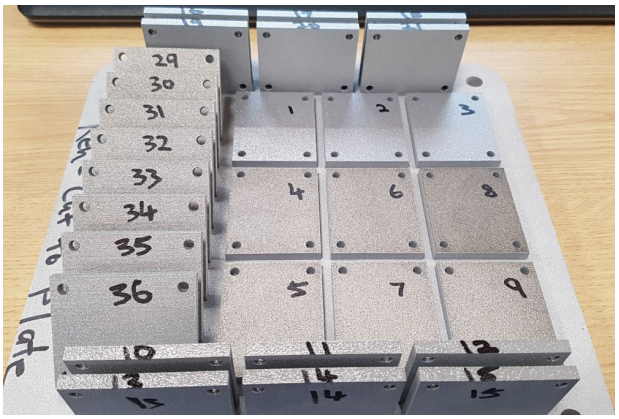

FIGURE 4. Photograph of the sample populated Renishaw RenAM500 additive manufacturing build plate.

variations in laser power levels, also shown in Table. 1, and are centered around the default values. All microwave characterisation measurements have been performed using a parallel plate resonator (PPR) setup, described in full in [18], where directional currents are induced in the study sample by the excitation of orthogonal resonant modes. The results reported here are measured at 6.4 GHz in the TEM_{010} resonant mode; a drawing of the PPR and simulations of its electric and magnetic fields, as well as induced current flow for this mode, are shown in Fig. 5. The reference plate is common to all measurements and its dimensions set the resonant frequency of the cavity, while the sample under test rests atop an indium gasket and is secured by bolts at each corner.

The operating principle of the PPR setup relies on the accurate measurement of quality (Q) factor while using a calibration sample before solving Eq. 4 to leave the sample R_{Ss} as the only unknown variable to be analysed when measuring a sample.

$$\frac{1}{Q_T} = G_s R_{Ss} + \sum_{m=1}^{i} G_{w_m} R_{Sw_m} + \sum_{p=1}^{j} p_{ed_p} \tan\delta_p \qquad (4)$$

where Q_T is the total Q factor of the system, all measured Q factors are loaded values, including the effects of the coupling coefficients, and are corrected to produce unloaded values before calculation of surface resistance; the method is described in detail in [19]. R_{Ss} and G_s, R_{Sw} and G_w are the surface resistances and geometric values associated with the sample and the summation of i remaining conductive walls of the cavity, respectively, while p_{ed} is the dielectric filling fraction for j dielectric volumes present in the fixture. The geometric factors and dielectric filling fractions are defined as

$$G = \frac{1}{\omega} \frac{\iint_s \vec{H}_t \cdot \vec{H}_t^* ds}{\iiint_v \mu_0 \vec{H} \cdot \vec{H}^* dv} \qquad (5a)$$

$$p_{ed} = \frac{\iiint_{vd} \varepsilon_d \vec{E} \cdot \vec{E}^* dv}{\iiint_v \varepsilon_v \vec{E} \cdot \vec{E}^* dv} \qquad (5b)$$

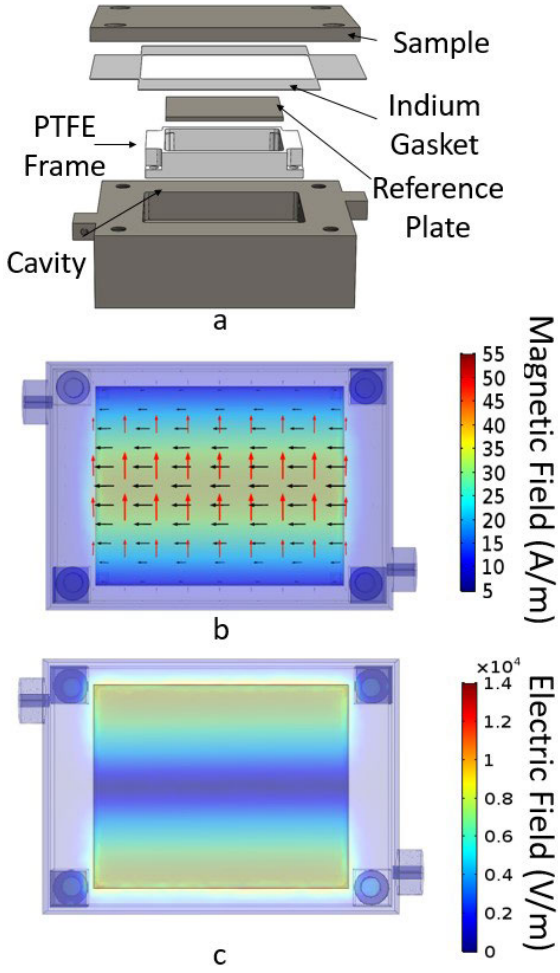

FIGURE 5. Parallel plate resonator fixture. a) Exploded CAD image and simulated electromagnetic properties for TEM_{010} mode at 6.4 GHz b) magnetic field (black arrows), magnetic field magnitude (color scale) and induced surface current (red arrows), c) electric field magnitude. Simulations are performed using COMSOL Multiphysics software with an arbitrary input power of 1 W. ©2021 IEEE. Reprinted, with permission, from IEEE [18].

where s is the surface integral for the conductive surface, v_d is the volume integral for the dielectric volume and v is the volume integral for the host cavity. μ_0 is the permeability of free space, and ε_d and ε_v are the permittivity of the component material and the material filling the cavity, respectfully. All microwave measurements were performed using a high precision Keysight N5232A vector network analyser.

IV. RESULTS AND DISCUSSION

A. BUILD ORIENTATION

Samples produced using default build parameters in different orientations have been measured for R_S and the results are shown in Fig. 6. The standard error reported on Fig. 6 is very small due to the high precision frequency measurement equipment used (Keysight N5232A network analyser), with less than 0.1% random error and the described cavity resonator fixture providing approximately 1% systematic error from the removal and replacement of samples. The 45° downskin surface, perhaps predictably, performs

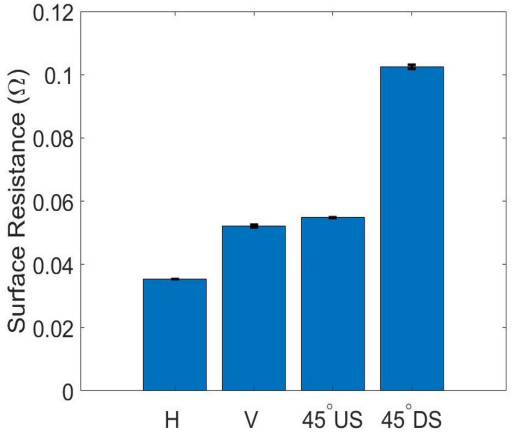

FIGURE 6. Measured surface resistance values for samples of different build orientation using default process parameters. Standard error is shown via error bars.

significantly worse in terms of microwave loss than other build orientations. Horizontal built plates exhibit the lowest loss of all samples, a result that supports previous measurements by this author [20], while there is only a marginal difference between vertical and 45° upskin surfaces. RMS surface roughness (R_q) measurements have been performed using a Taly Surf Series 2 drag profiler fitted with a tip of 2 μm radius and analysed with a 0.8mm cutoff low pass filter. R_q for the default values ($\sim$6 μm for horizontal, $\sim$12 μm for vertical, $\sim$13 μm for 45° upskin and $\sim$20 μm for 45° downskin orientations) correspond well with measured R_S, which increases with increasing surface roughness. From these results, it is evident that a macro approach to testing microwave components produced by PBF is missing important information regarding the specific locations where loss contributions are occurring and hence overall performance will be heavily dependent on the build orientation of the part.

B. LASER POWER

Fig. 7 shows the measured R_S values and R_q of 45° upskin and downskin surfaces and for samples built in a vertical orientation, against varying process laser power. In all cases R_S correlates well with observed changes in R_q. Fig. 7a and b correspond R_S values for vertical and 45° upskin surfaces, respectively; no significant pattern is observed relating R_S to changes in laser power. This may be explained for the upskin through the core build process having sufficiently melted the layer prior to the upskin parameters being implemented. Similarly, for the vertical built samples, border scans are repeated over successive layers, allowing for heat transfer through multiple layers such that a stable melt pool is generated, thus avoiding splutter and an excess of partially adhered powders.

Interestingly, the 45° downskin surfaces do exhibit a significant improvement with increasing laser power, shown in Fig. 7c. This is quantified by low values of R_S and correlates with lower values of R_q. Fig. 8 shows microscope images of the downskin surfaces for the worst (60 W) and best (180 W) performing samples. The 60 W sample (Fig. 8a)

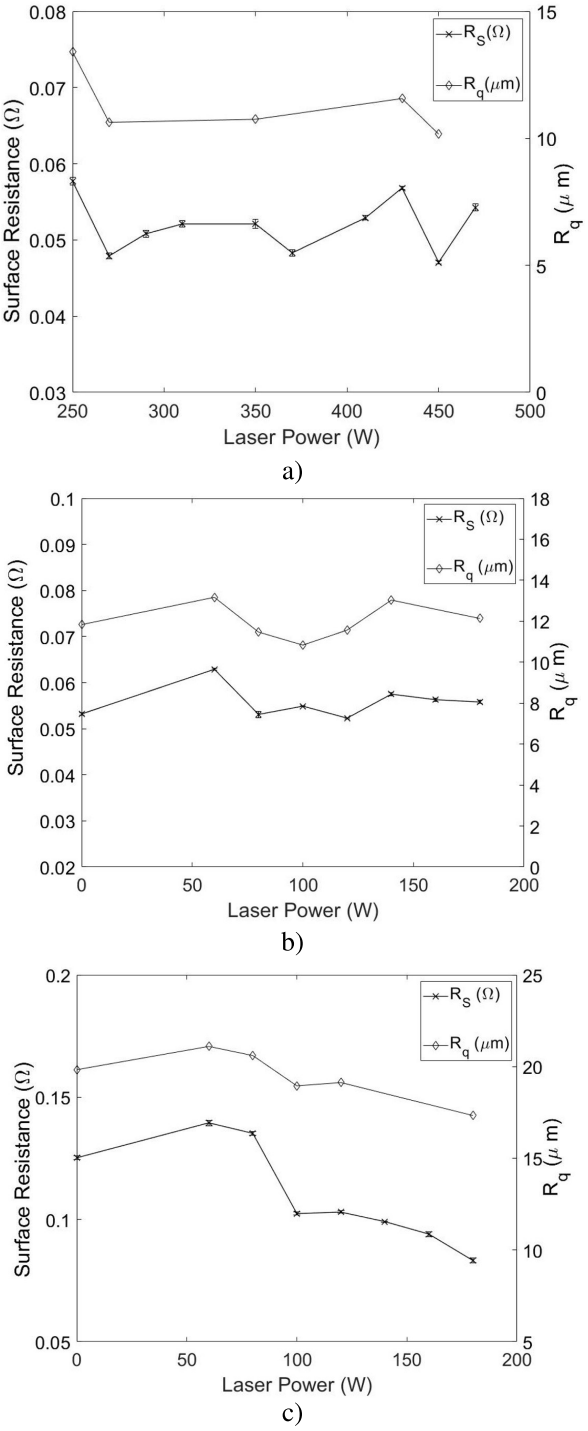

FIGURE 7. Graphs of measured surface resistance at different laser powers for a) vertical, b) 45° upskin and c) 45° downskin build orientations.

consists of an abundance of isolated satellites adhered only to the underlying surface. These partially melted powder spheres or satellites neither form a smooth surface or a sufficient electrical connection, and so are a major microwave loss contributor. In the 180 W sample (Fig. 8b), however, these satellites appears to have formed into larger agglomerates with surrounding particles, creating a more effective network of electrical connection and a more coherent layer. This is explained by the additional energy density penetrating deeper

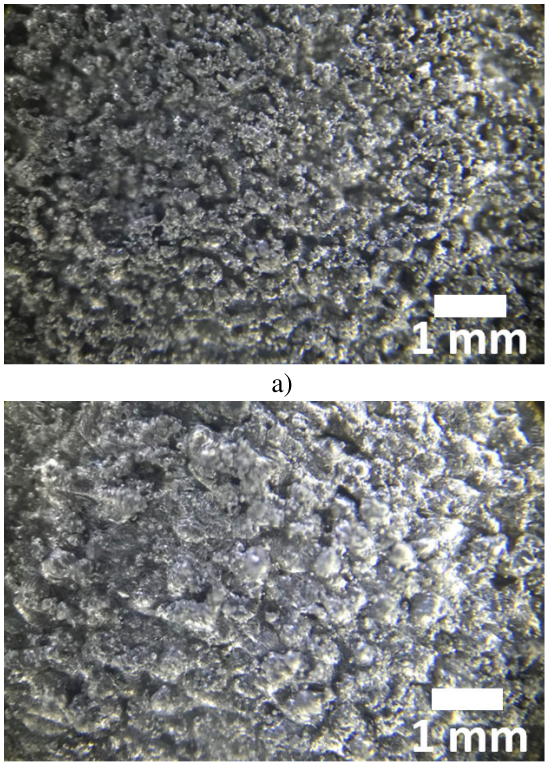

FIGURE 8. Microscope images of 45° downskin surfaces manufactured with laser powers of a) 60 W and b) 180 W. Scale bar is set at 1 mm.

into this layer and more fully melting a greater proportion of the particles.

C. APPLICATION TO WAVEGUIDE COMPONENTS

To test the influence of the above laser power optimisation, a series of 45° orientated waveguide sections have been manufactured, as shown in Fig. 9a. The build orientations is such that two internal surfaces of each waveguide are upwards facing and use the default parameter setup, while the remaining downward facing surfaces are swept for each waveguide section using the following laser powers; ALM1 = 100 W (default), ALM2 = 0 W and ALM3 = 180 W. Fig. 9b shows one of these waveguide sections connected to a vector network analyser, through magnetic coupling loops, by using blank end flanges; this converts the waveguide transmission line section into a waveguide resonant cavity, allowing loss to be measured more reliably through Q factor than the attenuation from the measurement of transmitted power. Q factor and hence R_S are measured through the forward transmission S parameter S_{21}. These traces are shown as an inset to Fig. 10. The resonant frequency of the dominant TE_{101} mode of this air filled cavity is 6.62 GHz, a similar frequency to the PPR measurements for consistency of results and dictated by the internal geometry of the cavity; 22.86±0.06 mm × 10.16±0.1 mm × 154±0.1 mm. R_S for the cavity geometry is found by

$$R_{Sr} = \frac{1}{G\,Q_T} \tag{6}$$

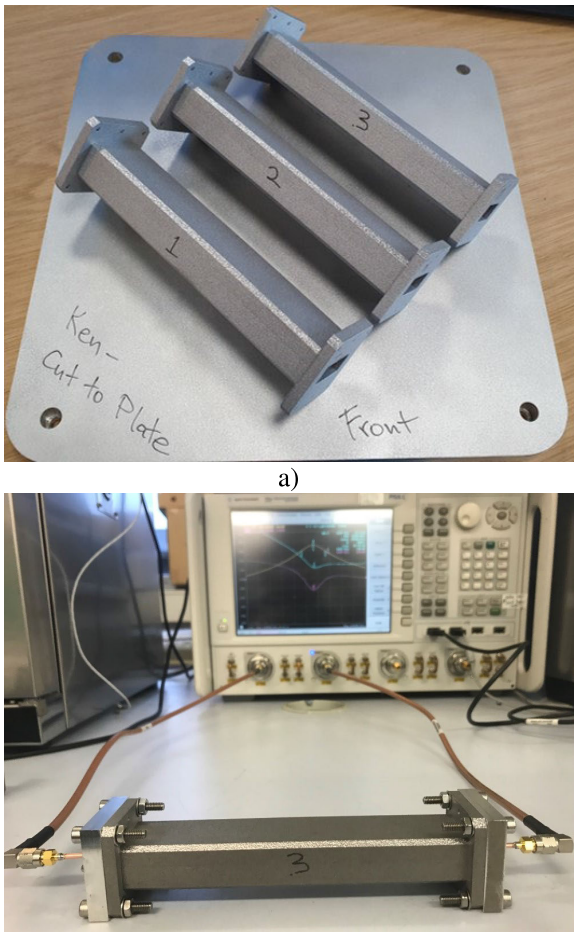

FIGURE 9. Additive manufactured AlSi10Mg waveguide sections, a) post build and b) connected as a cavity resonator to a vector network analyser.

where G is found through simulation using COMSOL Multi-physics software. The measured R_S values for each waveguide section are shown in Fig. 10. There is a clear reduction in R_S for sample ALM3, arising from the use of 180 W for the downskin laser power, when compared to the default value (ALM1: 100 W) and the absence of a downskin layer (ALM2: 0 W). These results are promising for the optimisation of PBF produced parts for microwave applications.

To asses how the reduction in R_S will translate into a waveguide transmission line system, attenuation has been calculated using the measured resonator R_S (R_{Sr}) values over the X-band frequency range. Conductor attenuation (α_c) due to the surface conduction losses of a uniform, rectangular waveguide in the TE_{10} mode is assessed by [21]

$$\alpha_c = \frac{R_{Sr}(f)}{b\eta_0\sqrt{1-x^2}}\left[1+\frac{2bx^2}{a}\right] \tag{7}$$

where a and b are the long and short internal dimensions of the waveguide, respectively, and η_0 is wave impedance of free space. The dimensionless parameter x is defined as the ratio $x = f_c/f$, where $f_c = c/2a$ is the cut-off frequency of the TE_{10} mode and f is the frequency of single mode operation

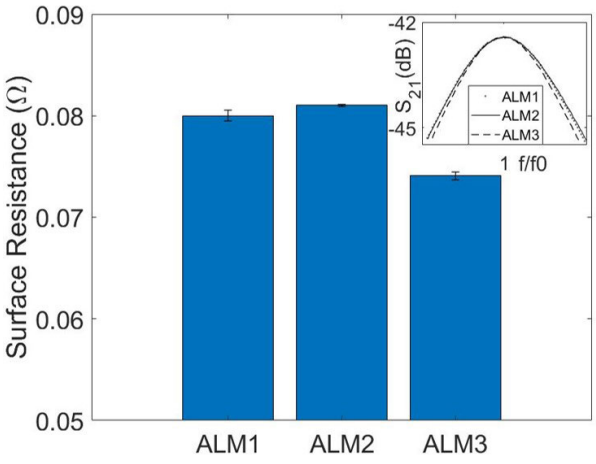

FIGURE 10. Measured surface resistance values for additive manufactured rectangular waveguide resonators produced using various down skin laser powers. Inset is the forward transmission S parameter traces for each waveguide resonator.

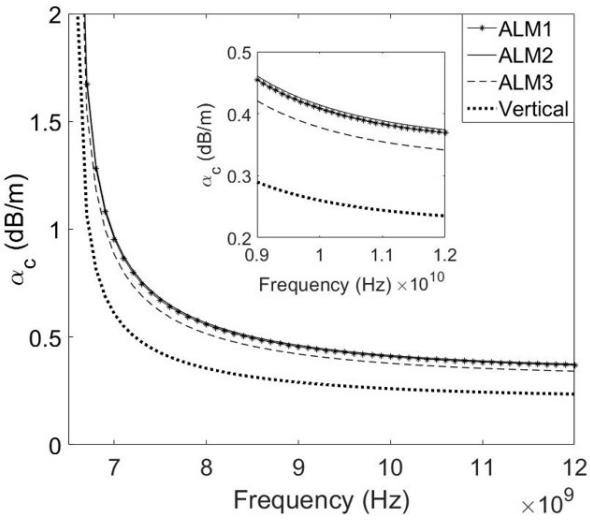

FIGURE 11. Calculated attenuation for TE_{10} mode of three rectangular waveguides produced by additive manufacturing using various downskin laser powers. Also included is a calculated value for an equivalent waveguide consisting of vertical surfaces. Inset is a magnified view of the calculated attenuation.

(i.e. in the range $c/2a < f < c/2b$). For calculation of α_c over the X-band frequency range, R_{Sr} is scaled from the cavity resonator measured value by

$$R_{Sr}(f) = R_{Sr}\sqrt{\frac{f}{for}} \tag{8}$$

Fig. 11 shows the calculated α_c values for each waveguide section over the X-band frequency range. The reduced R_S value for ALM3 provided a modest ∼0.05 dB/m improvement in conductor loss. For completeness, and to show the effect of build orientation on attenuation, a calculated value for an equivalent rectangular waveguide built in a vertical orientation is included on Fig. 11; the R_S value for this is taken from Fig. 6. Attenuation is significantly lower (∼0.13 dB/m) in the absence of downward facing surfaces.

V. CONCLUSION

In this study, additive manufactured sample plates orientated in three common build angles and several X-band waveguide sections have been manufactured from AlSi10Mg and evaluated for microwave loss. Sweeps of laser power on different parameter settings have been performed the following conclusions can been drawn:

1) The traditional macro approach to testing additive manufactured waveguide components has a significant flaw in that it does not take into account the notably higher loss contributions arising from downwards facing surfaces. Knowledge of the microwave surface resistance for each surface orientation should form part of the design-for-additive process.
2) A correlation has been established between increasing laser processing power and reduction of microwave surface resistance as well as average surface roughness for downwards facing surfaces.

Furthermore, this study has shown that it is possible to optimise additive manufactured components to improve microwave performance through the adaptation of build process parameters affecting the surface finish. However, the influence that increased laser power may be having on the mechanical properties of the surfaces has not been investigated here and would be a useful further study in the drive for increased industry uptake.

The results presented here are promising for the continued improvement in performance, and subsequent industrial uptake, of PBF components for microwave applications, where the design of three-dimensional parts will inevitably necessitate for one or more downward facing surfaces.

ACKNOWLEDGMENT

Information on the data underpinning the results presented here, including how to access them, can be found in the Cardiff University data catalogue at http://doi.org/10.17035/d.2021.0129673935.

Thanks is given to Prof. M Gumbleton at the School of Pharmacy, Cardiff University, for support with optical microscopy imaging.

REFERENCES

[1] N. T. Aboulkhair, N. M. Everitt, L. Ashcroft, and C. Tuck, "Reducing porosity in AlSi10Mg parts processed by selective laser melting," *Additive Manuf.*, vols. 1–4, pp. 77–86, Oct. 2014.

[2] H. Williams and E. Butler-Jones, "Additive manufacturing standards for space resource utilization," *Additive Manuf.*, vol. 28, pp. 676–681, Aug. 2019.

[3] S. H. Khajavi, J. Partanen, and J. Holmström, "Additive manufacturing in the spare parts supply chain," *Comput. Ind.*, vol. 65, no. 1, pp. 50–63, Jan. 2014.

[4] P. A. Booth and E. Valles Lluch, "Realising advanced waveguide bandpass filters using additive manufacturing," *IET Microw., Antennas Propag.*, vol. 11, no. 14, pp. 1943–1948, Nov. 2017.

[5] O. A. Peverini, M. Lumia, F. Calignano, G. Addamo, M. Lorusso, E. P. Ambrosio, D. Manfredi, and G. Virone, "Selective laser melting manufacturing of microwave waveguide devices," *Proc. IEEE*, vol. 105, no. 4, pp. 620–631, Apr. 2017.

[6] P. Booth and E. V. Lluch, "Enhancing the performance of waveguide filters using additive manufacturing," *Proc. IEEE*, vol. 105, no. 4, pp. 613–619, Apr. 2017.
[7] C. R. Garcia, R. C. Rumpf, H. H. Tsang, and J. H. Barton, "Effects of extreme surface roughness on 3D printed horn antenna," *Electron. Lett.*, vol. 49, no. 12, pp. 734–736, Jun. 2013.
[8] F. Calignano *et al.*, "High-performance microwave waveguide devices produced by laser powder bed fusion process," *Procedia CIRP*, vol. 79, pp. 85–88, Mar. 2019.
[9] A. Charles, A. Elkaseer, L. Thijs, V. Hagenmeyer, and S. Scholz, "Effect of process parameters on the generated surface roughness of down-facing surfaces in selective laser melting," *Appl. Sci.*, vol. 9, no. 6, p. 1256, Mar. 2019.
[10] B. Zhang and H. Zirath, "A metallic 3-D printed E-band radio front end," *IEEE Microw. Wireless Compon. Lett.*, vol. 26, no. 5, pp. 331–333, May 2016.
[11] M. D'Auria, W. J. Otter, J. Hazell, B. T. W. Gillatt, C. Long-Collins, N. M. Ridler, and S. Lucyszyn, "3-D printed metal-pipe rectangular waveguides," *IEEE Trans. Compon., Packag., Manuf. Technol.*, vol. 5, no. 9, pp. 1339–1349, Sep. 2015.
[12] R. Gumbleton, J. A. Cuenca, G. M. Klemencic, N. Jones, and A. Porch, "Evaluating the coefficient of thermal expansion of additive manufactured AlSi10Mg using microwave techniques," *Additive Manuf.*, vol. 30, Dec. 2019, Art. no. 100841.
[13] E. Hammerstad and O. Jensen, "Accurate models for microstrip computer-aided design," in *IEEE MTT-S Int. Microw. Symp. Dig.*, Washington, DC, USA, May 1980, pp. 407–409.
[14] V. J. Matjeke, C. Moopanar, A. S. Bolokang, and J. W. van der Merwe, "Effect of heat treatment time on the microstructure and mechanical deformation behavior of additive-manufactured AlSi10Mg components," *Prog. Additive Manuf.*, vol. 5, pp. 379–385, Jun. 2020.
[15] H. Chen, D. Gu, J. Xiong, and M. Xia, "Improving additive manufacturing processability of hard-to-process overhanging structure by selective laser melting," *J. Mater. Process. Technol.*, vol. 250, pp. 99–108, Dec. 2017.
[16] R. M. German, *Sintering Theory and Practice*. Hoboken, NJ, USA: Wiley, vol. 1996.
[17] J. C. Fox, S. P. Moylan, and B. M. Lane, "Preliminary study toward surface texture as a process signature in laser powder bed fusion additive manufacturing," in *Proc. Summer Top. Meeting: Dimensional Accuracy Surf. Finish Additive Manuf.*, 2016, pp. 168–173.
[18] R. Gumbleton, J. A. Cuenca, S. Hefford, K. Nai, and A. Porch, "Measurement technique for microwave surface resistance of additive manufactured metals," *IEEE Trans. Microw. Theory Techn.*, vol. 69, no. 1, pp. 189–197, Jan. 2021.
[19] D. Pozar, *Microwave Engineering*. Hoboken, NJ, USA: Wiley, 1998.
[20] R. Gumbleton, K. Nai, S. Hefford, and A. Porch, "Effects of post-processing treatments on the microwave performance of additively manufactured samples," in *Proc. 13th Eur. Conf. Antennas Propag. (EuCAP)*, Krakow, Poland, Mar./Apr. 2019, pp. 1–4.
[21] S. Ramo, J. R. Whinnery, and T. van Duzer, *Fields and Waves in Communication Electronics*, 3rd ed. Hoboken, NJ, USA: Wiley, 1994.

RICHARD GUMBLETON received the B.Eng. (Hons.) degree in electronic and communications engineering from Cardiff University, U.K., in 2017, where he is currently pursuing the Ph.D. degree in microwave engineering as part of an ICASE studentship award with Renishaw PLC.

His research interest includes additive manufacturing for microwave applications, specifically the characterisation and optimisation of additive manufactured surfaces.

ROBERT BATSON received the B.Eng. (Hons.) degree in electrical and electronic engineering from Cardiff University, U.K., in 2018, where he is currently pursuing the Ph.D. degree in microwave engineering as part of an ICASE studentship award with Renishaw PLC.

His current research interest includes measurement techniques that utilises microwave and millimeter wave structures to characterise and optimise additive manufacturing surfaces.

KENNETH NAI received the B.Sc. (Hons.) degree in electronics and electrical engineering and the Ph.D. degree in control systems from Loughborough University, U.K., in 1990 and 1995, respectively.

Since 1995, he has been with Renishaw PLC, Wotton-Under-Edge, U.K., where he is currently a Principal Engineer and he has developed products in the field of metrology systems, neuro-surgical robotics, and metal powder 3-D printers. He has been granted 12 U.S. patents. He is also a member of the Institution of Engineering and Technology and a Chartered Engineer.

ADRIAN PORCH received the M.A. degree in physics and the Ph.D. degree in low temperature physics from Cambridge University, Cambridge, U.K., in 1986 and 1990, respectively.

He is currently a Professor with the School of Engineering, Cardiff University, Cardiff, U.K., where he leads the Center for High Frequency Engineering. He has 34 years of experience in applying microwave methods to measure and understand the fundamental properties of electronic materials, with 165 relevant publications. More recently, he has developed microwave sensors and applicators across different disciplines, including new medical sensors and new methods in electron paramagnetic resonance spectroscopy.